UNIVERSIDADE TECNOLÓGICA FEDERAL DO PARANÁ

YAMID ENRIQUE NUÑEZ DE LA ROSA

# COMPORTAMENTO FRENTE A CORROSÃO DO AÇO INOXIDÁVEL DUPLEX UNS S32205 NITRETADO E SOLDADO

CURITIBA
2023

YAMID ENRIQUE NUÑEZ DE LA ROSA

# COMPORTAMENTO FRENTE A CORROSÃO DO AÇO INOXIDAVÉL DUPLEX UNS S32205 NITRETADO E SOLDADO

## Corrosion behavior of duplex stainless steel UNS S32205 nitrided and welded

Trabalho de conclusão de curso de pós-graduação apresentada como requisito para obtenção do título de Doutor em Engenharia no Programa de Pós-graduação em Engenharia Mecânica (PPGEM) da Universidade Tecnológica Federal do Paraná (UTFPR). Área de concentração: Engenharia de Materiais.

Orientador: Prof. Dr. Paulo César Borges.

CURITIBA

2023

**Ministério da Educação**
**Universidade Tecnológica Federal do Paraná**
**Campus Curitiba**

YAMID ENRIQUE NUNEZ DE LA ROSA

## COMPORTAMENTO FRENTE A CORROSÃO DO AÇO INOXIDAVÉL DUPLEX UNS S32205 NITRETADO E SOLDADO

Trabalho de pesquisa de doutorado apresentado como requisito para obtenção do título de Doutor Em Engenharia da Universidade Tecnológica Federal do Paraná (UTFPR). Área de concentração: Engenharia De Materiais.

Data de aprovação: 27 de Julho de 2023

Dr. Paulo Cesar Borges, Doutorado - Universidade Tecnológica Federal do Paraná

Dr. Carlos Marcus Gomes Da Silva Cruz, Doutorado - Universidade Tecnológica Federal do Paraná

Dra. Elisiane Maria Berton, Doutorado - Centro Universitário de Tecnologia de Curitiba - Unifatec

Dr. Euclides Alexandre Bernardelli, Doutorado - Universidade Tecnológica Federal do Paraná

Dr. Gelson Biscaia De Souza, Doutorado - Universidade Estadual de Ponta Grossa (Uepg)

Documento gerado pelo Sistema Acadêmico da UTFPR a partir dos dados da Ata de Defesa em 17/08/2023.

Dedico este trabalho a Oriana Palma Calabokis

# AGRADECIMENTOS

A Deus pela oportunidade de me trazer aqui neste ponto da vida, pelos logros obtidos, pela oportunidade de conhecer tantas pessoas maravilhosas que me acompanharam na minha caminhada de vida e que ainda estão aí sem importar a distância.

Agradeço especialmente a minha esposa Oriana Palma Calabokis por ter me acompanhado nesta etapa, por ser a minha parceira de loucuras, de pesquisa e por ter me apoiado sempre sem duvidar e pelo seu amor.

Aos meus pais Boris e Maria, meus irmãos Melissa, Jonatan, Katerine, Yeison e Jairo aos meus sogros Marcos y Maritza, por ter sido meu apoio permanente durante todo este tempo.

Ao professor Paulo César Borges por acreditar em mim e por ser mais que um excelente orientador, um amigo incondicional.

Aos professores que fizeram parte do meu crescimento profissional Paulo Borges, Carlos H. da Silva, Marcio Mafra, Giuseppe Pintaúde, Euclides Bernardelli, Julio das Neves, Carlos Cruz, Carlos Lepienski, Gloria Pena Uris e Carmen Maria Abreu.

Agradeço aos meus amigos Yamid García, Luis Quitian, Jhonattan Trejo, Carmen Fuenmayor, Walter Abujder, Kelly Gonzalez, Alejandro Guerrero, Jair Arrieta, Carlos Millan, Fatima Cividini, Marco Piccione, Francisco Piccione, Alexandre José, Jomar Riveiro, Pedro Quadros, Alba Turin e Ángel Rivera por todos os momentos de companhia e apoio.

À Universidade Tecnológica Federal do Paraná (UTFPR), ao Programa de Pós-Graduação em Engenharia Mecânica e de Materiais (PPGEM) e ao grupo de pesquisa GrMatS por toda estrutura proporcionada para o desenvolvimento desta tese e também a Universidade de Vigo.

A CAPES pela bolsa de estudo (88887.484833/2020-00) e pelo período Sanduiche na Espanha PDSE (88881.624474/2021-01).

Por fim, a todos aqueles que de alguma forma, direta ou indiretamente, me apoiaram neste projeto.

Nunca ande por trilhas, pois assim
só irá até onde outros já foram.
*Alexander Graham Bell*

# RESUMO

No presente trabalho é apresentado um estudo do comportamento frente a corrosão do aço inoxidável duplex UNS S32205 tratado pelo tratamento termoquímico de nitretação a plasma em baixa temperatura (380 °C) e soldado pelo processo TIG segundo parâmetros empregados na indústria. Os tópicos principais abordados neste estudo são: Corrosão localizada (pites e fresta), desgaste e tribocorrosão. Resultados destes estudos foram apresentados em três publicações em periódicos científicos: "*The effect of plasma nitriding on the synergism between wear and corrosion of SAF2205 duplex stainless steel*", "*Effect of low-temperature plasma nitriding on corrosion and surface properties of duplex stainless steel UNS S32205*" e "*Pitting and crevice corrosion behavior of the duplex stainless steel UNS S32205 welded by using the GTAW process*". Os principais resultados e conclusões deste trabalho são: A nitretação a plasma a baixa temperatura (380 °C) no aço inoxidável duplex UNS S32205 promoveu a formação de uma camada contínua de austenita expandida com espessura de aproximadamente de 3,5 μm com uma dureza de até três vezes a dureza do substrato. Os ensaios de polarização cíclica revelaram uma melhora na resistência à corrosão localizada do aço nitretado, apresentando maiores valores de potenciais de pites e de repassivação e menor laço de histerese em comparação com a condição não tratada. A presença de uma camada de austenita expandida causou uma redução no desgaste puro e na taxa de desgaste por efeito da tribocorrosão. O processo de solda TIG empregado no aço inoxidável duplex UNS S32205 manteve o comportamento eletroquímico do material próximo ao comportamento do metal base. Isso é consequência de vários aspectos, como o equilíbrio 50/50 das fases austenita-ferrita, ao longo do metal de solda e a não formação de precipitados de fases deletérias ($\sigma$, $\chi$) e a distribuição adequada dos elementos de liga entre o metal base e o metal de solda. Apesar das mudanças microestruturais e de composição química que produzem ambos os processos avaliados (nitretação e solda), os mesmos não prejudicaram a principal característica do AID que é a resistência a corrosão em meios contendo cloretos.

**Palavras-chave**: UNS S32205; corrosão por frestas; corrosão por pites; nitretação; solda TIG.

# ABSTRACT

This work presents a study on the corrosion behavior of duplex stainless steel UNS S32205 treated with low-temperature thermochemical whit plasma nitriding and welded using the TIG process according to industry-standard parameters. The main topics addressed in this study are localized corrosion (pitting and crevice), wear, and tribocorrosion. The results of these studies were presented in three publications in scientific journals: "*The effect of plasma nitriding on the synergism between wear and corrosion of SAF2205 duplex stainless steel*", "*Effect of low-temperature plasma nitriding on corrosion and surface properties of duplex stainless steel UNS S32205*" and "*Pitting and crevice corrosion behavior of the duplex stainless steel UNS S32205 welded using the GTAW process*". The main conclusions of this study are as follows: Low-temperature plasma nitriding (380 °C) in duplex stainless steel UNS S32205 promoted the formation of a continuous layer of expanded austenite with an approximate thickness of 3,5 µm and a hardness of which is three times the hardness of the substrate. Cyclic polarization tests revealed an improvement in the resistance to localized corrosion of the nitrided steel, with higher pit potentials, repassivation potentials, and a smaller hysteresis loop compared to the untreated condition. The presence of an expanded austenite layer resulted in a reduction in pure wear and wear rate due to the effect of tribocorrosion. The TIG welding process employed in duplex stainless steel UNS S32205 maintained the electrochemical behavior of the material close to that of the base metal. This is due to several factors, such as the balanced 50/50 ratio of austenite-ferrite phases throughout the weld metal, the absence of detrimental precipitates ($\sigma$, $\chi$), and the proper distribution of alloying elements between the base metal and the weld metal. Despite the microstructural and chemical composition changes resulting from both evaluated processes (nitriding and welding), they did not compromise the main characteristic of duplex stainless steel, which is its resistance to corrosion in chloride-containing environments.

**Keywords**: UNS S32205; pitting corrosion; crevice corrosion; nitriding; GTAW weld.

# LISTA DE ILUSTRAÇÕES

# LISTA DE ABREVIATURAS

| | |
|---|---|
| AID | Aço inoxidável duplex |
| AI/IA | Austenita intergranular/ Intergranular austenite |
| ASTM | American Society for Testing and Materials |
| AW | Austenita Widmanstätten/ Widmanstätten autenite |
| DRX/XRD | Difração de raios-X/ X-ray diffraction |
| EDS | Energy-dispersive X-ray spectroscopy |
| FCAW | Flux cored arc welding |
| FCC | Fase centrada no corpo |
| GTAW/TIG | Gas Tungsten Arc Welding/ Tungsten Inert Gas |
| MB/BM | Metal base/Base metal |
| MEV/SEM | Microscopia eletrônica de varredura |
| MO/OM | Microscopia ótica |
| PCA/OCP | Potencial de circuito aberto/ Open circuit potential |
| PD | Polarização potenciodinâmica/Potentiodynamic polarization |
| PMI | Positive material identification |
| PREN | Pitting resistance equivalent number |
| PS | Polarização estática/Static polarization |
| SAF | Sandvik Austenite Ferrite |
| SHE | Standard Hydrogen Electrode |
| TCP | Temperatura crítica de pites |
| UNS | Unified numbering system |
| WDS | Wavelength-dispersive X-ray spectroscopy |
| ZF/WM | Zona fundida/ Weld metal |
| ZTA/HAZ | Zona térmicamente afetada/ Hot affected zone |

# LISTA DE SÍMBOLOS E UNIDADES

| | | |
|---|---|---|
| **Ag** | Prata | |
| **AgCl** | Cloreto de prata | |
| **Ar** | Argônio | |
| **C** | Carbono | |
| $\mathbf{C_0}$ | Taxa de corrosão | |
| **Cr** | Cromo | |
| **CuK- α** | Radiação cobre K- α | [u.a] |
| $\mathbf{d_{50}}$ | Tamanho meio de partícula | [μm] |
| $\mathbf{E_{bd}:E_p}$ | Potencial de quebra de camada/potencial de pites | [V] |
| $\mathbf{E_{corr}}$ | Potencial e corrosão | [V] |
| $\mathbf{E_{pass}}$ | Potencial de passivação | [V] |
| **Fe** | Ferro | |
| **g** | Grama | [g] |
| $\mathbf{H_2}$ | Hidrogênio | |
| $\mathbf{H_2O}$ | Água | |
| $\mathbf{H_2SO_4}$ | Ácido sulfúrico | |
| **HCl** | Ácido clorídrico | |
| **hkl** | Índices de Miller | |
| $\mathbf{i_{corr}}$ | Densidade de corrente de corrosão | [μA/cm$^2$] |
| $\mathbf{I_{corr}}$ | Corrente de corrosão | [μA] |
| **KCl** | Cloreto de potássio | |
| **M** | Mol | [Mol] |
| **Mn** | Manganês | |
| **Mo** | Molibdênio | |
| **N** | Newton | [N] |
| $\mathbf{N_2}$ | Nitrogênio | |
| **NaCl** | Cloreto de sódio | |
| **Ni** | Níquel | |
| **Ø** | Diâmetro | [m] |
| **P** | Fosforo | |
| **Pa** | Pascais | [Pa] |
| **S** | Desgaste por efeito sinérgico | [mm/ano] |
| **S** | Enxofre | |
| **Si** | Silício | |
| $\mathbf{SiO_2}$ | Dióxido de silício | |
| $\mathbf{S_p}$ | Altura máxima do pico | |
| $\mathbf{S_q}$ | Parâmetro de rugosidade | |
| $\mathbf{S_{sk}}$ | Parâmetro de assimetria | |
| $\mathbf{S_{tr}}$ | Raio de aspecto | |
| $\mathbf{T_0}$ | Desgaste tribocorrosivo | [mm/ano] |
| **V** | Volts | [V] |
| $\mathbf{W_0}$ | Desgaste puro | [mm/ano] |
| **α** | Ferrita | |
| **γ** | Austenita | |
| $\gamma_N$ | Austenita expandida | |
| $\gamma_N^{\alpha}$ | Austenita expandida proveniente da ferrita | |
| $\gamma_N^{\alpha\gamma}$ | Austenita expandida proveniente da austenita | |
| **θ** | Teta | [°] |
| **λ** | Comprimento de onda | [m] |
| **ρ** | Densidade | [g/cm$^3$] |

# SUMÁRIO

# 1 INTRODUÇÃO

Os aços inoxidáveis duplex (AID´s) são uma família de aços que apresentam uma microestrutura composta por duas fases: austenita (γ) e ferrita (α), em proporções aproximadamente iguais (Freitas et al., 2021; Liang et al., 2020; Pezzato & Calliari, 2022). O interesse nessa família de aços provém principalmente da boa resistência aos diversos tipos de corrosão (corrosão sob tensão, localizada (pites e fresta) e generalizada (Geng et al., 2015; Gholami et al., 2015), isto deve-se em grande parte à presença de cromo na sua composição, responsável pela formação de uma fina camada estável e protetora na superfície que conferem estas propriedades (Alphonsa et al., 2015; Gholami et al., 2015). Em adição, a microestrutura bifásica nos AID´s também confere boas propriedades mecânicas (dependendo das percentagens dos principais elementos de liga (Mo, N e Ni) (Geng et al., 2015)) que fazem com que a implementação destes tenha ganhado força considerável em aplicações industriais tais como a indústria de exploração e produção marítima, transporte e extração de petróleo, indústria aeronáutica, papel e celulose, farmacêutica, petroquímica e aplicações químicas (Dan et al., 2022; Davidson & Singamneni, 2022; Freitas et al., 2021; Geng et al., 2015; Liang et al., 2020; Pintaude et al., 2019).

Nas indústrias de transporte/extração de petróleo e papel e celulose, os AID substituem aos aços inoxidáveis austeníticos e aços carbono devido à redução dos custos associados às falhas e substituição dos componentes que representa custos elevados e pausas na produção. Isto traz uma diminuição dos custos associados à manutenção dos componentes, além de evitar prejuízos no meio (Patrick De Leão et al., 2014). Ainda quando estes aços possuem um bom desempenho em meios agressivos, nem sempre atendem os requerimentos esperados pelas indústrias (alto desempenho: (Alphonsa et al., 2015)), motivo pelo qual pesquisadores procuram alternativas para melhorar as propriedades destes aços através de tratamentos de modificação de superfícies.

Dentre os tratamentos de modificação de superfície destacam-se os tratamentos de nitrocarburização, cementação e nitretação a plasma (Ahamad & Jauhari, 2012; Alphonsa et al., 2015; Dan et al., 2022; Haruman et al., 2020; Palma et al., 2021; Subbiah et al., 2019; Yan et al., 2014). Este último, nitretação a plasma é um tratamento termoquímico que visa a introdução de nitrogênio por difusão na superfície do aço, através de um meio gasoso parcialmente ionizado, com temperaturas na faixa entre 300 a 570 °C (Alves, 2001) e também é considerado uma tecnologia limpa que atende as normas ambientais (Pedrali, 2012). Quando a nitretação a plasma é conduzida em baixas temperatura (<450 °C) em AID, esta promove a formação de uma camada constituída por uma fase de austenita expandida (γN) ou também conhecida como fase S como relatado nos trabalhos de (Alphonsa et al., 2015; Dan et al., 2022; Haruman et al., 2020; Palma et al., 2021; Pintaude et al., 2019). A formação desta fase expandida nos AID´s, confere mas também só uma dureza superficial e resistência ao desgaste significativamente superior ao estado de fornecimento, mas também uma melhora na resistência à corrosão (Alphonsa et al., 2015; Dan et al., 2022; Palma et al., 2021).

Por outro lado, na industría a conformação de peças como tubos, válvulas ou tanques, comumente são necessários processos de uniões de peças (soldagem). No entanto, esses processos envolvem exposição a ciclos térmicos que podem alterar o equilíbrio das fases α/γ, as porcentagens de elementos de liga e levar ao aparecimento de fases deletérias tais como as fases $\chi$, $\sigma$, laves (Yousefieh et al., 2011). Como consequência, as propriedades mecânicas podem diminuir e a suscetibilidade à corrosão localizada pode aumentar (Geng et al., 2015).

Os processos de solda comumente empregados nos AID´s segundo a literatura são: GMAW (Gas Metal Arc Welding) (Azzi & Klemberg-Sapieha, 2011; Borges et al., 2019; Luchtenberg et al., 2019), FCAW (Flux-Cored Arc Welding) (Gnanasundaram & Natarajan, 2014; Zappa et al., 2017), SAW (Submerged Arc Welding) (Luo et al., 2013), SMAW (Shield Metal Arc Welding) ((Aguilar- Sierra et al., 2015; Elsaady et al., 2018)) e GTAW (Gas Tungsten Arc Welding (Geng et al., 2015; Heider et al., 2020; Tahaei et al., 2016; Zappa et al., 2017). Sendo o processo GTAW (TIG) um dos processos que fornece melhor balanço das fases ferrita e austenita segundo é sugerido pelas normas (NORSOK Standard, 2016; TAPPI, 2001) quando comparado com outros processos de soldagem (Leite et al., 2019; Moraes e Videira, 2016; Yousefieh et al., 2011).

Nesse contexto, e tendo em conta as alterações que geram os processos de nitretação e solda no AID, neste trabalho foi estudado a resistência à corrosão, desgaste abrasivo, e tribocorrosão do AID UNS S32205 no estado de fornecimento, nitretado e soldado pelo processo TIG. Os estudos são apresentados em três artigos publicados em periódicos especializados, onde se abordaram as seguintes situações específicas.

i. Efeito do tratamento termoquímico de modificação da superfície nitretada por plasma em baixas temperaturas do AID UNS S32205 e a sua resistência a corrosão.
ii. Efeito da nitretação em baixas temperaturas no AID UNS S32205 e a sua resistência à corrosão, desgaste e tribocorrosão.
iii. Comportamento da corrosão localizada (pites e frestas) do AID UNS S32205 soldado pelo processo TIG de acordo com os parâmetros da indústria.

# 2 OBJETIVOS

## 2.1 Objetivo geral

Estudar o comportamento frente a corrosão e tribocorrosão do aço inoxidável duplex UNS S32205 no estado de fornecimento, nitretado por plasma em baixa temperatura (380 °C), bem como o efeito do ciclo térmico gerado durante a solda pelo processo TIG na corrosão localizada.

## 2.2 Objetivos específicos

Avaliar o efeito da nitretação em baixa temperatura do aço inoxidável duplex UNS S32205 e o seu desempenho frente à corrosão.

Avaliar a resistência ao desgaste, corrosão e sinergia do aço duplex UNS S32205 com e sem nitretação por plasma a baixa temperatura.

Avaliar o efeito do ciclo térmico de solda pelo processo TIG na resistência a corrosão localizada e microestrutura do aço duplex UNS S32205.

# 3 ESTRUTURA DO TRABALHO

Para cumprir com os objetivos estabelecidos utiliza-se a forma de coletânea de artigos para a apresentação da tese de doutorado a qual está constituída por três artigos. Assim, esta tese se divide em dez capítulos. No primeiro capítulo é realizada uma introdução onde é feito a abordagem do tema principal de estudo e uma contextualização do problema, no capítulo dois, são apresentados os objetivos tracejados. No terceiro capítulo, se apresenta a estrutura do trabalho. A revisão bibliográfica é apresentada no capítulo quatro. Os capítulos cinco, seis e sete, reproduzem os três artigos publicados em periódicos especializados. E o capítulo oitavo traze as conclusões gerais sobre o tema explorado. Por fim, sugestões para trabalhos futuros e referências utilizadas no trabalho.

No final do documento contém um apêndice onde são apresentados uma lista de artigos publicados, capítulo de livro, participações em congresso e outras atividades desenvolvidas durante o período de doutorado. Todas elas desenvolvidas durante o período do doutorado.

## 3.1 Effect of low-temperature plasma nitriding on corrosion and surface properties of duplex stainless steel UNS S32205

Publicado no ano 2020 no *Journal of Materials Engineering and Performance.* Este artigo trata sobre o efeito da nitretação por plasma em baixa temperatura (380 °C) nas propriedades mecânicas (dureza), topográficas e de corrosão do aço inoxidável duplex (AID) UNS S32205.

Se trata de um estudo comparativo baseado em medidas de microdureza, medições de rugosidade superficial e ensaios de polarização cíclica e potenciostática em solução de NaCl, em amostras de AID UNS S32205 nitretadas por plasma e não tratadas.

Na literatura tem estudos de corrosão em aços duplex nitretados, nos quais, foi reportado a formação de uma "lombada" na região de passivação antes do potencial de pite. Essa "lombada" consiste em um aumento contínuo até um máximo na densidade de corrente, seguido por uma diminuição até atingir novamente a densidade de passivação. Os trabalhos que evidenciaram tal característica, carecem de explicação e sustento científico do que poderia estar acontecendo nesse local. Este trabalho abordou essa temática visando preencher essa lacuna da literatura. O método proposto foi avaliar através de ensaios potenciostáticos a resposta da densidade de corrente ao longo dessa região.

Micrografias obtidas através de microscopia ótica (MO) e microscopia eletrônica de varredura (MEV), permitiram evidenciar que logo da nitretação foi gerada uma camada com uma microestrutura bem definida de austenita expandida pelo nitrogênio (verificado também com DRX). Essa camada, apresentou uma dureza superior ao substrato do AID UNS S32205 não nitretado.

Medições de rugosidade mediante interferometria 3D mostraram que o tratamento de nitretação gerou uma topografia mais isotrópica com predominância de picos.

Após ensaios eletroquímicos, os parâmetros obtidos de corrosão mostraram um aumento da resistência à corrosão que pode ser atribuído à formação de uma camada de austenita expandida na superfície das amostras nitretadas por plasma. Esta camada pode reduzir a taxa de corrosão do AID UNS S32205, impedindo a penetração de íons cloreto na superfície da amostra.

A maior rugosidade da superfície nitretada, não prejudicou o desempenho frente a corrosão localizada.

Os resultados dos ensaios potenciostáticos evidenciaram que a formação da "lombada" na região de passivação é devida a nucleação de pites metaestáveis. Os pites metaestáveis são pites de tamanho microscópico que nucleiam e são repassivados antes de iniciar a etapa de propagação para pites estáveis. Por outro lado, também foi verificado neste artigo, que a corrosão no aço duplex nitretado ocorreu preferencialmente na fase austenita expandida ($\gamma_N^\alpha$) proveniente da fase ferrita e nas regiões intergranulares.

Em resumo, este estudo demonstrou que a nitretação por plasma em baixa temperatura é uma técnica eficaz para melhorar a resistência à corrosão e a dureza superficial do AID UNS S32205, tornando-o mais resistente à corrosão em ambientes agressivos.

## 3.2 The effect of plasma nitriding on the synergism between wear and corrosion of SAF 2205 duplex stainless steel

Este segundo artigo foi publicado no ano 2020 no *Industrial Lubrication and Tribology*. Neste trabalho foi investigado o efeito da nitretação por plasma em baixas temperaturas (380 °C) no desgaste mecânico, corrosivo e o efeito da sinergia entre desgaste e corrosão do aço inoxidável duplex (AID) UNS S32205 (SAF 2205).

Diversos estudos em aços inoxidáveis sobre o desgaste e corrosão tem evidenciado que os efeitos combinados geralmente resultam em perdas de materiais superiores do que a soma de ambos os processos isoladamente, o que indica que existe um efeito sinérgico de degradação entre eles. Neste trabalho foi abordado como a nitretação no aço duplex influi no desgaste puro, corrosão e no efeito sinérgico abrasão-corrosão. Para isso, o trabalho foi realizado em quatro estágios. Um primeiro estágio consistiu na nitretação e caracterização do AID UNS S32205. No segundo estágio, foram realizados ensaios de desgaste puro no tribômetro na configuração esfera sobre plano, empregando como abrasivo uma lama de água destilada com 20 % $Al_2O_3$ em ambiente inerte com 99 % de nitrogênio dentro de uma caixa de luvas pressurizada. No terceiro estágio, ensaios de corrosão pura foram realizados, fazendo uso de uma célula de corrosão em solução de NaCl ao 3,5 %. E finalmente o quarto estágio, foi avaliado o efeito sinérgico na configuração esfera sobre plano com lama constituída por solução de NaCl 3,5 % e suspensão ao 20 % de $Al_2O_3$.

Caracterizações do aço nitretado evidenciaram uma camada superficial com espessura de 3 µm e dureza em torno de três vezes a dureza do aço no estado de fornecimento. A difração de raios-X (DRX) mostraram um deslocamento do pico da austenita para esquerda, atribuído a formação da fase austenita expandida. Os parâmetros dos ensaios de corrosão indicaram que houve uma melhora na resistência à corrosão devido a nitretação em baixas temperaturas.

Os testes de desgaste puro mostraram que a nitretação por plasma melhorou a resistência ao desgaste do AID UNS S32205. As amostras nitretadas por plasma apresentaram menor taxa de desgaste e menor profundidade de desgaste do que as amostras não tratadas. Nos ensaios mistos (tribocorrosão), a camada nitretada aumentou a resistência à corrosão e desgaste do AID UNS S32205, impedindo a penetração de partículas, abrasivas e reduzindo a taxa de desgaste.

Salienta-se que durante os ensaios de desgaste puro, foi evidenciado o micromecanismo misto prevalecendo o riscamento com presença de algumas indentações das partículas abrasivas, para o material nitretado e no estado de fornecimento. Nos ensaios tribocorrosivos, houve uma mudança de micromecanismo em ambos os materiais, passando a ser por rolamento puro. Assim, evidenciou-se que o efeito sinérgico (tribocorrosão) promoveu maiores taxas de desgaste comparado com o desgaste puro em ambos os materiais, sendo mais resistente o aço nitretado.

Em resumo, este estudo demonstrou que a nitretação por plasma melhorou significativamente a resistência à corrosão do AID UNS S32205 em solução salina, reduzindo a sinergia entre desgaste e corrosão.

### 3.3 Pitting and crevice corrosion behavior of the duplex stainless steel UNS S32205 welded by using the GTAW process

Este terceiro artigo foi publicado no ano 2022 na *Materials Research*. Trata do comportamento frente à corrosão localizada por pites e frestas do aço inoxidável duplex (AID) UNS S32205 soldado pelo processo TIG.

É conhecido que dependendo dos parâmetros dos processos de solda, mudanças macroestruturais são geradas nos aços inoxidáveis duplex. A principal mudança acontece no duplo balanço percentual de ferrita-austenita desde a zona fundida (ZF) até a zona termicamente afetada (ZTA) devido aos gradientes térmicos, os quais são função da velocidade de avanço, corrente e a tensão.

Neste trabalho avaliou-se o efeito dos parâmetros de solda TIG empregados na indústria na resistência a corrosão localizada. Para isso, o estudo foi desenvolvido em três etapas. A primeira etapa consistiu na realização da solda TIG no AID UNS S32205. Na segunda etapa, foram realizadas caracterizações da microestrutura através de espectroscopia de emissão ótica, microscopia eletrônica de varredura, difração de raios-X e medições de microdureza ao longo do cordão de solda (MB – ZF – MB). Finalmente, na terceira etapa, foram realizados ensaios polarização cíclica para análise de corrosão localizada por pites e polarização potenciostática para análise de corrosão localizada por fresta, ambos em solução de 3,5 % NaCl.

Os resultados mostraram que tanto a composição química, difração de raios-X, ensaios de dureza e cálculo de balanço das fases no material soldado atendem aos requisitos das normas TAPPI TIP 0402-29 e Norsok M-601. Portanto, pode-se esperar uma boa resistência à corrosão da união soldada. Resultado que foi corroborado em ambos os tipos de ensaios de corrosão que demonstraram que não foram encontradas diferenças significativas entre o metal base e as amostras soldadas.

Em resumo, este estudo demonstrou que os parâmetros empregados de soldagem pelo processo TIG foram adequados para a produção de juntas de AID UNS S32205 com boa resistência à corrosão por pites e frestas.

# 4 REVISÃO BIBLIOGRAFICA

## 4.1 Aços inoxidáveis dúplex (AID)

Os aços inoxidáveis duplex (AID) recebem esse nome pela sua microestrutura bifásica em frações aproximadamente iguais de austenita (γ) e ferrita (α) em temperatura ambiente (Rodríguez et al., 2017; Rodriguez et al., 2020; Selvabharathi & Muralikannan, 2018; Tahaei et al., 2016; Zappa et al., 2017) como pode-se observar na Figura 1.

**Figura 1 - Microestrutura bifásica do AID UNS S32750 atacado com ácido oxálico 10 % por 30 s: Austenita corresponde as regiões claras e a ferrita corresponde a regiões mais escuras.**

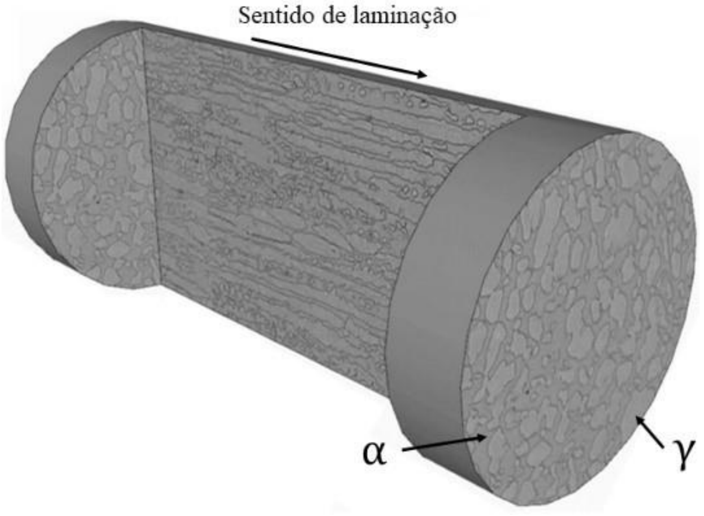

**Fonte: Calabokis, 2019.**

Esse balanço nas fases austenita e ferrita do AID confere uma combinação interessante nas propriedades de resistência mecânica, tenacidade e resistência à corrosão (Mohammed et al., 2017; Paulraj & Garg, 2015; Verma & Taiwade, 2017).

O AID UNS S32205 (3 %Mo, 22 %Cr e 5 %Ni) é principalmente empregado na indústria química, de transporte de petróleo, alimentos, papel e celulose (Azzi & Klemberg-Sapieha, 2011; Sim et al., 2019; Singh & Singh, 2002; Zappa et al., 2018).

## 4.2 Nitretação

### 4.2.1 Nitretação a plasma

O termo genérico nitretação refere-se a um tratamento termoquímico no qual a zona superficial de materiais ferrosos é enriquecida com nitrogênio. Este tratamento é preferencialmente realizado na faixa de temperatura entre 300 e 600 °C. Os conhecidos processos de nitretação fornecem não apenas uma boa proteção contra corrosão (generalizada ou localizada), mas também boa proteção contra desgaste, além de permitir que as características dinâmicas de componentes feitos de materiais ferrosos sejam aprimoradas

(Brinke, 2006). Quando a nitretação por plasma é realizada em aços inoxidáveis é necessário que a temperatura de tratamento seja suficientemente elevada para permitir a difusão intersticial do nitrogênio, e suficientemente baixa para evitar uma difusão de átomos de cromo e a precipitação de nitretos de cromo que prejudiquem a resistência à corrosão do aço (Cardoso et al., 2016).

### 4.2.2 Nitretação a plasma em baixas temperaturas (NPBT)

Pinedo et al., (2013), realizaram NPBT no aço inoxidável AISI F15 (duplex 2205) (400 °C) durante um tempo de 20 h em um reator com fonte DC pulsada de parede quente, em uma atmosfera de 75 % $N_2$ e 25 % $H_2$.

Pinedo e colaboradores baseados nos resultados obtidos por difração de raios-X (Figura 2) e análise por MEV-EBSD para as condições impostas de nitretação, encontraram que o tratamento promoveu a formação de uma fina camada modulada composta por austenita e ferrita expandida (γN, αN).

**Figura 2 - Padrão de difração da amostra nitretada a plasma de baixa temperatura (400 °C), indicando a formação de austenita expandida e ferrita expandida.**

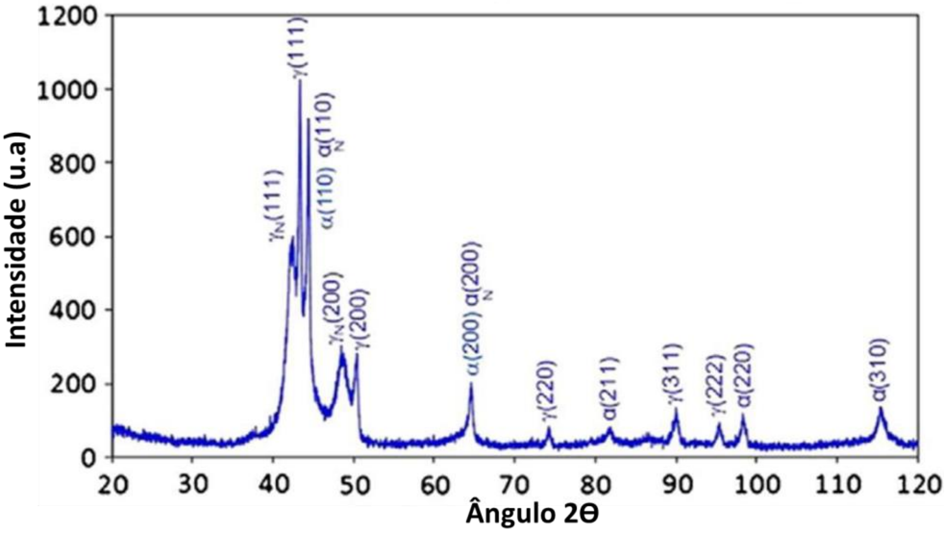

**Fonte: Pinedo et al., 2013.**

Esta camada apresentou uma espessura que variou em função da fase precursora, sendo os valores destes de 2 e 3 μm para austenita e ferrita, respetivamente. Por outra parte, os resultados de microdureza (Figura 3), evidenciaram que a NPBT conferiu ganhos em dureza que foi em torno de quatro vezes a dureza do substrato, devido à supersaturação de nitrogênio acumulada em ambas as fases.

**Figura 3 - Perfis de microdureza da superfície em direção ao núcleo ao longo de (A) um grão de ferrita e (B) um grão de austenita.**

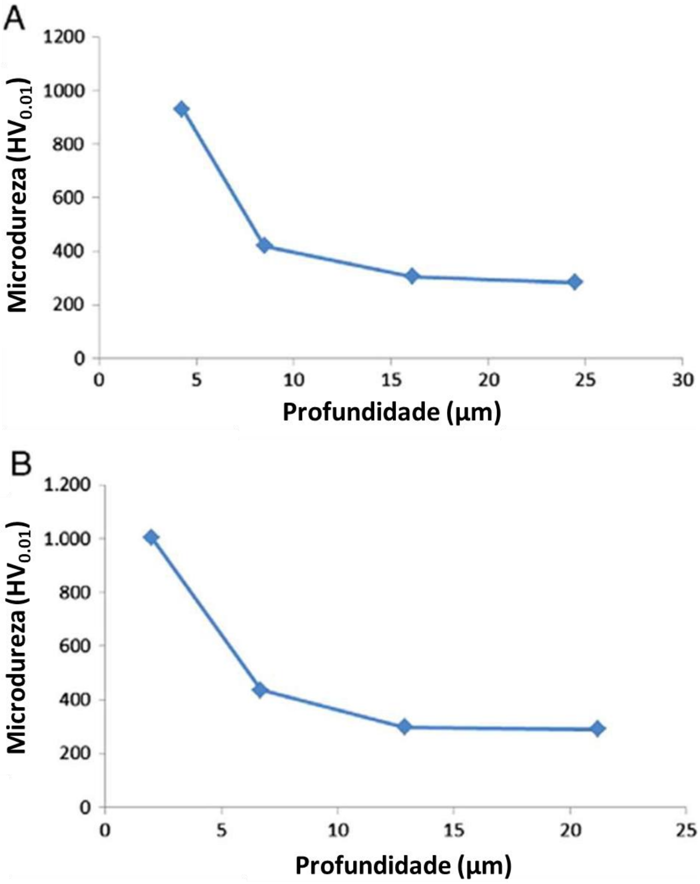

**Fonte: Pinedo et al., 2013.**

Posteriormente, Satyapal et al., (2013), realizaram a nitretação a plasma em 350, 400, 450 e 500 °C no aço inoxidável duplex grau 2205, mantendo-se constantes os demais parâmetros de processamento (tempo de 4 h, pressão de 5 mbar, mistura de gases de 80 % $N_2$ e 20 % $H_2$). No trabalho destacou-se a avaliação do efeito da temperatura na rugosidade, dureza e microestrutura da superfície e a resistência à corrosão mediante polarização potenciodinâmica em soluções de 3,5 % NaCl e 1 % HCl. A caracterizações das amostras nitretadas mostraram que as nitretações realizadas nas temperaturas de 350 e 400 °C apresentaram uma camada composta de austenita e ferrita expandida. O aumento da temperatura, promoveu o deslocamento dos picos referentes a difração das fases ferrita e austenita devido à maior difusão de nitrogênio que finalmente resultou na formação de nitretos de cromo e ferro (CrN, $Fe_3N$) entre 450 e 500 °C (Figura 4).

**Figura 4 - Gráfico de DRX das amostra nitretada a plasma e não tratada.**

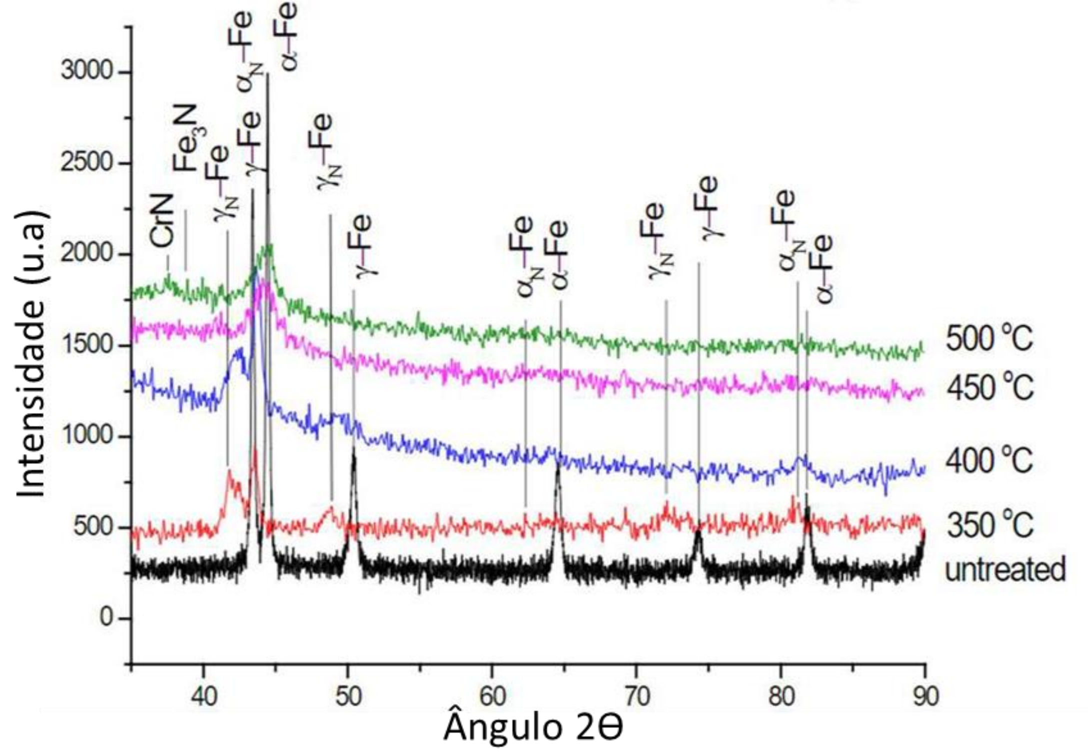

**Fonte: Satyapal et al., 2013.**

Os autores indicam que os parâmetros de rugosidade e dureza da superfície das amostras nitretadas aumentaram conforme aumenta a temperatura de nitretação como consequência do *sputtering* e a aparição de nitretos (450 e 500 °C) (Figura 5).

**Figura 5 - Efeito da rugosidade (a) e da dureza (b) em função da temperatura para as amostras nitretadas e não tratada.**

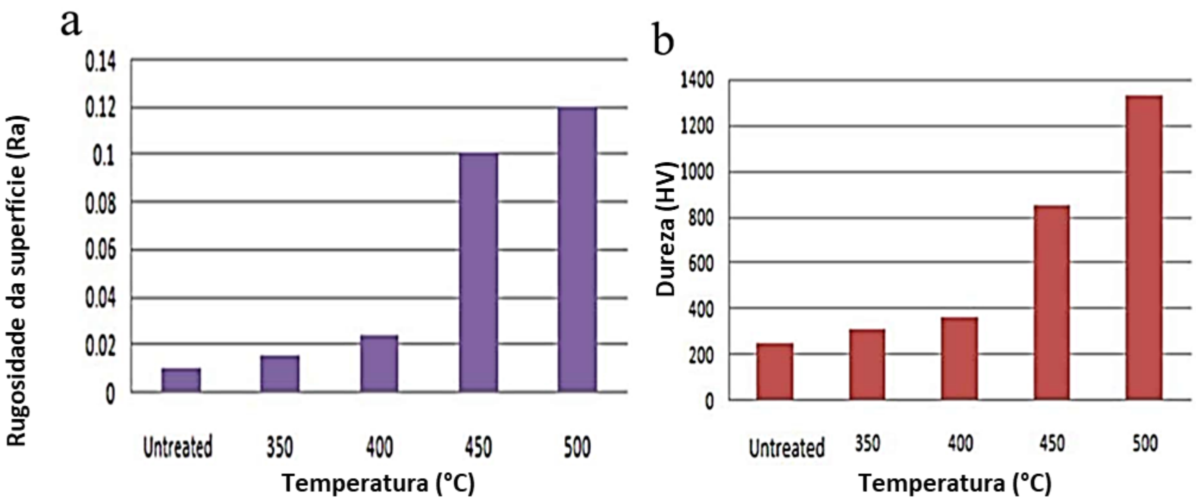

**Fonte: Satyapal et al., 2013.**

Salienta-se que ensaios de polarização potenciodinâmica nas amostras nitretadas a plasma a 350 e 400 °C apresentaram melhor resistência à corrosão do que as amostras no estado de fornecimento e nitretadas em 450 e 500 °C (Satyapal et al., 2013). Segundo os autores, para as amostras tratadas em 450 e 500 °C os nitretos formados levaram ao esgotamento do cromo da solução sólida, e consequentemente impossibilitou a formação do filme de óxido de cromo uniforme e continuo na superfície (Figura 6). Sendo que as amostras nitretadas em temperaturas abaixo de 400 °C apresentaram fases expandidas e o aço se apresenta mais resistente à corrosão nos ambientes avaliados.

**Figura 6 - Curvas de polarização potenciodinâmica para amostras não tradas e nitretadas em (a) NaCl 3,5 % e (b) 1 % HCl.**

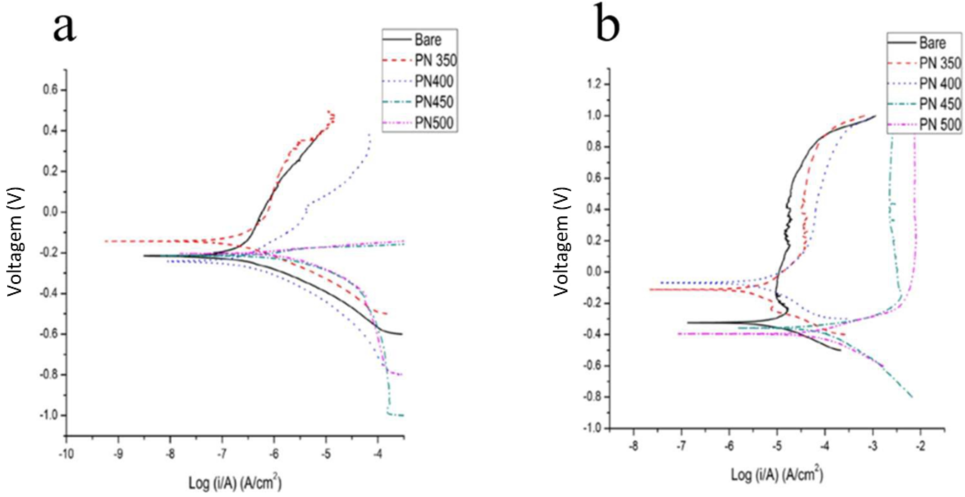

**Fonte: Satyapal et al., 2013.**

Pintaude et al., (2019), estudaram o efeito da NPBT na resistência à corrosão e à abrasão de dois graus de AID, o SAF 2507 (UNS S32750) e SAF 2205 (UNS S32205). Ambos os aços foram tratados usando um reator a plasma "*active screen*" com uma temperatura de 380 °C, sob pressão de 0,75 mbar por um tempo de 10 h numa atmosfera gasosa de 25 % $N_2$ e 75 % $H_2$. As amostras nitretadas foram caracterizados em termos da dureza, resistência ao desgaste e à corrosão. Resultados de difração de raios-X nas amostras tratadas, mostraram que a NPBT gerou uma camada composta por austenita expandida devido a dissolução de nitrogênio na austenita para ambos os aços. Imagens das seções transversais das amostras nitretadas mostraram a formação de finas camadas homogêneas de 1,48 ± 0,14 µm para SAF 2507 e 1,62 ± 0,26 µm para SAF 2205, com durezas superiores (SAF 2750; de 429 ± 12 para 870 ± 60 $HV_{0.025}$) e (SAF 2205; de 333 ± 10 para 780 ± 50 $HV_{0.025}$). Logo as amostras nitretadas foram conduzidas para análise de resistência ao desgaste mediante ensaios de riscamento num tribômetro (teste tipo *scratch*). Resultados mostraram que a maior dureza do aço SAF 2507 apresentou melhor desempenho em relação ao aço SAF 2205. O aço SAF 2205 nitretado apresentou mais trincas após o teste de riscamento, decorrente de seu alto coeficiente de atrito e menor resistência ao desgaste devido a maior fragilidade da camada de $\gamma_N$ (Figura 7). Os autores, já baseados nos ensaios de corrosão (polarização potenciodinâmica) encontraram que ambos os aços nitretados apresentaram melhor desempenho frente a corrosão devido a que seus potenciais de corrosão foram mais nobres do que os estados de fornecimento além dos menores valores de densidade de corrente de corrosão e potencias de pites (Figura 8).

**Figura 7 – Imagens MEV das superfícies nitretadas no (b) SAF 2205 e (d) SAF 2507 ensaiadas mediante *scratch* em carga constante de 5 N.**

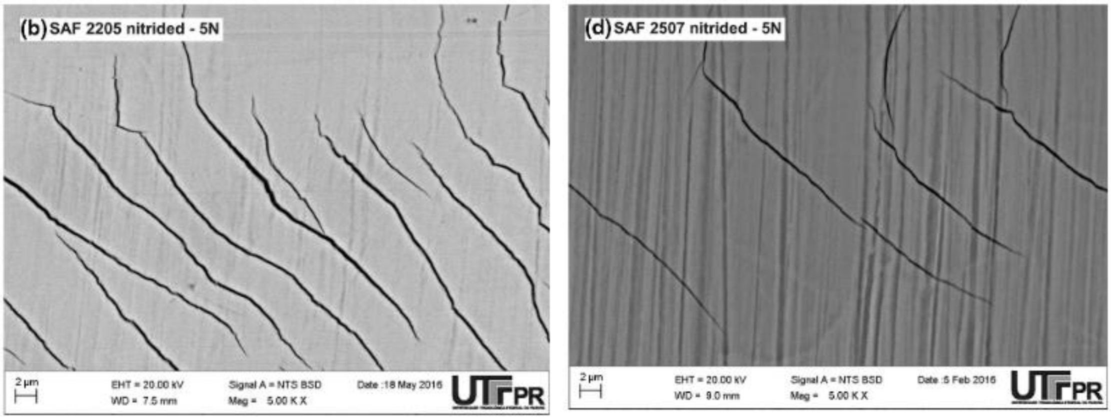

**Fonte: Pintaude et al., 2019.**

**Figura 8 - Curvas de polarização adquiridas em NaCl 0,6 M de amostras não tratadas e nitretadas de (a) aço SAF 2205 e (b) aço SAF2507.**

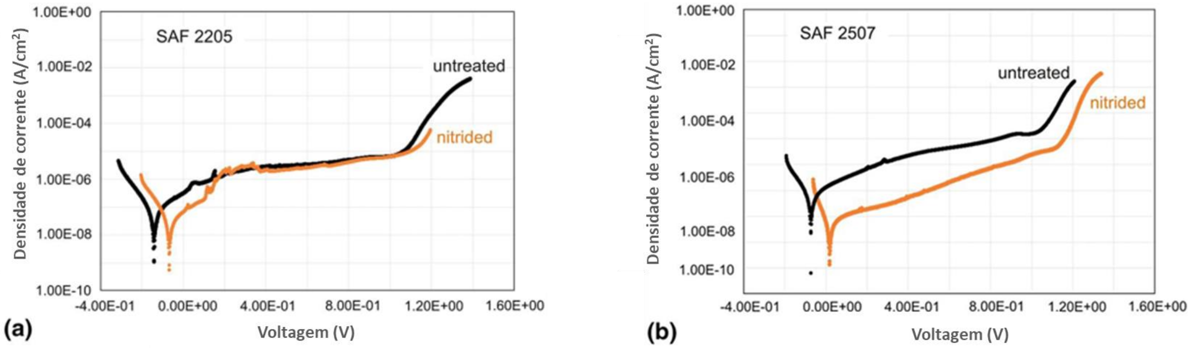

**Fonte: Pintaude et al., 2019.**

Shen et al., (2020), estudaram a corrosão localizada do AID UNS S32205 nitretado por plasma em baixas temperaturas. As condições de nitretação empregadas neste estudo foram: temperatura de 460 °C por 1 h, sob tensão de 600 V e corrente de 4,5 A. Amônia pura foi introduzida na câmara e decomposta por descarga incandescente sob uma pressão de trabalho de 300 Pa. Os autores reportam a formação de uma camada de austenita expandida $\gamma_N$ sem presença de nitretos de cromo (Figura 9), com espessura de 3 µm.

Figura 9 - Padrões de difração de raios-X de amostras de AID 2205 (a) como recebidas e (b) nitretadas.

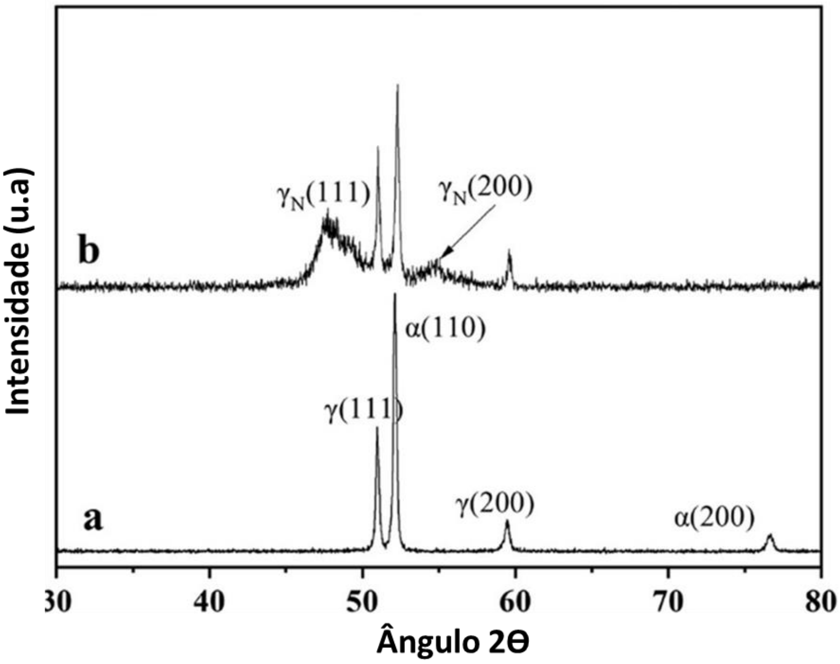

Fonte: Shen et al., 2020.

Ensaios de polarização potenciodinâmica em soluções 0,5 M $H_2SO_4$ + 2 ppm $F^-$ a 70 °C foram realizados em ambiente aerado e desaerados com $H_2$.

Resultados para ambos os casos mostraram uma diminuição das densidades de corrente de corrosão, potenciais de corrosão e de pites mais nobres o que indica melhoras na resistência a corrosão do AID UNS S32205 nitretado (Figura 10).

Figura 10 - Curvas de polarização potenciodinâmica de AID 2205 não tratado e nitretado em 0,5 M $H_2SO_4$ + 2 ppm $F^-$ a 70 °C quando borbulhado com (a) ar e (b) hidrogênio.

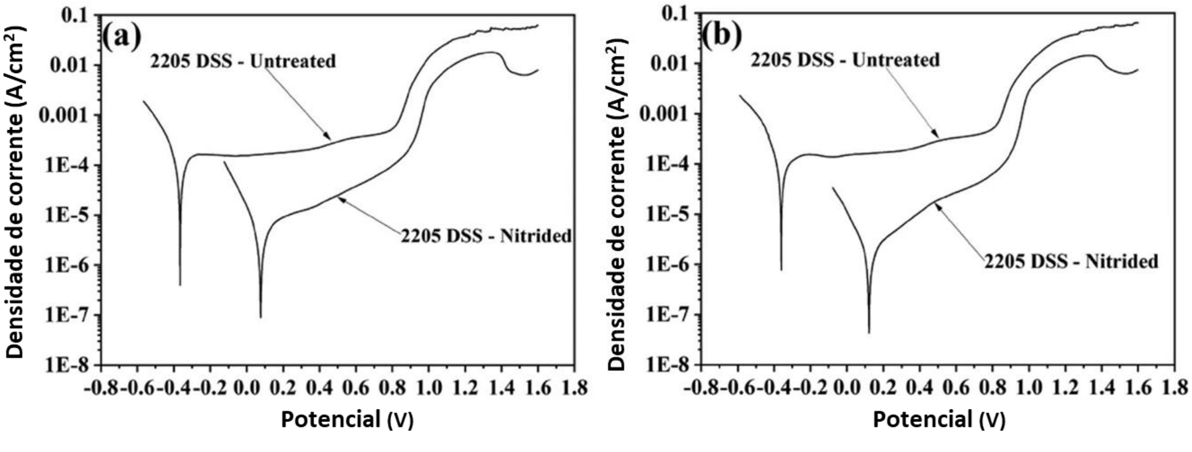

Fonte: Shen et al., 2020.

Haruman et al., (2020), estudaram o comportamento frente à tribocorrosão de aços 316L e 2205 nitretados em baixas temperaturas. Um forno tubular gasoso foi usado para realizar o tratamento de nitretação a 450 °C por 10 h, em atmosfera de gás de 75 % de $NH_3$ misturado com 25 % de $N_2$. Caracterizações microestruturais mostraram a formação de uma camada da fase expandida S, em ambos os aços, sendo mais espessa e dura no 2205 do que no 316L (Figura 11).

**Figura 11 - Padrões XRD (radiação Cu Kα) das amostras, mostrando a formação de camadas da fase S ($\gamma_N$) nas amostras tratadas.**

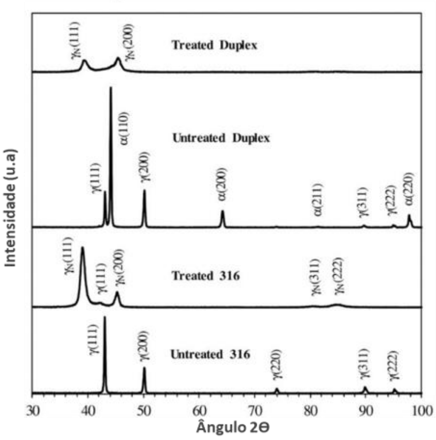

**Fonte: Haruman et al., 2020.**

Ensaios de polarização potenciodinâmica com e sem deslizamento mostraram melhora em ambos os aços nitretados, apresentando diminuição da densidade de corrente e aumento do potencial de corrosão e pites comparado com os aços sem tratar (Figura 12). Já o efeito sinérgico de desgaste e corrosão foi conduzido em um tribômetro recíproco a temperatura ambiente (22 °C) sob carga de 10 N em NaCl ao 3,5 % e frequência de 2 Hz, resultando em uma redução da perda de material em 5 a 70 vezes devido a fase S em ambos os materiais (Figura 13).

**Figura 12 - Curvas de polarização medidas durante o teste potenciodinâmico (a) sem deslizamento e (b) com deslizamento (2 N, 2 Hz).**

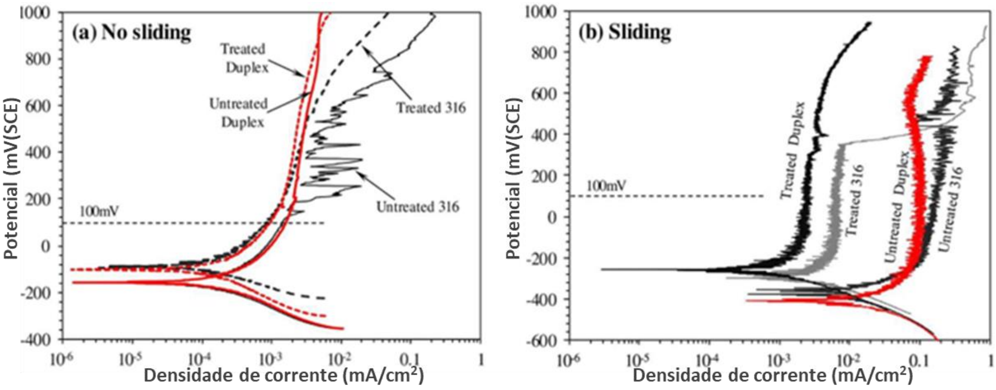

**Fonte: Haruman et al., 2020.**

**Figura 13 - Perda total de material medida das pistas deslizantes produzidas em OCP sob carga de 10 N em solução de NaCl ao 3,5 %.**

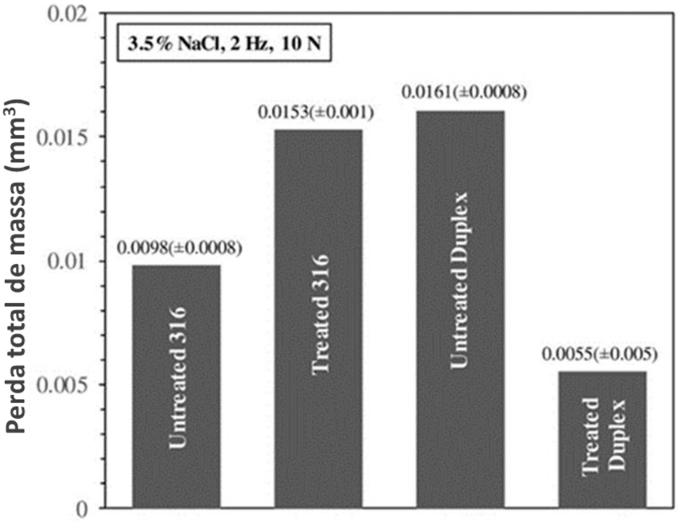

**Fonte: Haruman et al., 2020.**

## 4.3 Solda no AID

O desenvolvimento de peças, válvulas, tubulações e tanques com AID que a indústria demanda, requerem processos de soldagem que mantenham as propriedades de resistência mecânica e á corrosão. Os processos de solda comumente empregados nestes aços segundo a literatura são: GMAW (*Gas Metal Arc Welding*) (Azzi & Klemberg-Sapieha, 2011; Borges et al., 2019; Luchtenberg et al., 2019), FCAW (*Flux-Cored Arc Welding*) (Gnanasundaram & Natarajan, 2014; Zappa et al., 2017), SAW *(Submerged Arc Welding*) (Luo et al., 2013), SMAW (*Shield Metal Arc Welding*) (Aguilar-Sierra et al., 2015; Elsaady et al., 2018) e GTAW (*Gas Tungsten Arc Welding*) (Geng et al., 2015; Heider et al., 2020; Tahaei et al., 2016; Zappa et al., 2017).

Todos os processos acima mencionados, dependendo dos parâmetros de solda, podem gerar mudanças no balanço percentual de ferrita-austenita do AID desde a zona fundida (ZF) até a zona termicamente afetada (ZTA) devido aos gradientes térmicos os quais são função da velocidade de avanço, corrente e da tensão (Fonseca et al., 2016; Rodriguez et al., 2020; Roldão, 2010; Videira, 2016).

Algumas pesquisas sugerem que o aporte térmico recomendado para AID UNS S32205 deve estar em torno dos 0,5 kJ/mm até 2,5 kJ/mm (Eghlimi et al., 2014; Elsaady et al., 2018; C. S. Fonseca et al., 2016a; Kotecki, 2010; Luchtenberg et al., 2019; Yousefieh et al., 2011).

Fonseca e Pinheiro, (2016) e Grilo et al., (2017) estudaram a influência do aporte térmico sobre a morfologia da austenita e na quantidade das fases obtidas em chapas de AID

SAF 2205 e UNS S32304 ambas as duas soldadas pelo processo de solda GMAW, foram utilizados como consumível arame Autrod 2209 e Autrod 2509, respectivamente. Os parâmetros operacionais de corrente, e de tensão mantiveram-se fixos (28 V e 200 A; 32 V e 300 A) e variando a velocidade de avanço para assim obter diferentes valores de aporte térmico (0,5 kJ/mm, 1,0 kJ/mm e 1,5 kJ/mm; 0,7 kJ/mm, 1,09 kJ/mm, 1,32 kJ/mm e 1,87 kJ/mm). Verificou-se que o maior valor de aporte térmico, obtido para a menor velocidade de avanço, influenciou na mudança nas morfologias das fases austenitas, sendo a mais importante a presença da austenita de Widmanstätten (AW) com consequentemente diminuição da fase ferrita no aço SAF 2205 (Figura 14) e um aumento para o aço UNS S32304. Em ambos os casos segundo os autores, não houve presença de fases prejudiciais como a Laves, a chi, a sigma e carbonetos nas condições de soldagem utilizadas.

**Figura 14 - Diferentes morfologias da austenita, em amostras soldadas com aporte térmico de a. 0,5 kJ/mm, b. 1,0 kJ/mm e c. 1,5 kJ/mm sendo 1: austenita intragranular (AIG), 2: austenita de contorno de grão (ACG) e 3: austenita de Widmanstätten (AW).**

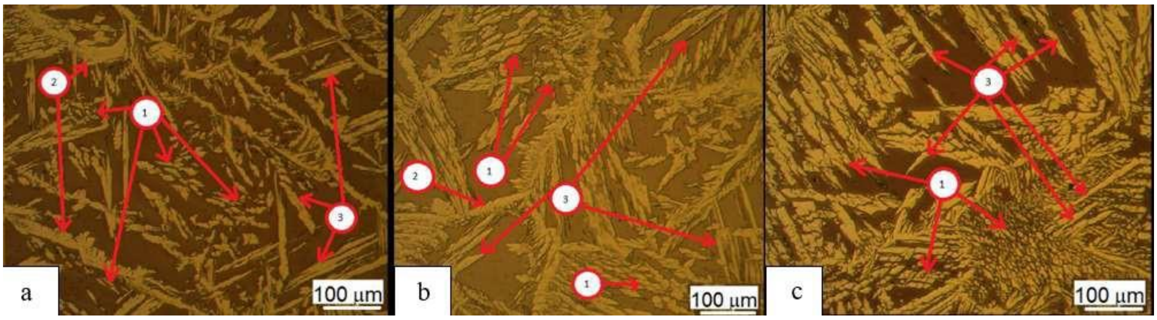

**Adatado de: Fonseca et al., 2016.**

Magalhães *et al*., (2019), também estudaram o efeito da energia de soldagem em um AID (UNS S32304) mediante o processo de solda SMAW empregando arame consumível AWS E2209-17, nesse trabalho foi constatado que com o aumento da energia de soldagem também reduz a relação ferrita/austenita.

Já o processo GTAW é um dos processos que fornece um melhor balanço das fases ferrita e austenita quando comparado com outros processos de soldagem (Moraes e Videira, 2016; Pereira, 2009; Yousefieh et al., 2011) segundo é sugerido pelas normas (NORSOK Standard, 2016; TAPPI, 2001). Videira, (2016) estudou o efeito do aporte térmico no processo de solda GTAW. Ele observou presença de austenita com morfologia de AW na ZF e ACG, além disso, na ZTA foi observado a formação de uma faixa com maior percentual de ferrita. Por outro lado, no trabalho de Geng et al., (2015) foi estudada a evolução da microestrutura do AID 2205 soldado pelo processo GTAW (AWS A5.9 ER2209), os resultados indicaram que durante o resfriamento da ZF, formou ACG nos contornos da ferrita por causa da maior energia livre nesses locais, na sequência a AW nucleou a partir do ACG e cresceu para o interior da ZF em um determinado ângulo, ao mesmo tempo, uma grande quantidade de AIG surgiu nos grãos de ferrita devido ao alto teor de níquel do arame consumível e a presença de austenita secundaria $(\gamma_2)$. Neste caso, o balanço das fases foi levemente alterado, sendo a ferrita aquela que teve uma menor porcentagem.

### 4.3.1 Dureza do AID soldado

A dureza do MB do AID depende das fases individuais de austenita e ferrita presentes em sua microestrutura, sendo estes valores aproximadamente iguais (Calabokis, 2020; C. S. Fonseca et al., 2016). Quando é comparada a dureza do MB com ZF, dependendo do processo e do aporte térmico, a dureza pode variar devido taxa de resfriamento.

Luchtenberg et al., (2019) avaliaram a influência do aporte térmico na dureza em chapas de aço carbono (ASTM A 516 Gr 60) submetida a deposição pelo processo de solda GMAW. Para isso foi utilizado como arame consumível AWS A5.9 ER2209 e três diferentes valores de aportes térmicos (0,53 kJ/mm, 1,01 kJ/mm, 1,27 kJ/mm e 1,74 kJ/mm) visando obter propriedades similares as do AID UNS S32205. Os resultados apresentados, mostraram que o equilíbrio de austenita e ferrita muda com a energia de soldagem, para todos os casos. Em todas as condições de energia de soldagem, surgiram quatro tipos diferentes de morfologias de austenita (AIG, ACG, AW e austenita parcialmente (APT)). Luchtenberg et al., (2019) observaram que as durezas de topo dos revestimentos de solda foram maiores do que os valores de dureza de uma chapa laminada de AID UNS S32205 (Figura 15).

**Figura 15 – Perfis de dureza em função do aporte térmico comparados com a dureza do AID UNS s32205.**

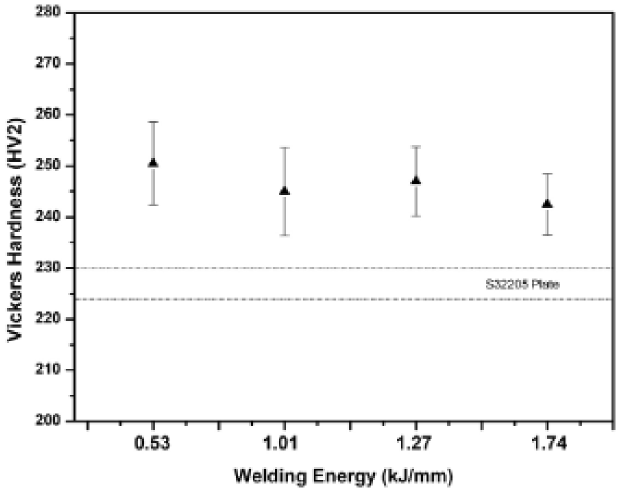

**Fonte: Luchtenberg et al., (2019).**

Este resultado foi atribuído ao grande número de interface austenita/austenita e austenita/ferrita. Essas interfaces dificultam o movimento de discordâncias, tornando os revestimentos mais duros e consequentemente, difíceis de deformar plasticamente pelo indentador Vickers.

No trabalho de Moraes e Videira, (2016), verificou-se que o AID UNS S32205 soldado pelo processo GTAW, apresentou valores de dureza que diminuem conforme aumentou aporte térmico, sendo todos estes valores levemente maiores à dureza do MB. Resultado oposto foi obtido pelo Geng et al., (2015), onde observou-se que o valor de dureza na ZF é menor do que no MB. Conforme se afasta da ZF para o MB, a dureza aumenta até um máximo na ZTA e logo cai até o valor de dureza do MB, devido principalmente à formação de precipitados de nitretos de cromo.

### 4.3.2 Corrosão no AID soldado

A escolha do procedimento de solda e seus parâmetros (corrente, potencial, velocidade e aporte térmico), o metal de adição, os materiais a serem soldados e o gás de proteção, desempenham papéis fundamentais para alcançar uma boa resistência à corrosão em uma solda. Um bom desempenho frente a corrosão de uma peça soldada é muito mais desafiador do que chapas de aço, as quais passaram por processos de laminação, tratamento térmico e decapagem na usina siderúrgica (Heider et al., 2020).

Para a série de AID, é essencial garantir condições próximas ao equilíbrio de fase austenita- ferrita na ZF e na ZTA, além de evitar a precipitação de fases prejudiciais como intermetálicos, carbonetos e nitretos. As características microestruturais mencionadas dependem principalmente do aporte térmico e da taxa de resfriamento. A microestrutura também possuem forte influência do tamanho do grão e da distribuição dos elementos de liga no inicio do resfriamento da junta soldada. Além disso, a importância de uma boa limpeza e tratamento térmico pós-soldagem para garantir boas propriedades de corrosão, não pode ser subestimada. Na sequência, serão descritos os fatores que afetam a resistência à corrosão dos AID soldados através de diferentes processos de soldagem e as técnicas eletroquímicas utilizadas para a sua avaliação baseado em pesquisas previas.

O trabalho de Zhang et al., (2017) mostra detalhadamente a susceptibilidade das diferentes fases cristalinas da microestrutura de uniões soldadas do aço duplex UNS S31803 utilizando o consumível E2209. A junta soldada multipasse foi fabricada pelo processo FCAW. A influência da evolução microestrutural na corrosão seletiva em junta de soldagem foi investigada pela reativação potenciocinética eletroquímica de circuito duplo modificado (DL-

EPR, *modified double loop electrochemical potentiokinetic reactivation*) em solução de 2 M $H_2SO_4$ + 1 M HCl na temperatura 35 ± 1 °C.

A composição microestrutural da junta soldada multipasse FCAW variou dependendo da região da solda, como apresentado na Figura 16 (Zhang et al., 2017). A austenita primária ($\gamma_1$) é aquela que solidificou diretamente do metal fundido. Enquanto a austenita secundária ($\gamma_2$) nucleia nos contornos $\gamma/\alpha$ ou no interior da ferrita tendo diferentes morfologias: AW, ACG, AIG e APT. A junta soldada FCAW, também apresentou outros componentes microestruturais como $Cr_2N$, fase $\sigma$ e inclusões como esquematizado na Figura 16.

**Figura 16 - Diagrama esquemático da evolução microestrutural e da corrosão seletiva de diferentes fases na junta AID pelo processo FCAW após o teste DL-EPR em solução desareada de 2 M $H_2SO_4$ + 1 M HCl a 35 °C: zona fundida ZF (a, b), zona termicamente afetada ZTA (c, d) e metal base (e, f).**

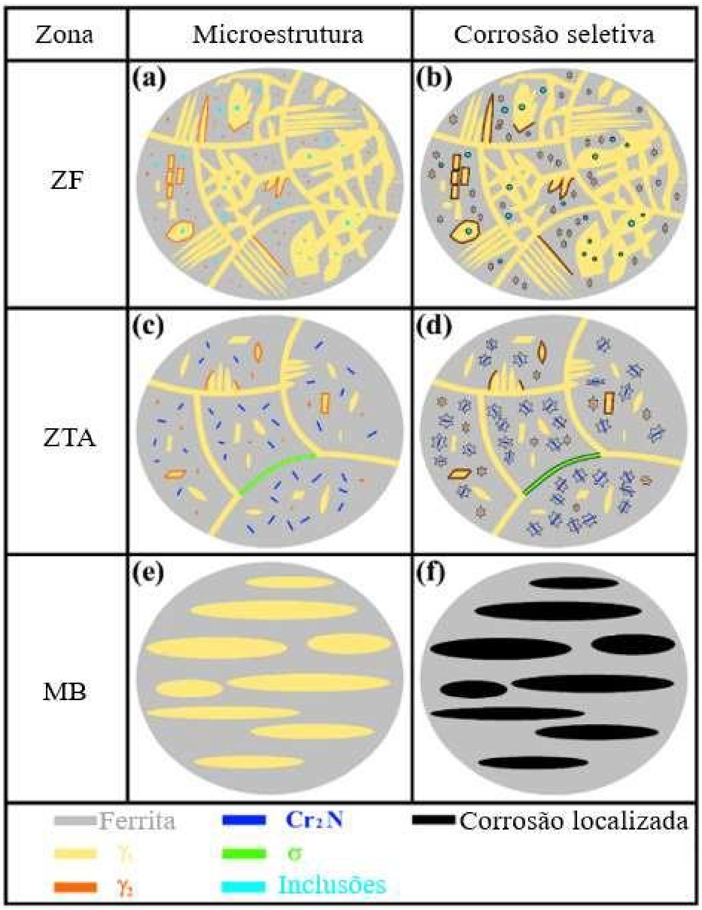

**Fonte: Zhang et al., 2017.**

Os ensaios DL-EPR revelaram que no cordão de solda (ZF), as austenitas secundárias de contorno de grão e intragranular e as inclusões atuaram como pontos de nucleação de micropites, resultado esquematizado na Figura 16 Zhang et al., (2017). Na região ZTA, a corrosão por pites e intergranular aconteceu por dissolução preferencial das regiões de depleção de cromo: em torno dos precipitados $Cr_2N$ e fase σ. Na ZTA, a austenita secundária $\gamma_2$ também foi mais susceptível a corrosão comparada com a austenita primária $\gamma_1$ e ferrita α. No caso do metal base MB, sofreu corrosão preferencial nos grãos austeníticos devido ao menor número equivalente de resistência à corrosão por pites (PREN), comparada com os grãos ferríticos.

Resultados semelhantes foram obtidos por Zhang et al., (2017), que afirmam que as diferenças de resistência a corrosão por pites entre as zonas ZF, ZTA e MB são principalmente devidas às diferenças do PREN entre as fases ferrita e as diferentes austenitas e o balanço de fases. Zhang et al., (2017) avaliaram a resistência a corrosão por pites segundo a ASTM G150-18 e polarização potenciodinâmica na solução 1M NaCl em 60 °C em chapas de UNS S31803 unidas pelo processo de soldagem GTAW.

A relevância do trabalho de Zhang et al., (2017) encontra-se no estudo detalhado da susceptibilidade à corrosão dos componentes microestruturais ao longo do material soldado, porém, estudos similares também foram realizados por Geng et al., (2015) utilizando polarização potenciodinâmica em 3,5 % NaCl.

Geng et al., (2015) realizaram um estudo meticuloso da resistência a corrosão nas diferentes zonas da solda entre chapas, sendo a zona 1 o centro do cordão de solda (ZF), zona 2 a linha de fusão (transição entre ZF e ZTA), e subsequentemente as zonas 3, 4 e 5 conforme se afasta do cordão e atinge o metal base. O processo de soldagem utilizado foi GTAW (eletrodo ER 2209) para chapas de UNS S32205.

**Figura 17 - Curvas de polarização potenciodinâmica em solução 3,5 % NaCl das diferentes regiões do aço UNS S32205 soldado pelo processo GTAW. A Zona 1 situa-se no centro da zona fundida ZF e na sequência em ordem crescente são enumeradas (zona 2, 3, 4, 5) conforme se afasta desta região até atingir o metal base.**

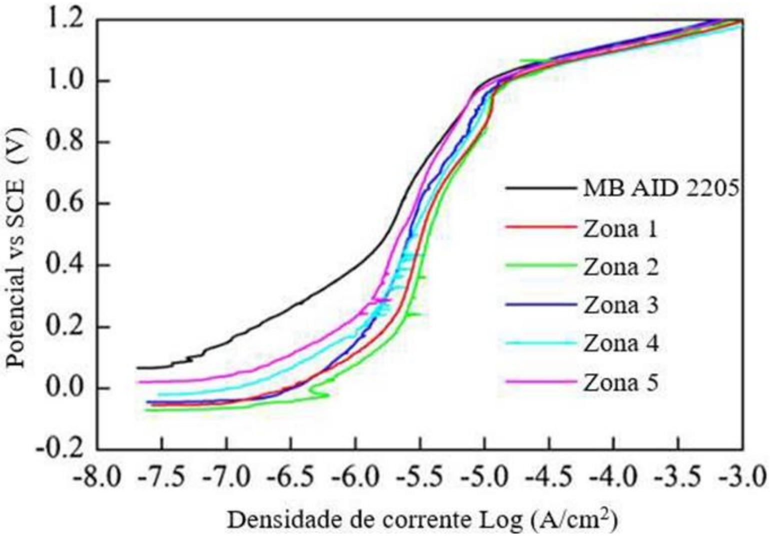

**Fonte: Geng et al., 2015.**

A resistência a corrosão, vista tanto com aumento da corrente de corrosão ($I_{corr}$) quanto pela diminuição do potencial de corrosão ($E_{corr}$), seguiu a seguinte ordem: zona 2 < zona 1 < zona 3 < zona 4 < zona 5 < metal base (Figura 17). A zona 2 apresentou a maior susceptibilidade à corrosão generalizada devido a dois aspectos: (i) possui tamanho de grão de ferrita mais grosseiro, maior fração de volume de ferrita e heterogeneidade microestrutural do que quaisquer outras zonas; (ii) contém uma grande quantidade de nitretos de cromo na interface austenita-ferrita e dentro dos grãos de ferrita. Em seguida a zona 1 em termos de resistência a corrosão, devido à formação de austenitas secundárias, que são mais susceptíveis que a ferrita e austenita primária devido a seu menor teor de Cr, Mo e N, resultado concordante com os estudos de Zhang et al., (2017). Contudo, segundo o trabalho de Pardal et al., (2011), a presença de traços de fases deletérias, microporosidades e a presença de pequenos precipitados de fase σ e de $Cr_2N$ menores que 3 μm na ZTA da raiz do cordão de solda, não tiveram influência no comportamento frente a corrosão da junta. No entanto, esses resultados mostraram-se fortemente influenciados pelos superiores percentuais de nitrogênio (N), molibdênio (Mo) e tungstênio (W) nas regiões ZTA e ZF tanto da raiz (soldada pelo processo GTAW) e da solda (enchimento e acabamento pelo processo SAW). Os maiores teores são resultado da utilização de eletrodo consumível superduplex (ER 2594, com composição química aproximada 25 %Cr, 10 %Ni, 4 %Mo) para união de aço duplex UNS S31803.

Os autores Geng et al., (2015), baseados nos resultados de polarização potenciodinâmica (Figura 17) salientam que não houve diferenças importantes na corrente de passivação nem no potencial de nucleação de pites entre as diferentes zonas (1, 2, 3, 4 e 5) e o metal base apesar das diferenças na microestrutura, composição química e morfologias. Ao respeito, Múñez et al., 2007 determinaram que a linha de fusão da solda, equivalente à zona 2 da pesquisa de Geng et al., 2015, é o local preferencial para a nucleação de pites devido ao maior conteúdo de precipitados de carbonetos e nitretos nas uniões de UNS S32205 mediante processo GMAW (eletrodo ER 2209).

Conforme discutido, a variedade microestrutural das juntas de solda em AID acontece em todos os processos de solda (por exemplo GTAW, GMAW, SMAW, SAW, sendo sempre decisiva a escolha dos parâmetros do processo de soldagem afim de evitar as fases deletérias (carbonetos e nitretos, fase σ) e manter o balanço entre as frações volumétricas de γ e α superior à 25-30 %, conforme as especificações norma TAPPI TIP 0402-29 e Norsok M601. No trabalho de Luchtenberg et al., (2019) também foi estudado o efeito da energia de soldagem, ou aporte térmico, no processo de revestimento por solda GMAW/CMT (*weld overlay*) do arame consumivel ER 2209 sobre uma chapa de aço carbono (ASTM A 516 Gr 60). Modificando a velocidade de deposição do consumível ER 2209, foram obtidos diferentes aportes térmicos, cujos efeitos na microestrutura e na resistência á corrosão são mostrados na Figura 18.

**Figura 18 - a. Quantidade relativa de fases presentes no revestimento por solda de AID ER 2209 e b. Curvas de polarização potenciodinâmica em 3,5 % NaCl; em função da energia de soldagem.**

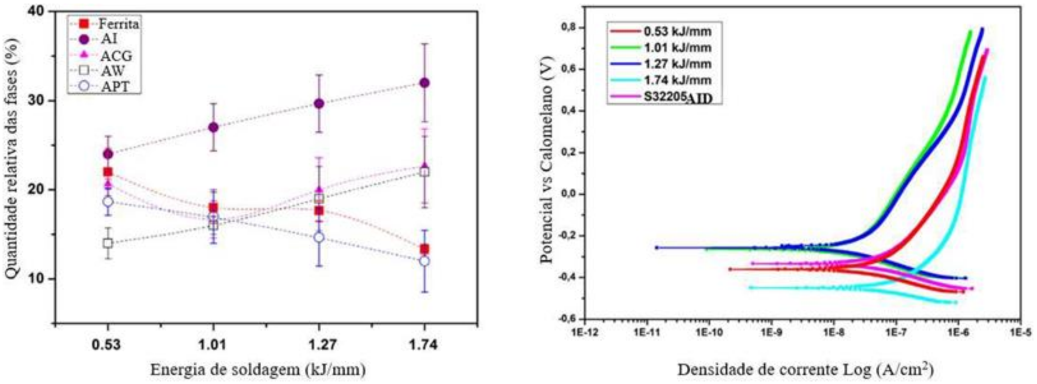

**Fonte: Luchtenberg et al., 2019.**

Segundo Luchtenberg et al., (2019), a Figura 18a, quanto maior a energia, maior quantidade de $\gamma_2$ do tipo AIG e AW e alteração do equilíbrio das fases ferrita/austenita para menores quantidades de ferrita. A resistência à corrosão dos revestimentos de solda, avaliada por polarização potenciodinâmica em 3,5 % NaCl, mostrou que a condição de maior energia de soldagem 1,74 kJ/mm (com maior fração de austenita secundária) apresentou a menor resistência à corrosão de todas as condições, comparado com a peça laminada de UNS S32205 (Figura 18b). O pior comportamento de corrosão está relacionado aos baixos teores de Cr, N, Mo nas austenitas secundárias (Luchtenberg et al., 2019). Enquanto as outras três condições de energia mostraram-se semelhantes ou até melhores referentes as caraterísticas de resistência à corrosão ($E_{corr}$, $i_{corr}$, $i_{pass}$) comparada com a placa S32205 laminada. No trabalho de Luchtenberg et al., (2019), faltou a avaliação da resistência à corrosão do substrato (aço carbono ASTM A 516 Gr 60), com objetivo de salientar a efetividade na proteção do substrato utilizando tratamentos de revestimentos por solda com ligas de superior resistência a corrosão.

O controle do aporte térmico, precisa vir acompanhado do controle da taxa de resfriamento. Heider et al., (2020) demonstraram que elevados aportes térmicos e prolongadas taxas de resfriamento podem causar difusão desigual do cromo na matriz para os contornos de grão com a formação de uma rede de carbonetos de cromo neles, levando a corrosão localizada intergranular. Apesar disso, a resistência à corrosão em água de mar sintética da superfície soldada (revestimento) de AID (consumível de composição similar ao UNS S32205) foi em todas as condições de soldagem superior ao substrato de ferro fundido cinzento (EN-GJL-250);

deposição realizada por GMA-SW (*gas metal arc surface welding*) e PTA-SW (*plasma transferred arc surface welding*). Os autores Eghlimi et al., (2015) também salientaram que as diferenças na resistência a corrosão avaliada mediante ensaios de polarização cíclica em 1M de NaCl e ensaios de temperatura crítica de pites (ASTM G150), dependeram do efeito do aporte térmico na obtenção do melhor balanço de austenita/ferrita (tendência 50/50), o engrossamento dos grãos e o menor teor de $Cr_2N$.

Eghlimi et al., (2015) também avaliaram revestimentos por soldagem de aço inoxidável super duplex (ER2594N SDSS, composição química equivalente a UNS S32750) em substratos de aço de baixa liga de alta resistência (0,26 % C) pelo processo de soldagem GTAW (arco de tungstênio) usando correntes pulsadas e constantes.

Os trabalhos previamente citados de (Eghlimi et al., 2015; Heider et al., 2020; Luchtenberg et al., 2019; Zappa et al., 2018) estudaram o efeito do aporte térmico em processos de soldagem por revestimentos utilizando AID como material de adição. Porém o efeito do aporte térmico na resistência a corrosão de juntas soldadas de AID, depende também das fases, a microestrutura e a composição química resultante, assim como nos processos de revestimento por soldagem. De fato, Shin et al., (2019) examinaram o efeito da corrente no processo de soldagem por pontos de resistência RSW (*resistance spot welding*) no comportamento de corrosão do UNS S32750. As mudanças na corrente de soldagem afetaram tanto a largura, a microestrutura e composição química das zonas ZF e ZTA, porque o aporte térmico (energia de entrada de calor) foi incrementado conforme o aumento da corrente. Em consequência, houve um aumento da fração volumétrica da ferrita com segregação de Cr, Ni e Mo nestes grãos, o que diminuiu os valores dos potenciais de corrosão e de nucleação de pites (*Ecorr* e *Epit*) nos ensaios de polarização potenciodinâmica em 3,5 % NaCl, como apresentado na Figura 19.

**Figura 19 - Efeito da corrente de soldagem nas curvas de polarização potenciodinâmica do aço UNS S32750 soldado pelo processo RSW. Solução de 3.5 % NaCl.**

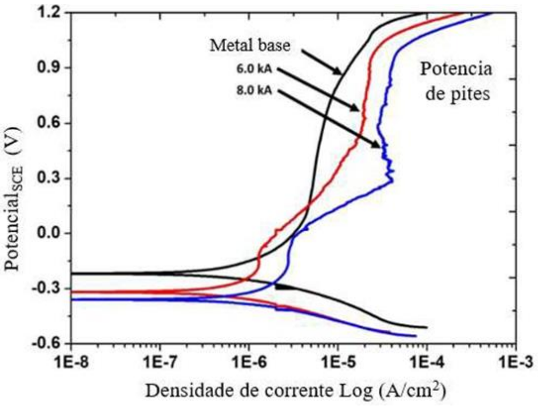

**Fonte: Shin et al., 2019.**

Em resumo, a resistência a corrosão dos AID soldadas utilizando diferentes processos de soldagem, depende do: equilíbrio de fases austenita-ferrita na ZF e na ZTA; da formação de precipitados de fases deletérias como intermetálicos, fase sigma, fase chi, carbonetos e nitretos; da formação de austenitas secundárias e da distribuição dos elementos de liga entre as fases.

Como foi visto, estas características microestruturais dependem da escolha dos parâmetros do processo, principalmente da entrada de calor e da taxa de resfriamento, sendo sempre necessária uma avaliação completa e detalhada da microestrutura ao longo da solda para elucidar o comportamento frente a corrosão obtido.

A literatura encontra-se focada no estudo da resistência a corrosão em meios contendo cloretos, utilizando principalmente as técnicas de polarização potenciodinâmica e de temperatura crítica de pites (TCP ASTM G150). Contudo, algumas outras técnicas também têm sido utilizadas como a reativação potenciocinética eletroquímica de circuito duplo modificado (Zhang et al., 2017), impedância eletroquímica (Heider et al., 2020) e ensaios de imersão (Elsaady et al., 2018). Desta forma, a revisão bibliográfica realizada em soldagem de AID indica que existem muitas alternativas para a avaliação da resistência à corrosão que faltam por estudar.

JMEPEG (2020) 29:2612–2622
https://doi.org/10.1007/s11665-020-04753-6

1059-9495/$19.00

# Effect of Low-Temperature Plasma Nitriding on Corrosion and Surface Properties of Duplex Stainless Steel UNS S32205

*Yamid E. Núñez de la Rosa, Oriana Palma Calabokis, Paulo César Borges, and Vladimir Ballesteros Ballesteros*

*(Submitted October 28, 2019; in revised form March 12, 2020; published online April 6, 2020)*

**The duplex stainless steel UNS S32205 was plasma nitrided at 380 °C for 10 h using a gas mixture of 25% $N_2$-75% $H_2$. The thickness of the nitrided layer was 4.5 ± 0.5 µm, composed mainly of nitrogen-expanded austenite and iron nitrides precipitates. There was an increase in surface hardness around 2.6 and 3.8 times in the nitrided layer formed on the austenite and the ferrite phases, respectively, in relation to the untreated samples. The surface texture parameters skewness ($S_{sk}$), maximum peak height ($S_p$) and texture aspect ratio ($S_{tr}$) were the most appropriate parameters for studying the topography changes after treatment. An improvement in the localized corrosion properties after the nitriding treatment was revealed by the cyclic polarization curves. The nitrided samples showed higher pitting corrosion and repassivation potentials compared to the untreated material. The ferritic phases and grain boundaries were more susceptible to corrosion in the nitrided samples. The potentiodynamic curves of the nitrided samples exhibited a hillside on the passive-to-transpassive transition. This feature was already observed by other researchers, but it has not been well investigated. Potentiostatic studies demonstrated that metastable pitting took place on this transition.**

**Keywords** corrosion, low-temperature plasma nitriding, metastable pitting, UNS S32205

## 1. Introduction

Duplex stainless steels (DSSs) have a two-phase microstructure with equivalent amounts of ferritic ($\alpha$) and austenitic ($\gamma$) phases. They are widely used in high-performance components for petrochemical, oil and gas, chemical and nuclear industries because of their superior strength and corrosion resistance, compared to the analogous austenitic steels. However, for some wear-resistant demanding applications, the bulk hardness is not enough to ensure the required performance (Ref 1-7).

Plasma nitriding is a thermochemical surface treatment expected to improve wear properties on duplex stainless steel (DSS) without decreasing the corrosion resistance. When this treatment is carried out at low temperatures (350-420 °C), it is possible to form a layer with higher hardness and better wear properties than the steel substrate (Ref 1-7). The nitrided layer formed at low temperatures is mainly composed by nitrogen-expanded phases without nitrides (Ref 8, 9). The chromium nitrides are formed when the treatment is carried out at higher temperatures ($>$ 420 °C). Those precipitates affect the corrosion performance because they create chromium-depleted regions which hinder the formation of the passive layer (Ref 5-7, 9-12).

Electrochemical techniques, such as electrochemical impedance spectroscopy and potentiodynamic polarization, are commonly used for corrosion studies. The current response is plotted as a function of the potential, when the metal is subjected to the potentiodynamic polarization. Some studies regarding plasma-nitrided DSS have reported polarization curves with a hillside on the passive-to-transpassive transition (Ref 2, 3, 13-17). This hillside was recognized in all cases by a continuous increase followed by a drop in current density at the end of the passivation region. This phenomenon, which has also been reported in the literature, has not been well explained, but it is believed that it is related to the partial rupture of the passive layer followed by its repassivation before the definitive rupture in the transpassive region.

Duplex stainless steels are susceptible to pitting corrosion in many chloride environments (Ref 18-21). Typical current–potential curves obtained by potentiodynamic polarization have a sudden current increase when the pitting potential ($E_p$) or breakdown potential is reached. This marks the passive-to-transpassive transition where localized corrosion and transpassive reactions could occur. However, it was demonstrated that pitting nucleation can occur at potentials far below the pitting potential, known as metastable pitting (Ref 22-25). Concerning DSS, metastable signals were evidenced in untreated UNS S32205 and UNS S32750 on the studies performed by Tang et al. and Garfias-Mesias and Sykes, respectively (Ref 26, 27). However, to our knowledge, metastable pitting has not been studied before in plasma-nitrided stainless steels despite the actual importance of these treated alloys.

In the present study, low-temperature plasma-nitrided UNS S32205 was characterized in terms of microstructure, hardness, surface roughness and corrosion behavior. Especially, this study

---

**Yamid E. Núñez de la Rosa, Oriana Palma Calabokis,** and **Paulo César Borges**, Universidade Tecnológica Federal do Paraná, Curitiba, Brazil; and **Vladimir Ballesteros Ballesteros**, Facultad de Ingeniería y Ciencias Básicas, Fundación Universitaria Los Libertadores, Bogotá D.C., Colombia. Contact e-mail: yamid@alunos.utfpr.edu.br.

emphasized the study of the current density hillside observed at the end of the passivation region.

## 2. Materials and Methods

### 2.1 Specimen Preparation

The stainless steel UNS S32205 was used as the substrate material. Table 1 presents the chemical composition of this material analyzed by mass spectroscopy.

The samples were cut by electro-erosion from a hot-rolled bar (diameter: 85.5 mm) up to the dimensions of (7 × 20 × 60) $mm^3$. Afterward, they were rectified to remove irregularities and grounded until 600 grit using SiC grinding papers. Finally, they were ultrasonically cleaned in acetone and dried under hot air.

### 2.2 Plasma Nitriding

Plasma nitriding treatments were carried out in a pulsed plasma reactor with a cold-wall chamber, located at the LabPlasma (UTFPR-Brazil). Prior to plasma treatment and in order to remove the surface oxide layer, sputter cleaning was done using a gas mixture of hydrogen and argon (75% $H_2$ and 25% Ar, 200 SCCM flux) at a pressure of 3 Torr (~ 400 Pa), a voltage of 600 V and a temperature of 300 °C for 20 min. The samples were arranged side by side to avoid border effect during plasma nitriding, and they were placed on the sample holder, which behaves as a cathode with respect to the chamber wall. The heating process was controlled by increasing the time that the pulse source was on and off, step by step until the set treatment temperature was achieved and stabilized for 10 min. During this time, the flux of argon was substituted for nitrogen (25% of $N_2$). The samples were then treated under the constant temperature, pressure, flux and voltage used during sputtering, for 10 h. After this process, the bias voltage and nitrogen flux decreased to zero and the specimens were cooled down to room temperature in a hydrogen gas atmosphere to avoid oxidation during cooling.

### 2.3 Characterization: Morphology and Hardness

The nitrided samples were cross-sectioned, compression mounted in bakelite and polished to a mirror finishing with successive SiC grinding papers and diamond paste. For revealing microstructure, they were electrochemically etched with a solution of oxalic acid (10 w/v% $C_2H_2O_4$) at 4.6 V for 10 s. Afterward, the microstructure of the nitrided layer was analyzed by light optical microscope (OM) equipped with image software.

3D Areal surface texture parameters were acquired by an optical interferometer equipped by commercial software which provided all the parameters defined in the ISO 25178 standard. A sampling area of 0.865 mm × 0.865 mm was analyzed with a resolution of 1024 × 1024 pixels. The most significant parameters of the surface changes after the treatment were chosen by the "average and standard deviation method" proposed by Helmli et al. (Ref 28, 29). This method analyses based on the significance $S_i$ (Eq 1) and threshold $\tau$ (Eq 2) values calculated for each surface texture parameter,

$$S_i = \frac{d\left(I'_i, I''_i\right)}{\frac{1}{2}\left(\mu'_i + \mu''_i\right)}, \qquad \text{(Eq 1)}$$

where $d\left(I'_i, I''_i\right)$ is the highest difference between the confidence intervals $I_i$ and $\mu_i$ is the average of each parameter for the untreated (′) and nitrided (″) surfaces. The significance $S_i$ represents which parameter was more sensitive between the initial and the final surface condition. The threshold value ($\tau$) was calculated by solving the quadratic equation for $\tau$:

$$\frac{\left(\tau - \mu''_i\right)^2}{2\sigma''_i} - \frac{\left(\tau - \mu'_i\right)^2}{2\sigma'_i} = \frac{\sigma'_i}{\sigma''_i}, \qquad \text{(Eq 2)}$$

where $\sigma'_i, \sigma''_i$ are the standard deviation of each surface parameter for the untreated and nitrided conditions, respectively. The threshold value is, in fact, the limit value of each roughness parameter used to differentiate between the surface conditions.

A diffractometer with radiation CuK-α ($\lambda$ = 1.5406 Å) using the $\theta$-2$\theta$ Bragg–Brentano configuration, a current of 30 mA, a voltage of 40 kV and a scan rate of 0.02°/s was used to scan the XRD patterns from 20° to 120° (2$\theta$). Also, the JCPDS cards were used for identifying the phase constituents: 00-006-0696 for ferrite, 01-071-4649 for austenite, 83-0875 for iron nitride $\gamma'$-$Fe_4N$ and 83-0877 for iron nitride ε-$Fe_3N$. The hardness of untreated and treated surfaces samples was measured with a microhardness tester with a Vickers indenter under load of 490 mN ($HV_{0.05}$) for 10 s. Fifteen indentations on each phase were taken. Before performing the test, the samples were electrochemical etched as previously described.

### 2.4 Electrochemical Corrosion Studies

Corrosion behavior of untreated and plasma-nitrided samples was studied using potentiodynamic polarization technique in 3.5 wt.% NaCl solution using a portable potentiostat with a reference electrode of Ag/AgCl (KCl saturated) and graphite as the counter electrode. This instrument has built-in software for data analysis. A specimen area of 0.5027 $cm^2$ was exposed to 70 mL of solution on a flat electrochemical acrylic cell. After stabilizing the open-circuit potential (OCP) for 30 min, the potentiodynamic polarization test was carried out by sweeping at a scan rate of 1 mV/s, from − 300 to 1500 mV for untreated samples and from − 600 to 1500 mV for nitrided ones. The reverse scan initiated at 1500 mV on the cathodic direction. This test was repeated at least three times for each sample condition. All the potentials indicated in this work were compared to Ag/AgCl (KCl saturated). The PSTrace software was used to carry out the tests and to calculate the corrosion current density ($i_{corr}$) and the corrosion potential ($E_{corr}$) values.

**Table 1 Chemical composition (wt.%) of UNS S32205 duplex stainless steel**

| Cr | Ni | Mo | C | Si | Mn | S | P | Fe (balance) |
|---|---|---|---|---|---|---|---|---|
| 22.10% | 5.2% | 2.77% | 0.01% | 0.44% | 0.75% | 0.002% | 0.02% | 63.72% |

The $i_{corr}$ value was used to calculate the corrosion rate (CR) according to ASTM G102-89 standard (Ref 30), considering the dimensionless equivalent weight (EW = 25.874) and density ($\rho = 7.69$ g/cm$^3$) of the UNS S32205. The passivation current density ($i_{pass}$) corresponds to the arithmetic average of current densities throughout the passive region. Finally, the pitting nucleation ($E_p$) and repassivation ($E_R$) potentials were determined from the polarization curves according to the methodology proposed by Esmailzadeh et al. and Shoesmith (Ref 31, 32).

In order to study the evolution of some electrochemical features on nitrided samples, potentiostatic tests were carried out. Therefore, linear polarizations were done until the final potentials 0.7, 0.9, 1.0, 1.05, 1.1, 1.15, 1.2 and 1.35 V, followed by potentiostatic polarization at the chosen potential for 1 h. These tests were performed under the same conditions as the potentiodynamic polarization tests. After the electrochemical studies, the corroded area was analyzed by OM and by scanning electron microscope (SEM), which was operated at 20.000 kV. The SEM was coupled with an energy-dispersive x-ray analysis (EDX) used to identify the element partitioning in the duplex microstructure, according to Weber and Uggowitzer (Ref 33).

## 3. Results and Discussion

Typical cross-sectional micrograph of the plasma-nitrided UNS S32205 is shown in Fig. 1. The measured thickness value of this thin nitrided layer was 4.5 ± 0.5 μm. This layer was uniform, and it was difficult to measure the thickness of the layers formed on top of the individual phases; hence, this is not mentioned. The nitrided layer formed on top of the austenite grains was denoted as $\gamma_N^\gamma$ and that formed on top of the ferrite grains as $\gamma_N^\alpha$, and this nomenclature will be discussed later. Under similar treatment conditions (380 °C, 10 h and a gas mixture consisting of 25% $N_2$ and 75% $H_2$) and using the active screen nitriding technique, Pintaúde et al. (Ref 4) obtained 1.62 ± 0.26 μm nitrided layer thickness on the same DSS. Alphonsa et al. (Ref 6) reported nitrided layers with different thicknesses in each phase, 3.2 and 1.8 μm in ferrite and austenite phase, respectively, when the UNS S32205 was plasma nitrided for 4 h at 400 °C and a gas mixture consisting of 80% $N_2$ and 20% $H_2$.

XRD patterns of untreated and nitrided specimens of UNS S32205 are shown in Fig. 2. The pattern of untreated sample revealed the diffraction peaks corresponding to the crystallographic planes (*hkl*) of ferrite and austenite phases, as listed in Table 2. The pattern for the nitrided specimen showed a significant drop of the ferrite and austenite peaks; in addition, it exhibited two new peaks located at $2\theta = 41.24°$ and $2\theta = 46.08°$. Those peaks are attributed to the nitrogen-expanded austenite phase ($\gamma_N$) (Ref 1-7). These new peaks are broad in nature, and they are positioned at lower angles than the original austenite peaks in the untreated pattern (Fig. 3). This increase in the austenite lattice parameter occurs due to supersaturation of nitrogen solid solution in the face-centered cubic (FCC) structure (Ref 8).

Earlier studies reported the transformation of the ferritic phases into the nitrogen-expanded austenite structure due to the nitrogen gammagenic effect (Ref 4, 6, 9, 10). However, some researches state that low-temperature plasma nitriding promotes the transformation of the ferrite and austenite phases of the untreated DSS, into expanded austenite ($\gamma_N$) and expanded ferrite ($\alpha_N$), respectively (Ref 5, 7). According to Pinedo et al. and Tschiptschin et al., the expanded ferrite phase was evidenced as a broad and low-intensity peak in the XRD spectra, located at $2\theta \approx 44°$ y $2\theta \approx 64°$ (Ref 5, 7). Nowadays, $\alpha_N$ phase is not fully understood and some controversy remains regarding its identification. Discussion around these discrepancies goes beyond the objectives of this work. According to the XRD spectra of the nitrided DSS (Fig. 2 and 3), it is difficult to infer the existence of the $\alpha_N$ phase, but it would be an interesting topic for future research. Therefore, the nomenclature followed in this work is expanded austenite coming from the previous austenite grains ($\gamma_N^\gamma$) and expanded austenite originated from the previous ferrite grains ($\gamma_N^\alpha$), as shown in Fig. 1.

Furthermore, the XRD spectra of nitrided samples revealed peaks attributed to iron nitrides $\gamma'$-$Fe_4N$ and $\varepsilon$-$Fe_3N$, listed in Table 2 and indicated in Fig. 2 and 3. Using this x-ray diffraction analysis conditions, no peaks corresponding to chromium nitrides precipitates were identified. The formation of a nitrided layer composed of nitrogen supersaturated phase without chromium nitrides is one of the most advantageous

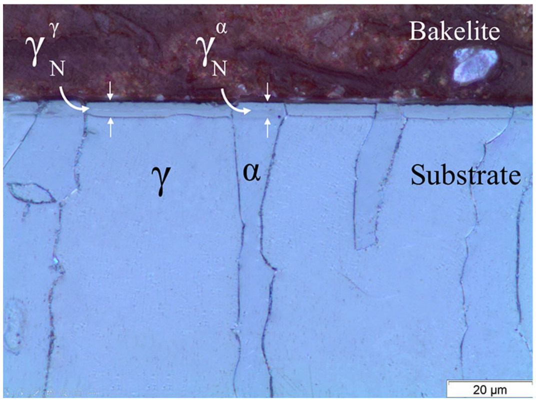

**Fig. 1** Cross-sectional OM images of UNS S32205 plasma nitrided at 380 °C, 10 h and 25% $N_2$-75% $H_2$ atmosphere (etching with 10% oxalic acid)

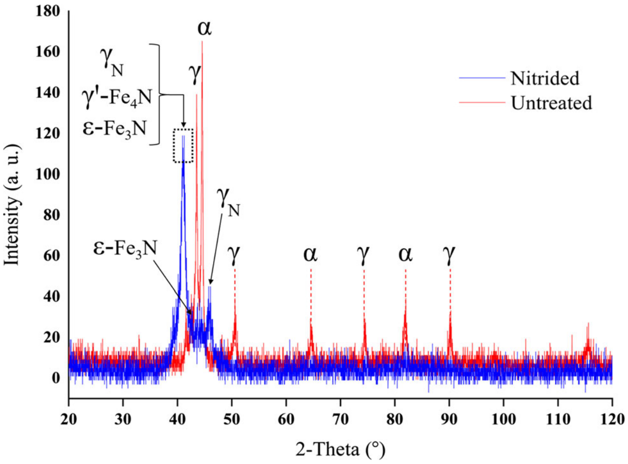

**Fig. 2** XRD patterns of untreated and nitrided UNS S32205

**Table 2 Phase identification, diffraction angles and Miller index**

| Condition | Phase | $2\theta$, ° | (*hkl*) |
|---|---|---|---|
| Untreated | $\gamma$ | 43.52 | (111) |
| | $\alpha$ | 44.54 | (110) |
| | $\gamma$ | 50.58 | (200) |
| | $\alpha$ | 64.76 | (200) |
| | $\gamma$ | 74.5 | (210) |
| | $\alpha$ | 82.42 | (211) |
| | $\gamma$ | 90.3 | (311) |
| | $\alpha$ | 115.6 | (310) |
| Nitrided | $\varepsilon$-$Fe_3N$ | 40.97 | (002) |
| | $\gamma'$-$Fe_4N$ | 41.17 | (111) |
| | $\gamma_N$ | 41.24 | (111) |
| | $\varepsilon$-$Fe_3N$ | 43.42 | (110) |
| | $\gamma_N$ | 46.08 | (200) |

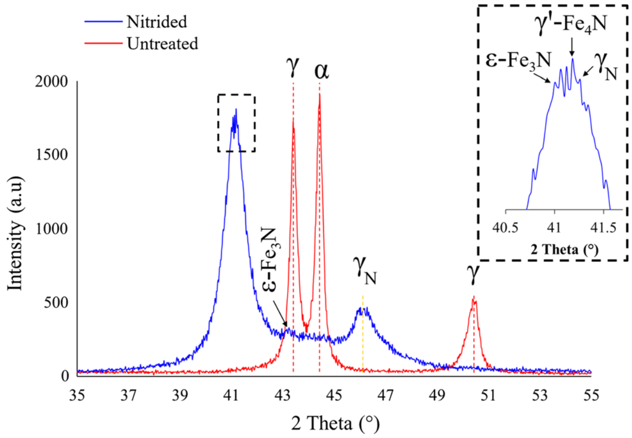

**Fig. 3** Detail of the XRD patterns ranging from 35° to 55° of untreated and nitrided UNS S32205

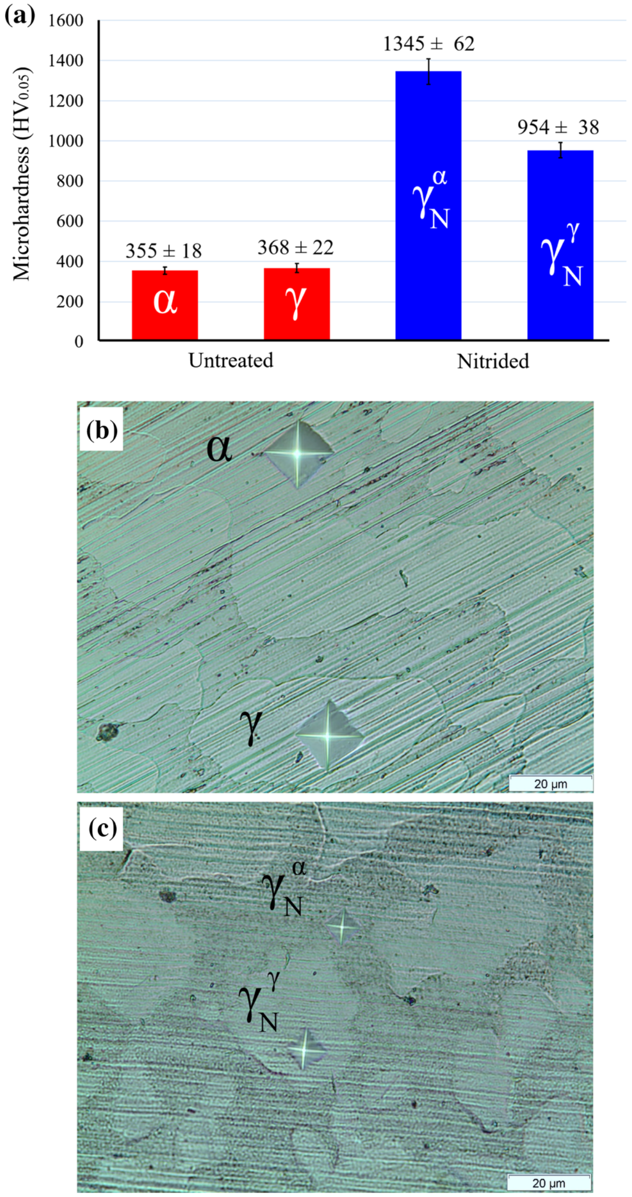

**Fig. 4** Surface microhardness values (a) and Vickers indentations marks in the phases of duplex steel samples (100X): untreated (b) and nitrided (c)

characteristics of low-temperature plasma nitriding of DSS, as it is evidenced in numerous studies (Ref 1-7, 9, 13, 14).

Figure 4 shows the Vickers surface hardness values resulting from the individual phases before and after nitriding. The indentations marks left by the Vickers indenter are shown in Fig. 4(b) and (c). No significant differences were observed in the measured values for the ferritic (355 ± 18 $HV_{0.05}$) and austenitic (368 ± 22 $HV_{0.05}$) phases before treatment. Similar results were obtained on other studies, where the hardness values for both phases were close together in the UNS S32205 steel (Ref 6, 11, 15). Besides, hardness was significantly enhanced due to the formation of the expanded phase. The hardness of the nitrided surface was measured separately on top of the "previous" austenite grains ($\gamma_N^\gamma$) and the "previous" ferrite grains ($\gamma_N^\alpha$), as shown in Fig. 4. In comparison with the untreated ferritic and austenitic phases, the hardness of the nitrided layer increased 3.8 and 2.6 times for expanded $\gamma_N^\alpha$ and expanded $\gamma_N^\gamma$, respectively.

In the literature, many studies performed hardness measurements from random indentations on the plasma-nitrided surface without distinguishing the hardness value of each phase in DSS (Ref 1-3, 10, 13, 14). All of them obtained a hardness increase due to the interstitial solid solution strengthening. For the same material (UNS S32205), two different works reported higher hardness values for the modified ferritic phases at nitriding temperature of 400 °C (Ref 5, 6). Despite this, Pintaúde et al. (Ref 4) found that the modified austenitic phases had higher hardness after nitriding at 380 °C for 10 h. In the referenced works (Ref 4-6), the hardness differences are attributed to the higher nitrogen content in the hard modified phase, which produces high tensions in the crystal lattice with the introduction of these interstitial atoms. Nevertheless, in the present work, the outstanding hardness of expanded $\gamma_N^\alpha$ grains (1345 ± 62 $HV_{0.05}$) compared to the $\gamma_N^\gamma$ grains (954 ± 38 $HV_{0.05}$) could be related to the existence of the iron nitrides ($\gamma'$-$Fe_4N$ and $\varepsilon$-$Fe_3N$) revealed in the XRD spectra (Fig. 2 and 3). According to other studies, iron nitrides mainly precipitated in the modified ferrite grains in the nitrided layer, resulting in higher hardness values in this modified phase (Ref 7, 9).

The surface topography of the samples before and after nitriding treatment was analyzed using the interferometry technique and following the methodology described in section 2.The parameters skewness ($S_{sk}$), maximum peak height ($S_p$) and texture aspect ratio ($S_{tr}$) are the 3D surface texture parameters that best indicate the change in topography with the plasma treatment. All the values are shown in Table 3 and Fig. 5.

As shown in Fig. 5, these parameters have well-differentiated values between initial (untreated) and final (nitrided) surface conditions, with the calculated threshold value being between them. In addition, they were the surface parameters with the highest significance value, thus indicating which surface characteristic changed the most with the nitriding treatment. With these three conditions fulfilled, they effectively represent the parameters that best indicate the topography changes caused by the treatment.

According to Table 3, the negative value of $S_{sk}$ for the untreated surface represents the predominance of surface valleys, while positive values represent the predominance of peaks as a result of the nitriding treatment. On the other hand, $S_{tr}$ values close to 0 indicate surface anisotropy, which agrees with the surface preparation prior to treatment, as it can be observed in the directionality of the ground marks in Fig. 6(a), whereas $S_{tr}$ values close to 1 represent a more isotropic surface as shown in Fig. 6(b), as a result of the random bombardment of species during the plasma sputtering and nitriding processes (Ref 6, 29). Finally, $S_p$ parameter agrees with the results of the skewness parameter, evidencing that nitriding treatment changed the surface to a more isotropic topography with predominance of peaks.

The polarization curves shown in Fig. 7 correspond to the potentiodynamic sweeps of UNS S32205 untreated and nitrided. Corrosion current density, corrosion potential, passivation current density, pitting nucleation potential, repassivation potential and corrosion rate values of untreated and plasma-nitrided UNS S32205 are summarized in Table 4. These results are the arithmetic mean of at least three specimens in order to check the replicability; the scatter in the data is also reported.

After the nitriding treatment, the corrosion potential ($E_{corr}$) decreased, while the corrosion current density ($i_{corr}$) increased, both with respect to the untreated specimen. These results represent a loss of nobility in the general corrosion in the nitrided steel. The average passivation current density ($i_{pass}$) is two orders of magnitude higher, indicating that the passive layer of nitrided surface was less protective. However, according to the literature, current densities of the order of nA/cm$^2$ to tens of mA/cm$^2$ are considered passivation densities (Ref 32). Previous works on nitrided DSS (UNS S31803 and UNS S32205) obtained nobler or equal corrosion potentials for nitrided steel compared to the untreated material (Ref 2, 4, 6, 14). These studies reported passivation current densities of the untreated material in the order of magnitude of $10^0$ to $10^1$ μA/cm$^2$, while the average current density of nitrided samples can be in the same order of magnitude and larger up to two orders.

The polarization curves for the nitrided specimens (Fig. 7) also show the displacement of the pitting nucleation potential ($E_P$) and repassivation potential ($E_R$) to larger potentials with the consequent reduction in the hysteresis loop. The above observations manifest the better localized corrosion resistance of the nitrided UNS S32205. It is important to note that none of

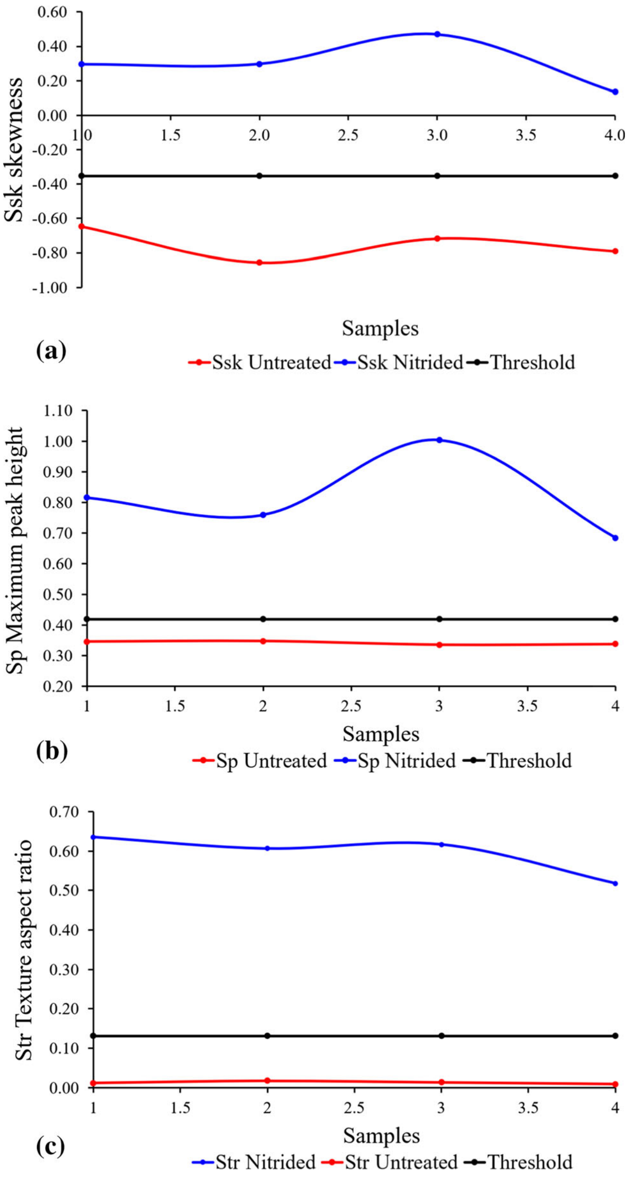

**Fig. 5** Graphical representation of $S_{sk}$ (a), $S_p$ (b) and $S_{tr}$ (c) parameters and their threshold values before and after nitriding

**Table 3 Values of $S_{sk}$, $S_p$ and $S_{tr}$ surface texture parameters and their significance and threshold calculated values**

| Parameter | Significance | Threshold | Untreated | Nitrided |
|---|---|---|---|---|
| $S_{sk}$ | 6.64 | − 0.35 | − 0.75 ± 0.09 | 0.3 ± 0.14 |
| $S_p$, μm | 1.31 | 0.42 | 0.341 ± 0.006 | 0.82 ± 0.14 |
| $S_{tr}$ | 2.29 | 0.13 | 0.013 ± 0.004 | 0.59 ± 0.05 |

these corroded samples (untreated and nitrided) presented crevice corrosion. Instead, general corrosion and some pits were observed in the corroded surface of both samples.

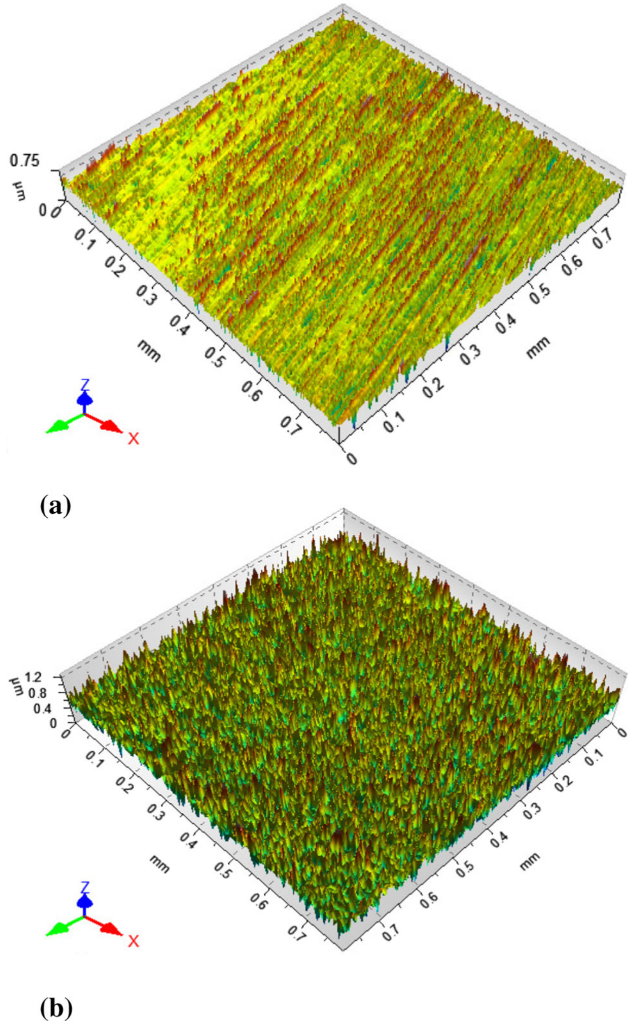

**Fig. 6** Topographic 3D profile of UNS S32205: (a) untreated and (b) nitrided

The positive effect of nitrogen on improving the pitting corrosion resistance was already confirmed by Baba et al. (Ref 12) and other researches in DSS plasma nitrided (Ref 1-4, 6). Besides this effect, the influence of surface roughness in the localized corrosion cannot be neglected. According to Tang et al. (Ref 26), a rougher surface increases the possibility of stable pitting grow. In the present investigation, untreated surfaces showed predominance of valleys structures demonstrated by the parameters $S_{sk} = -0.75 \pm 0.09$ and $S_p$ (μm) = $0.341 \pm 0.006$. The valleys structures could promote cavities more occluded and with the ability to maintain the internal electrochemical pit environment (Ref 26). This could also contribute to the lower pitting corrosion resistance of the rougher surface, i.e., the untreated surface, which exhibited higher hysteresis loop and lower $E_P$ and $E_R$ potentials indeed.

The potentiodynamic curves of the nitrided samples (Fig. 7) exhibit a hillside at the end of the passivation region and just before the transpassive region. This feature was already evidenced on other studies of plasma-nitrided stainless steels as those developed by Chiu et al., Pereira et al., Alphonsa, Raja and Mukherjee, Li, Dou and Dong and Lee, in DSS, the work of Spies et al. in austenitic steel and Pires et al. in martensitic steel (Ref 2, 3, 6, 13-17). In none of these studies, a discussion regarding this behavior is presented.

**Table 4 Summary of $i_{corr}$, $E_{corr}$, $i_{pass}$, $E_p$, $E_R$ and corrosion rate (CR) of untreated and plasma-nitrided UNS S32205 steel**

| | Duplex stainless steel UNS S32205 | |
|---|---|---|
| | **Untreated** | **Nitrided** |
| $i_{corr}$, μA/cm$^2$ | 0.22 ± 0.12 | 0.98 ± 0.63 |
| $E_{corr}$, V | − 0.15 ± 0.04 | − 0.33 ± 0.08 |
| $i_{pass}$, μA/cm$^2$ | 4.7 ± 1.3 | 268 ± 40 |
| $E_p$, V | 1.17 ± 0.05 | 1.285 ± 0.005 |
| $E_R$, V | 1.10 ± 0.16 | 1.21 ± 0.01 |
| CR, mm/year | 0.002 ± 0.001 | 0.011 ± 0.007 |

Standard deviation in data is shown

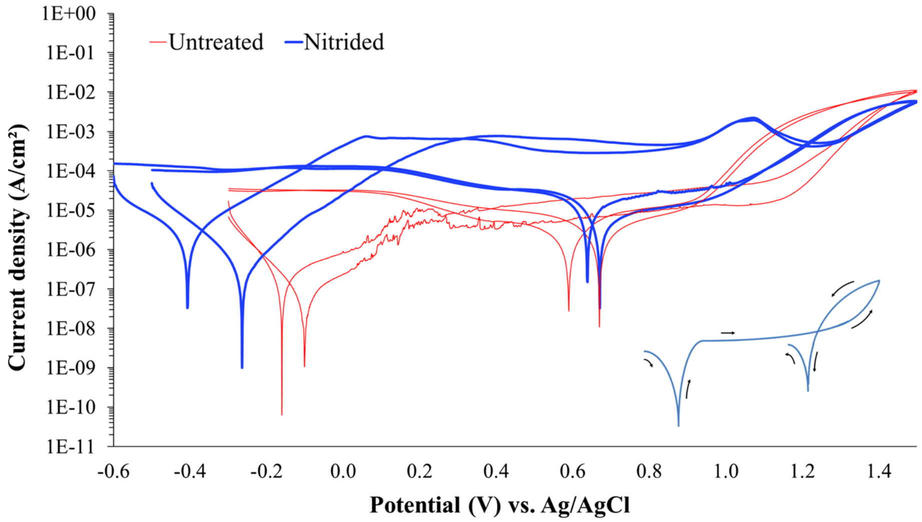

**Fig. 7** Potentiodynamic polarization curves of untreated and nitrided UNS S32205 (Scan rate 1 mV/s, 3.5 wt.% NaCl)

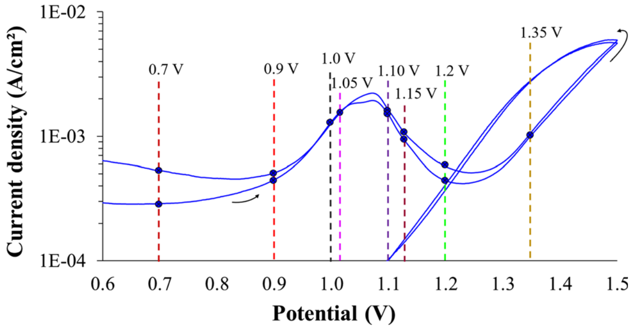

**Fig. 8** Detail of the potentiodynamic polarization curves of nitrided UNS S32205. The chosen potentials for potentiostatic tests are identified by dotted lines that cross over the polarization curves at the potentials: 0.7, 0.9, 1.0, 1.05, 1.1, 1.15, 1.2 and 1.35 V

Figure 8 shows a zoomed view of the polarization curves of nitrided samples between 0.7 and 1.5 V. The hillside is evidenced between the potentials 0.9 and 1.2 V, prior to the hysteresis loop. The hillside is characterized by a continuous increase followed by a decrease in the current density. In order to study the evolution of this phenomena, different potentials (identified in Fig. 8) were chosen for potentiostatic analysis. The passivation (0.7 V) and transpassivation (1.35 V) potentials were also chosen for comparative purposes.

During the potentiostatic tests, the variation of the current as a function of time was recorded. These curves are presented in Fig. 9(a).

The current–time curves (Fig. 9a) of the tests developed in the potential range from 0.7 to 1.2 V showed a similar trend: They started at current values around 2000 µA, in the first 300 s they suddenly decreased, and then they maintained almost constant current values until the end of the test. The curve of the test performed at 1.35 V behaved differently from the others, stabilizing at higher current values. According to the cyclic polarization curves (Fig. 7), this potential is located in the transpassivation region, where the current increase is usually attributed to the passive layer dissolution and localized corrosion processes. In addition, during this test at 1.35 V, many bubbles were formed on the corroded surface, which is related to the decomposition of water, a reaction that also contributed to the current increase.

Figure 9(b) shows a zoomed view of the current–time curves performed between potentials 0.7 and 1.15 V. In those curves, it could be observed current transients or fluctuations all along the time lapse, being greater at the potentials 1.05 and 1.15 V. At the potential 1.05 V, these signals had well-defined periodic behavior from 1200 s until the end of the test. These fluctuations had a variable amplitude ranging from 0.05 to 3.0 µA and a period between 3 and 5 s. This potential corresponds to the top of the hillside (Fig. 8). In comparison, the current fluctuations of the tests developed at the 1.15 V potential were variable from 200 s until the end of the test, presenting wide dispersion of both amplitude and period values.

Stainless steels in chloride-containing solutions have been evidenced electrochemical noise, transient signals or well-known fluctuations in current when they were subjected to open-circuit potential condition, potentiodynamic polarization, anodic galvanostatic polarization and potentiostatic polarization (Ref 18, 22-24). These signals reflect the initiation, growth and repassivation processes of precursor pits, which are called metastable pits. According to Laycock, Moayed and Newman, the manifestation of these transient signals, even at temperature conditions lower than the critical pitting temperature (CPT) or also at potentials lower than the pitting potential, is an indication of these metastable phenomena (Ref 22). These current fluctuations can have ranges from tens of pA to tens of µA (above the average current) and a short duration of a few seconds, as reported on different austenitic stainless steels and DSS (Ref 22-27). Consequently, the fluctuations of the current–time curves of the potentiostatic tests (Fig. 9b) are attributed to metastable pitting in the nitrided UNS S32205.

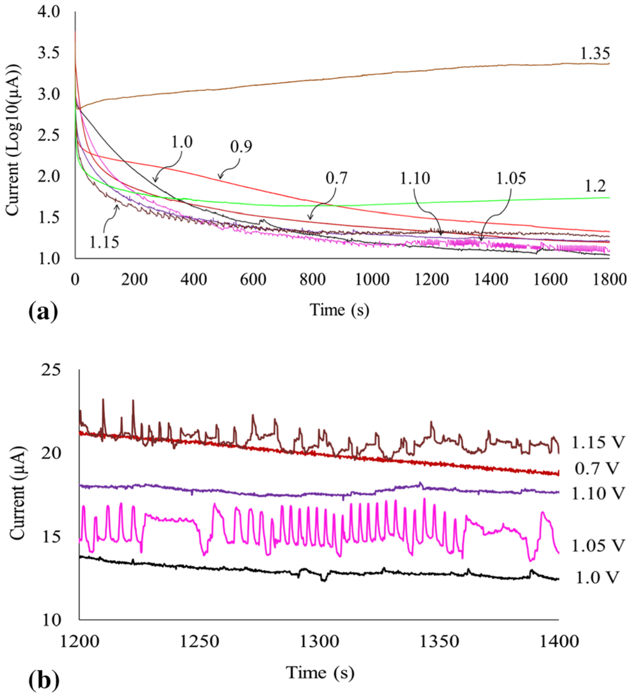

**Fig. 9** Results of potentiostatic tests set at the chosen potentials in the passive-to-transpassive transition of nitrided UNS S32205. (a) Current versus time curves of all the potentiostatic conditions; (b) detail between 1200 and 1400 s of potentiostatic tests hold at 0.7, 1.0, 1.05, 1.10 and 1.15 V

With the purpose of studying the phenomenology occurred during the potentiostatic tests, micrographs of the corroded surfaces after tests were analyzed in order to confirm the formation of metastable pits and to identify if other types of corrosion occurred. In this type of mounting, crevice corrosion can occur in the contact regions or boundaries between the sample and the corrosion cell. These boundaries were analyzed, whose micrographs are presented in Fig. 10.

The micrographs in Fig. 10 are divided by a dotted line drawn in the sample/cell contact regions. Consequently, the corroded surface that was exposed to the electrolytic solution is in the right side of each micrograph. The sample surface that was not in contact with the solution is in the left side. In the micrographs shown in Fig. 10(a)-(e) (potentials between 0.7 and 1.2 V), it is possible to observe the non-formation of crevice corrosion; therefore, the formation of the hillside was not a consequence of this type of localized corrosion. Otherwise in Fig. 10(f), crevice formation in the boundary region is evidenced in addition to further general surface degradation. The corrosion attack seems deeper in one of the

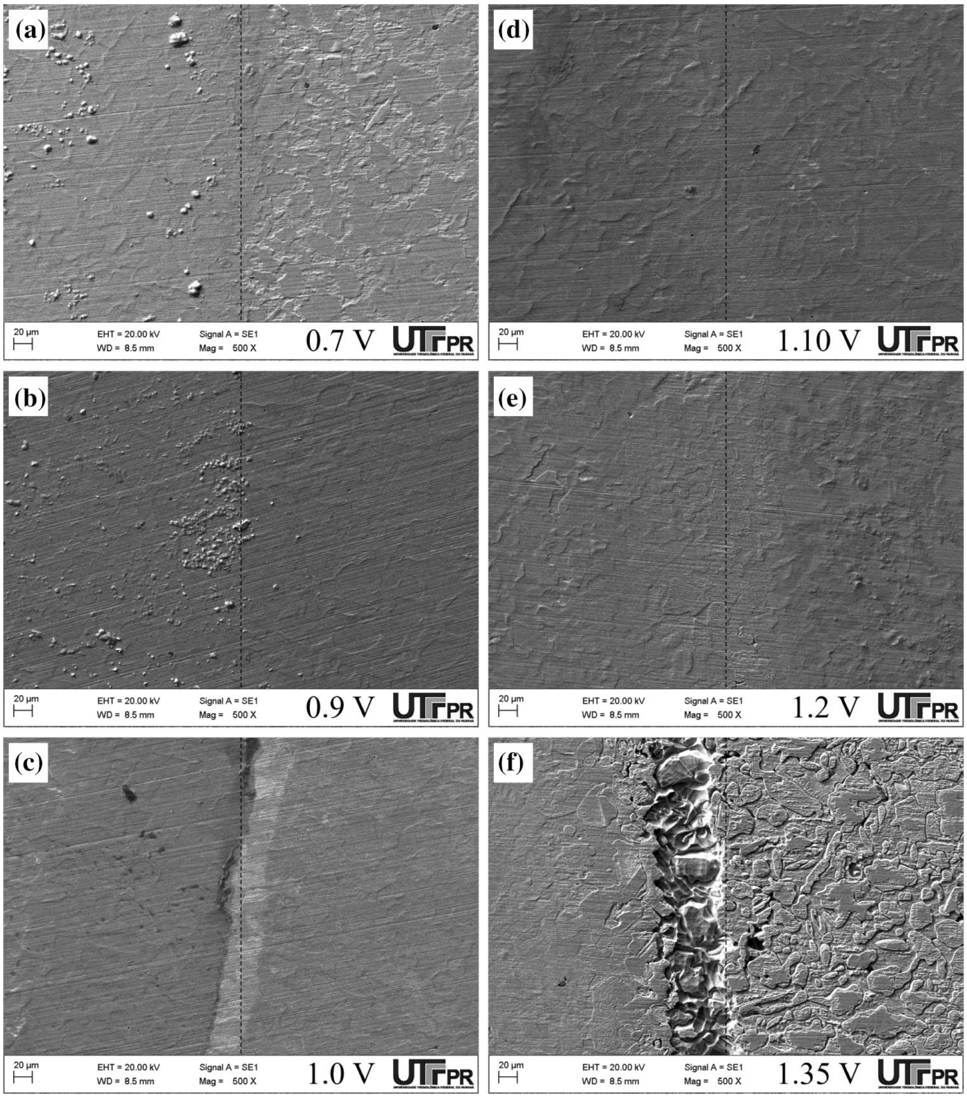

**Fig. 10** SEM micrographs of nitrided samples (500X) after the potentiostatic tests hold at: (a) 0.7 V; (b) 0.9 V; (c) 1.0 V; (d) 1.10 V; (e) 1.2 V; and (f) 1.35 V. Surfaces comparison: right side corroded, left side not exposed to 3.5 wt.% NaCl solution

phases. Crevice corrosion and high surface degradation observed in the sample polarized at the transpassive potential (1.35 V, Fig. 10f) certainly were part of the sources that contributed to the higher current values (Fig. 9a).

Once it was verified that there was no crevice corrosion in the potential range where the hillside was formed, the corroded surfaces were analyzed with the aim of detecting the formation of pits. Some micrographs of these surfaces are shown in Fig. 11, which demonstrated the presence of pits in all potentiostatic tests. It was identified by EDX in which expanded phase the pits nucleated preferentially, because the substitutional elements remain in the regions previously occupied by austenite and ferrite grains (Ref 4, 6).

Low-temperature plasma nitriding studies on DSS report a non-uniform distribution of nitrogen in the nitrided layer, with differences between phases (Ref 2, 4, 6, 9). According to the Pitting Resistant Equivalent Number (PREN), the pitting corrosion resistance depends mainly on the chromium, molybdenum and nitrogen elements (Ref 19, 33). Hence, the unequal distribution of the elements in the phases could cause a difference in localized corrosion resistance between them. In fact, most of the pits nucleated in the expanded $\gamma_N^\alpha$ phase and some pits nucleated in the phase boundaries between the expanded $\gamma_N^\gamma$ and expanded $\gamma_N^\alpha$ grains. Finally, few pits were found within the expanded $\gamma_N^\gamma$ grains. To confirm the element partitioning in the nitrided UNS S32205, further research needs to be done in order to study the accurate chemical composition of the expanded phases from chemical analysis techniques, such as WDS and XPS.

In the micrographs of the tests conducted between the potentials 0.7 to 1.2 V (Fig. 11a-f), pits with dimensions not exceeding 5 µm in diameter were observed. According to some studies, the size of the metastable pits did not exceed 10 µm (Ref 18, 23, 26, 27). Therefore, the pits nucleated during potentiostatic tests can be considered metastable pits, which verifies the transient behavior observed in current curves as a function of time (Fig. 9b). When these metastable pits were subjected to potentials in the transpassivation region (> 1.2 V), they became stable and severe pits as those observed in the micrographs of the potential tests at 1.35 V (Fig. 11g and h). In this test condition, the size of the pits was considerably larger than the pits formed at the other lesser

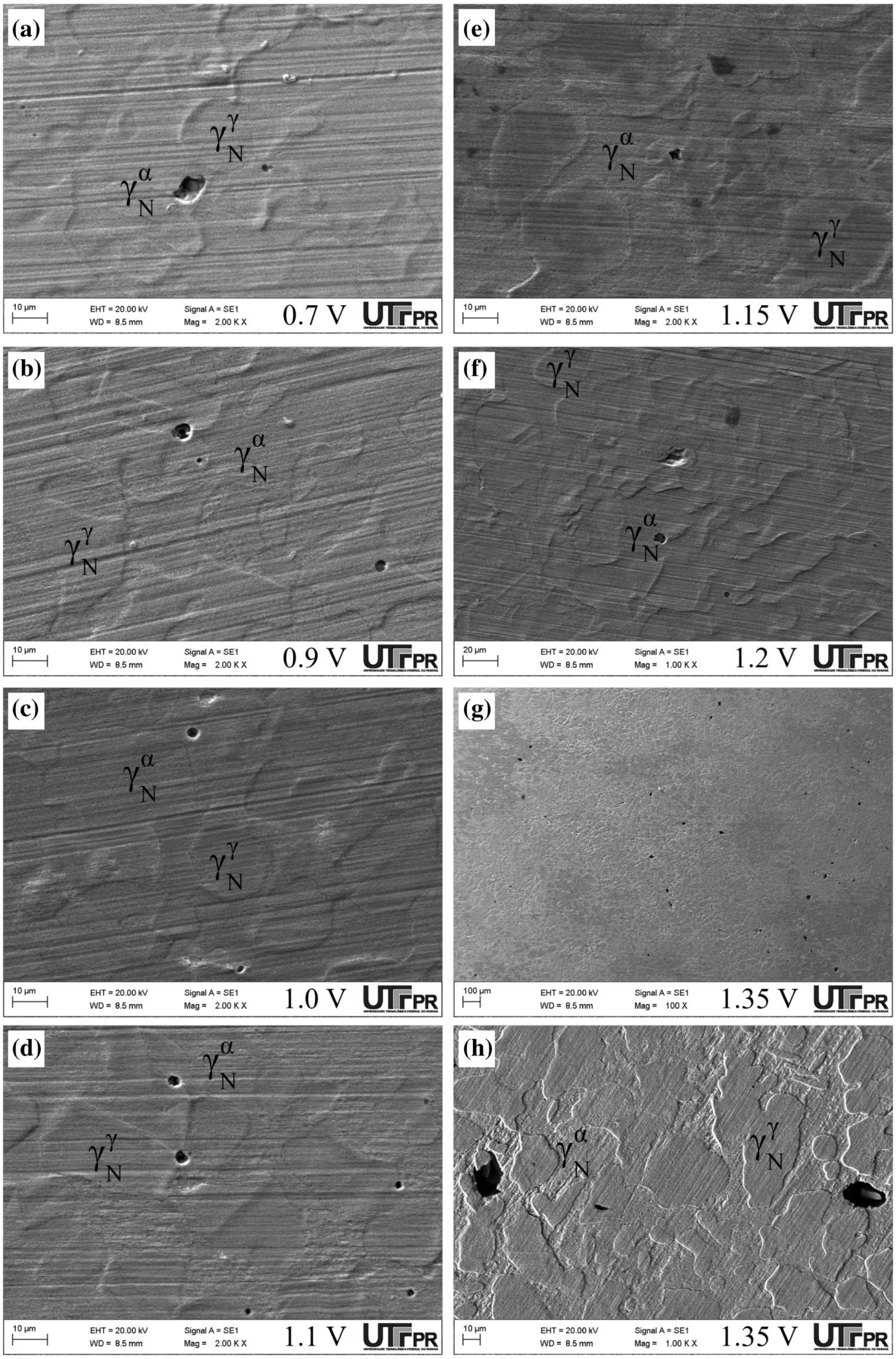

**Fig. 11** SEM micrographs of nitrided samples after potentiostatic tests hold at: (a) 0.7 V; (b) 0.9 V; (c) 1.0 V; (d) 1.10 V; (e) 1.15 V; (f) 1.2 V; and (g) 1.35; (h) Detail of surface after potentiostatic test at 1.35 V

potentials, having diameters up to 20 µm (Fig. 11h). The fact that these metastable pits were formed and immediately repassivated, as evidenced by the transient signals, also agrees that the material was polarized in potentials smaller than the repassivation potential ($E_R$ = 1.21 ± 0.01 V, Table 2) and theoretically the material has the ability to repassivate the localized corrosion (Ref 10).

Besides the preferential nucleation of the metastable pits in the expanded $\gamma_N^\alpha$ regions, it was also evidenced the greater susceptibility of corrosion attack in this phase. Figure 12(a) shows how some regions were preferentially attacked (dark regions: $\gamma_N^\alpha$), while in the other expanded phase (light regions: $\gamma_N^\gamma$) the corrosion was less evident. The precipitates observed in Fig. 12(b) were analyzed by EDX. This technique revealed that

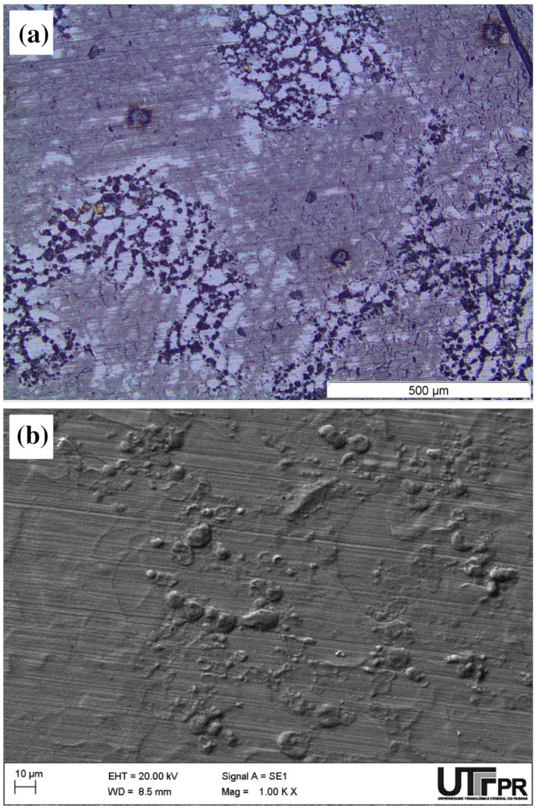

**Fig. 12** Micrographs of corroded surfaces of nitrided specimens after potentiostatic tests (1.2 V): (a) OM and (b) SEM

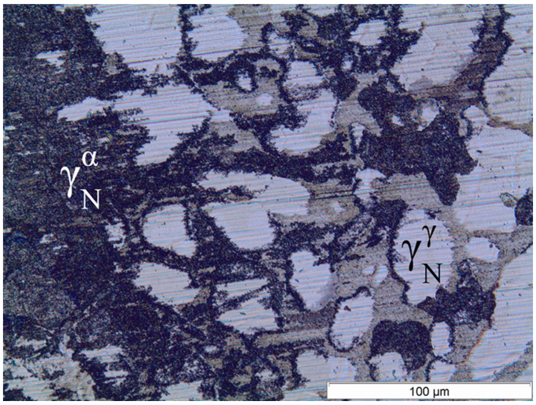

**Fig. 13** OM micrograph of corroded surface of nitrided specimens after potentiostatic tests (1.35 V)

they were probably corrosion products such as oxides and salts, due to the oxygen (27.16% mass) and chlorine contents measured (1.12% mass).

Finally, it is shown in Fig. 13 the corroded surface after the potentiostatic test at 1.35 V. In this figure is evidenced the preferential corrosion in the (dark) expanded $\gamma_N^\alpha$ phase and in some grain boundaries between expanded phases. The intergranular corrosion could be caused by the formation of the galvanic cell as a consequence of the differences in corrosion resistance in the duplex biphasic morphology (Ref 19, 21, 26, 33).

Summarizing, the formation of the hillside on the passive-to-transpassive region in the nitrided UNS S32205 is a manifestation of the metastable pit nucleation. This type of pits evolves into stable pits at potentials higher than the repassivation potential, when the material is already in the transpassivation region. Additionally, it was evidenced that the expanded $\gamma_N^\alpha$ regions and the grain boundaries are more susceptible to corrosion attack and pitting corrosion, in comparison with the expanded $\gamma_N^\gamma$ phase.

## 4. Conclusions

Plasma nitriding was conducted on duplex stainless steel UNS S32205 at a temperature of 380 °C for 10 h. Based on the experimental results, the following conclusions can be drawn:

- The plasma nitriding treatment of the UNS S32205 steel formed a layer thickness of 4.5 ± 0.5 µm composed of nitrogen-expanded austenite and iron nitrides ($\gamma'$-$Fe_4N$ and $\varepsilon$-$Fe_3N$) without chromium nitrides precipitates.
- The nitrided surface exhibited higher hardness values being 2.6 and 3.8 times in the expanded phases formed on top of austenite and ferrite grains, respectively, when compared with the untreated surfaces.
- The nitriding treatment produced a more isotropic topography with a predominance of peaks, confirmed by the values of the 3D surface texture parameters $S_{sk}$, $S_p$ and $S_{tr}$.
- The cyclic polarization tests revealed an improvement in localized corrosion resistance of nitrided steel, showing higher values of pitting ($E_p$) and repassivation ($E_R$) potentials and smaller hysteresis loop compared to the untreated condition.
- The hillside exhibited at the end of the passivation region of the nitrided specimens was a consequence of the nucleation of metastable pits between the potentials 0.9 V and 1.2 V (versus Ag-AgCl).
- Metastable pits preferentially nucleated in the expanded $\gamma_N^\alpha$ phases, and they were identified by transient signals during potentiostatic tests, in addition to their diameter that does not exceed 5 µm.
- The expanded $\gamma_N^\alpha$ phases and the grain boundaries of the nitrided UNS S32205 showed the highest corrosion susceptibility during the potentiostatic tests carried out at 1.2 and 1.35 V.

## Acknowledgments

The authors thank CNPq and CAPES Brazilian Funding Agencies for the scholarships awarded to Y. Núñez and O. Palma. The authors acknowledge the Multi-User Center for Materials Characterization (CMCM) of the UTFPR for SEM analysis. The authors also thank Fundación Universitaria *Los Libertadores* and Federal University of Technology - *Paraná* (UTFPR) for the financial support of this research.

## Open Access

## References

1. K. Nagatsuka, A. Nishimoto, and K. Akamatsu, Surface Hardening of Duplex Stainless Steel by Low Temperature Active Screen, *Surf. Coat. Technol.*, 2010, **205**(1), p 295–299
2. L.H. Chiu, Y.Y. Su, F.S. Chen, and H. Chang, Microstructure and Properties of Active Screen Plasma, *Mater. Manuf. Process.*, 2010, **25**(5), p 316–323
3. J.O. Pereira, R. Oliveira, E. Hónorio, J.A. Moreto, R. Marinho, M. Dorigão, and L. Sgarbi, Wear and Corrosion Study of Plasma Nitriding F53 Super Duplex Stainless Steel, *Mater. Res.*, 2016, **19**(6), p 1241–1252
4. G. Pintaúde, A. Rovani, J.C. Klein das Neves, L.E. Lagoeiro, X. Li, and H. Dong, Wear and Corrosion Resistances of Active Screen Plasma-Nitrided Duplex Stainless Steels, *J. Mater. Eng. Perform.*, 2019, **28**(6), p 3673–3682
5. C.E. Pinedo, L.B. Varela, and A.P. Tschiptschin, Low-Temperature Plasma Nitriding of AISI, F51 Duplex Stainless Steel, *Surf. Coat. Technol.*, 2013, **232**, p 839–843
6. J. Alphonsa, V.S. Raja, and S. Mukherjee, Study of Plasma Nitriding and Nitrocarburizing for Higher Corrosion Resistance and Hardness of 2205 Duplex Stainless Steel, *Corros. Sci.*, 2015, **100**, p 121–132
7. A.P. Tschiptschin, L.B. Varela, C.E. Pinedo, X.Y. Li, and H. Dong, Development and Microstructure Characterization of Single and Duplex Nitriding of UNS S31803 Duplex Stainless Steel, *Surf. Coat. Technol.*, 2017, **327**, p 83–92
8. B.K. Brink, K. Stahl, T.L. Christiansen, and J. Oddershede, On the Elusive Crystal Structure of Expanded Austenite, *Scr. Mater.*, 2017, **131**(1), p 59–62
9. W. de Oliveira, B. Kurelo, D.G. Ditzel, F. Serbena, C. Foerster, and G. de Souza, On the S-Phase Formation and the Balanced Plasma Nitriding of Austenitic-Ferritic Super Duplex Stainless Steel, *Appl. Surf. Sci.*, 2018, **434**(15), p 1161–1174
10. J. Yan, T. Gu, S. Qiu, J. Wang, J. Xiong, and H. Fan, Phase Transformations During the Low-Temperature Nitriding of AISI, Duplex Stainless Steel, *Metall. Mater. Trans. B*, 2015, **43**(3), p 1461–1470
11. J.E. May, C.A. Caldas de Souza, P.A.P. Nascente, P. Soares, C.M. Lepienski, and S.E. Kuri, Effect of Thermal Aging Conditions on the Corrosion Properties and Hardness of a Duplex Stainless Steel, *Mater. Res.*, 2010, **13**(4), p 431–436
12. H. Baba, T. Kodama, and Y. Katada, Role of Nitrogen on the Corrosion Behavior of Austenitic Stainless Steels, *Corros. Sci.*, 2002, **44**(10), p 2393–2407
13. X. Li, W. Dou, and H. Dong, Combating the Tribo-Corrosion of LDX2404 Lean Duplex Stainless Steel by Low Temperature Plasma Nitriding, *Lubricants*, 2018, **6**(93), p 1–12
14. I. Lee, Effect of CH4 Content on the Characteristics of Surface Layers of Low Temperature Plasma Nitrided 2205 Duplex Stainless Steel, *Mater. Sci. Forum*, 2016, **879**, p 1074–1079
15. O. Palma, Y. Núñez, J. Ribeiro, P. Borges, Comportamento tribológico do aço inoxidável duplex UNS S32205 submetido a nitretação a plasma em baixas temperaturas (Tribological properties of low temperature plasma nitrided duplex stainless steel UNS S32205), Congresso Brasileiro de Engenharia de Fabricação, 2019, pp. 1–6 (in Portuguese)
16. H. Spies, C. Eckstein, H. Biermann, and A. Franke, Corrosion Behaviour of Stainless Steels After Low Temperature Thermochemical Treatment, *Mater. Sci. Eng. Technol.*, 2010, **41**(3), p 133–141
17. F. Pires, C. Picone, G. Totten, and L. Casteletti, Corrosion Behavior of Plasma Nitrided and Nitrocarburised Supermartensitic Stainless Steel, *Mater. Res.*, 2018, **21**(3), p 1–8
18. Z. Szklarska-Smialowska, *Pitting and Crevice Corrosion*, Houston, NACE International, 2005, p 45–162
19. A. Perren, T. Suter, P. Uggowitzer, L. Weber, R. Magdowski, H. Böhni, and M.O. Speidel, Corrosion Resistance of Super Duplex Stainless Steels in Chloride Ion Containing Environments: Investigations by Means of a New Microelectrochemical Method I. Precipitation-Free States, *Corros. Sci.*, 2011, **43**, p 707–726
20. B. Deng, Y. Jiang, J. Gong, C. Zhong, J. Gao, and J. Li, Critical Pitting and Repassivation Temperatures for Duplex Stainless Steel in Chloride Solutions, *Electrochim. Acta*, 2008, **53**, p 5220–5225
21. E. de Souza, S. Rossitti, C. Fortulan, and J. Domingos, Influence of Ferrite Phase Content on the Electrochemical Properties of Duplex Stainless Steels, *Mater. Res.*, 2017, **20**(1), p 21–29
22. N. Laycock, M. Moayed, and C. Newman, Metastable Pitting and the Critical Pitting Temperature, *J. Electrochem. Soc.*, 1998, **145**(8), p 2622–2628
23. P. Pistorius and G. Burstein, Metastable Pitting Corrosion of Stainless Steel and the Transition to Stability, *Philos. Trans. R. Soc.*, 1992, **341**(1662), p 531–559
24. H. Böhni, Localized Corrosion—Mechanisms and Methods, *Mater. Sci. Forum*, 1992, **111–112**, p 401–414
25. M.H. Moayed and R.C. Newman, Evolution of Current Transients and Morphology of Metastable and Stable Pitting on Stainless Steel Near the Critical Pitting Temperature, *Corros. Sci.*, 2006, **48**, p 1004–1018
26. Y. Tang, N. Dai, J. Wu, Y. Jiang, and J. Li, Effect of Surface Roughness on Pitting Corrosion of 2205 Duplex Stainless Steel Investigated by Electrochemical Noise Measurements, *Materials*, 2019, **12**(738), p 1–20
27. L.F. Garfias-Mesias and J.M. Sykes, Metastable Pitting in 14 Cr Duplex Stainless Steel, *Corros. Sci.*, 1999, **41**(5), p 959–987
28. F. Helmli, K. Potsch, and C. Repitsch, Choosing the appropriate parameter, *Characterisation of Areal Surface Texture*, R. Leach, Ed., Springer, Berlin, 2013, p 155–166
29. D. Marton and J. Fine, On the Development of Increasing Surface Roughness During Ion Sputtering, *Thin Solid Films*, 1987, **151**(3), p 433–439
30. Standard Practice for Calculation of Corrosion Rates and Related Information from Electrochemical Measurements, ASTM G102 – 89 (American Society for Testing Materials International, 2015), pp. 1–7
31. S. Esmailzadeh, M. Aliofkhazraei, and H. Sarlak, Interpretation of Cyclic Potentiodynamic Polarization Test Results for Study of Corrosion Behavior of Metals: A Review, *Prot. Metals Phys. Chem. Surf.*, 2018, **54**(1), p 976–989
32. D.W. Shoesmith, Kinetics of aqueous corrosion, *Corrosion: Fundamentals, Testing, and Protection*, Vol 13A, S.D. Cramer and B.S. Covino, Ed., ASM Handbook, ASM International, Novelty, 2003, p 42–51
33. L. Weber and P. Uggowitzer, Partitioning of Chromium and Molybdenum in Super Duplex Stainless Steels with Respect to Nitrogen and Nickel Content, *Mater. Sci. Eng. A*, 1998, **242**(1–2), p 222–229

# The effect of plasma nitriding on the synergism between wear and corrosion of SAF 2205 duplex stainless steel

*Yamid Núñez, Marcio Mafra, Rigoberto E. Morales, Paulo César Borges and Giuseppe Pintaude*
Department of Mechanics, Universidade Tecnológica Federal do Paraná, Curitiba, Brazil

**Abstract**

**Purpose** – This study aims to assess the performance of SAF 2205 duplex stainless steel against pure wear, tribo-corrosion, corrosion and the synergism between wear and corrosion. The effect of plasma nitriding conducted at low temperature (380°C) on SAF 2205 steel was analyzed.

**Design/methodology/approach** – Three systems were used for assessing the synergism between wear and corrosion: tribo-corrosion – wear tests conducted using the micro-scale abrasion test, performed under a slurry of alumina particles containing 3.5% NaCl; pure wear – tests conducted using the previous system but isolated in a glovebox with a 99% N2 atmosphere; and cyclic polarization under 3.5% NaCl solution. A hard nitrided layer of 3 $\mu$m thickness was characterized using X-ray diffraction, presenting expanded austenite.

**Findings** – The wear mode after micro-scale abrasion tests changed in the absence of an oxygen atmosphere. During pure wear, a mixed mode was identified (rolling + grooving), with the grooving mode more intense for the untreated steel. For tribo-corrosion tests, only rolling wear was identified. For all cases, the nitrided samples presented less wear. The corrosion results indicated a higher repassivation potential for the nitrided condition.

**Practical implications** – The synergism was more positive for the nitrided sample than for the untreated one, which can be considered for surface treatments of duplex stainless steels in practical applications.

**Originality/value** – A detailed description of wear mechanisms showed a significant change in the presence of oxygen atmosphere, a new approach for isolating pure wear.

**Keywords** Duplex stainless steel, Plasma nitriding, Micro-abrasion, Corrosion, Tribo-corrosion, Synergistic effect

**Paper type** Research paper

## 1. Introduction

Duplex stainless steel has been successfully used in the oil and gas industry (Craidy *et al.*, 2015). Among its applications are joints, valves and pipes subject to aggressive medium. Such components can suffer degradation from the interaction with the saline environment and at the same time with the sand present in the seawater.

The improvement of abrasion resistance can be achieved by using surface treatments, such that the hardness of duplex stainless steel is limited to restrictions imposed by the possibility of hydrogen embrittlement (Lai *et al.*, 2013). In this way, low-temperature plasma nitriding is an alternative for keeping the corrosion resistance and improving the surface hardness (Cardoso *et al.*, 2016) and probably mitigating the hydrogen embrittlement (Asgari *et al.*, 2013).

The abrasion behavior of duplex stainless steels has been studied separately from their corrosion resistances (Marques *et al.*, 2011; Pereira Neto *et al.*, 2016; Pintaude *et al.*, 2019).

Marques *et al.* (2011) studied the micro-abrasion and corrosion behaviors of super duplex UNS S32750 steel. They observed that the precipitation of a hard phase after heat treatment increased the wear resistance by 50 per cent. The harder sample, containing sigma phase, presented less wear, associated with shallower grooves and fewer indentations on the hard phase. However, this condition resulted in a significant drop in the critical pitting temperature and fracture toughness. On the other hand, in the presence of $\alpha$' phase (nanometric Cr-rich precipitates) the increase in wear was not accompanied either with less corrosion or even toughness reductions.

The effect of plasma nitriding on the wear and corrosion behaviors was described by Pereira Neto *et al.* (2016) separately. In their study, the crater wear was caused by direct contact between the ball and the worn surface, without a slurry. Within the range of nitriding temperatures (350-570°C), they

---

The current issue and full text archive of this journal is available on Emerald Insight at: **https://www.emerald.com/insight/0036-8792.htm**

Industrial Lubrication and Tribology
72/9 (2020) 1117–1122
© Emerald Publishing Limited [ISSN 0036-8792]
[DOI 10.1108/ILT-08-2019-0302]

The authors would like to thank funding given by National Council for Scientific and Technological Development (CNPq) (Process 443896/2014-3) and Fundação Araucãria (Process FA CP08/2017) for their financial support. The authors also thank the Multi-User Center for Materials Characterization (CMCM, Curitiba, Brazil) scanning electron microscopy analysis and Sandvik do Brasil S/A (São Paulo, Brazil) for supplying duplex stainless steel bars. One of authors, G. Pintaude, thanks to CNPq by the financial support through Process 308416/2017-1.

Received 2 August 2019
Revised 15 November 2019
Accepted 9 January 2020

found that 400°C can be allied with wear and corrosion resistances.

Pintaude *et al.* (2019) studied the effect of low-temperature plasma nitriding (380°C) on the scratch resistance and corrosion of two grades of duplex stainless steel (SAF 2205 and SAF 2507). The higher support given by the hardness of SAF 2507 steel was determinant for achieving a larger critical load in the scratch test for a thin layer composed by expanded austenite, formed due to plasma nitriding. In terms of corrosion, the pitting potential was practically unchanged after nitriding.

There are many adaptations to conduct micro-scale abrasive wear tests and corrosion at the same time. The works of Stack *et al.* (2010) and Sun *et al.* (2009) revealed that the test parameters of micro abrasion-corrosion adapted test rig affect the wear mechanism of biomedical alloys, being possible to evidence the transitions between them. They highlighted the crucial influence of the formation and breakdown of a passivation film on the degradation mechanism and synergy effect.

A similar approach to that developed in the current study was introduced by Bello *et al.* (2007). These authors considered three systems:

1 pure abrasion, using a slurry diluted in distilled water;
2 abrasion-corrosion, using a slurry diluted in a corrosive 3.5 per cent NaCl solution; and
3 the corrosion component enhanced by abrasion, where the ball-cratering rig with no SiC abrasive slurry but only using the 3.5 per cent NaCl solution.

They studied three stainless steels: UNS S30403, S31603 and S32760 grades. The S32760 grade delivered the best repassivation performance with negative synergistic characteristics.

More recently, Santos *et al.* (2015) developed a new test rig that consists of a fixed-ball micro-abrasion tester, which had the unique capability of monitoring the forces acting on the contact of abrasion-corrosion processes. They studied an austenitic (AISI 304) and ferritic (AISI 430) stainless steels, obtaining negative synergy on tribo-corrosion conditions for both steels. Their approach also involved studying the same three systems as Bello *et al.* (2007), but with $SiO_2$ particles and 1 N $H_2SO_4$ corrosive solution.

To our knowledge, the approach used by Bello *et al.* (2007) and Santos *et al.* (2015) was not still explored for surface-treated duplex stainless steels. Considering these previous investigations, the current study aims to present the effect of low-temperature plasma nitriding on the synergism between abrasion and corrosion, using a different approach from Bello *et al.* (2007) and Santos *et al.* (2015) to produce pure abrasion.

## 2. Experimental procedures

Samples of super duplex stainless steel SAF 2205 (~3 per cent Mo, 22 per cent Cr, and 5 per cent Ni) were extracted from a bar of 85.5-mm diameter. The cutting process was used to obtain coupons with dimensions of 5 x 20 x 60 mm. After cutting, the specimens were ground and subsequently sanded for a finishing equivalent to a sandpaper #600 grit. Its Vickers hardness is 368 ± 36 $HV_{0.05}$.

### 2.1 Plasma nitriding

After sanding, the samples were washed and cleaned properly for the plasma nitriding treatment, conducted in a pulsed DC reactor. The treatment consists in two steps:

1 an initial sputtering for 20 min under a gas mixture of (25%Ar-75%$H_2$) at 300°C, for removing the passive layer; and
2 nitriding for 10 h under a gas mixture of (25%$N_2$-75%$H_2$), at 380°C.

The temperature and time of nitriding treatment were based on a previous investigation (Pintaude *et al.*, 2019). During all steps, the pressure and voltage were kept constant at 3 Torr (400 Pa) and 600 V, respectively. The parameters plasma-on and plasma-off periods were controlled for assuring a maximum variation for the temperature of ±2°C.

### 2.2 Characterization of nitrided specimens

The microstructure of the nitrided layer was revealed for assessing its thickness, etching polished cross-sections with oxalic acid 10 per cent Vol. in an electrolytic device. The phases of the nitrided layer were analyzed using X-ray diffraction (XRD). The top hardness of layers was determined through the Vickers scale, using 490 mN. The average values corresponded to a series of 10 measurements.

### 2.3 Pure wear ($W_0$) and tribo-corrosion (T) evaluation

The evaluation of wear without corrosion ($W_0$) and tribo-corrosion ($T$) was performed through a micro-scale abrasion test rig, using a free-ball configuration. As a counter-body, a ball of zirconia of 24.5-mm diameter (52.14 g of mass) was employed. The slurry was composed of a water suspension containing 20 per cent m/v of alumina particles, with $d_{50}$ = 6.7 ± 0.3 $\mu$m (Rovani *et al.*, 2019), dissolved in depleted distilled water. For the tribo-corrosive tests, 3.5 per cent of NaCl was added to the slurry. For controlling the corrosion, the test rig was placed into a glovebox (Figure 1). The glovebox volume was filled with nitrogen gas (99.999 per cent minimum) using a flow rate of 10 L/min. After that, the minimum content of nitrogen was controlled using a flow rate of 1 L/min. Using an optical spectrometer, the peak of 844.1 nm, corresponded to the oxygen gas, was monitored to guarantee a maximum of 1 per cent of oxygen inside the chamber. On the opposite, the tribo-corrosive tests were carried out in an open-to-air environment.

**Figure 1** Schematic drawing of glovebox, showing the system used for reproducing wear without corrosion

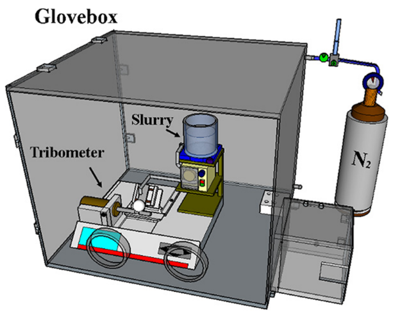

Testing variables used for micro-scale abrasion tests were: a dynamic load of 0.1 N, an axis rotation speed of 300 rpm, a testing time of 18 min, and a drop rate of ~2 ml/min. These parameters were used elsewhere (Rovani *et al.*, 2019) and they assured that all tests were performed within the steady-state regime of wear. For each testing condition, four measurements were done.

### 2.4 Corrosion evaluation $C_0$

Potential-dynamic tests were performed for evaluating the corrosion behavior of the SAF 2205 steel before and after the plasma nitriding. The corrosion rate was calculated considering the Tafel region. Tests were carried out using scanning of potentials in the anodic direction, using a scan rate of 1 mV/s, from 0.3 V below the rest potential up to 1.5 V (reversion point), and finally returning to the initial value of potential. To obtain average values of corrosion parameters, five experiments were carried out at least.

### 2.5 Synergism evaluation (S)

Figure 2 is a flow chart detailing all tests performed in this work. The values of wear rate without corrosion ($W_0$) and tribo-corrosion ($T$) and the value of corrosion rate ($C_0$) obtained on each test procedure were used for synergism calculation. The synergism between wear and corrosion was calculated following the recommendations of ASTM G119-09 Standard.

$$S = T - W_0 - C_0 \tag{1}$$

## 3. Results and discussion

Figure 3 shows the cross-section of nitrided SAF 2205 steel. A continuous and uniform layer can be observed, with an average value of the thickness of 3.0 ± 0.2 $\mu$m. This layer is constituted by a metastable phase so-called S-phase or expanded austenite, which had been confirmed by following XRD results.

**Figure 2** Flow chart detailing the tests performed

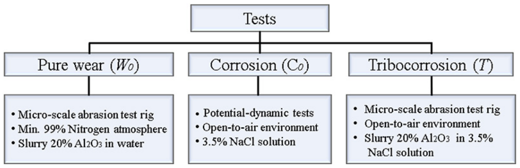

**Figure 3** Cross-section of nitrided SAF 2205 steel (380°C for 10 h)

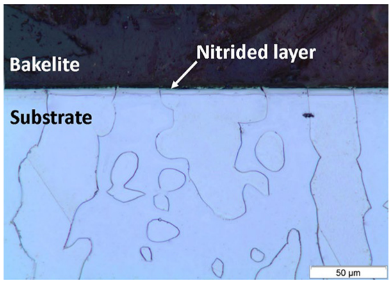

After plasma nitriding, the Vickers hardness of the surface is 1102 ± 178 $HV_{0.05}$. Thus, the surface treatment was able to increase three times the initial hardness. However, this value can be underestimated yet, considering the indentation depth achieved during the test – approximately 1.32 $\mu$m – which corresponds to 44 per cent of layer thickness. This percentage is high enough for the substrate properties had influenced the hardness.

Figure 4 shows the spectrum of XRD for the untreated and nitrided conditions. As expected, the diffractogram relative to the untreated specimen [Figure 4(a)] presents only peaks associated with the austenite ($\gamma$-Fe) and ferrite ($\alpha$-Fe). On the other hand, in the nitrided specimens, one can observe the disappearing of peaks relative to the ferrite and a shift of peaks 1 and 3 [Figure 4(b)], related to the austenite, for smaller angles (peaks I and II). The peaks identified as I and II have been related to the expanded austenite, sometimes called as S-phase, as described by Alphonsa *et al.* (2015) and Cardoso *et al.* (2016). This shift is associated with the increase in the lattice parameter of austenite, caused by the nitrogen supersaturation (Pinedo *et al.*, 2013).

Table I presents the wear rates for systems corresponding to the abrasive wear without corrosion ($W_0$) and tribo-corrosion ($T$). For both material conditions, the wear produced by tribo-corrosion is higher than that observed for the pure wear, indicating the effect of corrosive component for both superficial conditions. The presence of an expanded austenite layer caused a reduction of 50.6 per cent in the pure

**Figure 4** (a) XRD spectrum of untreated SAF 2205 steel, presenting peaks of austenite (2, 3) and (b) XRD spectrum of nitrided SAF 2205 steel, showing peaks of expanded austenite (I, II)

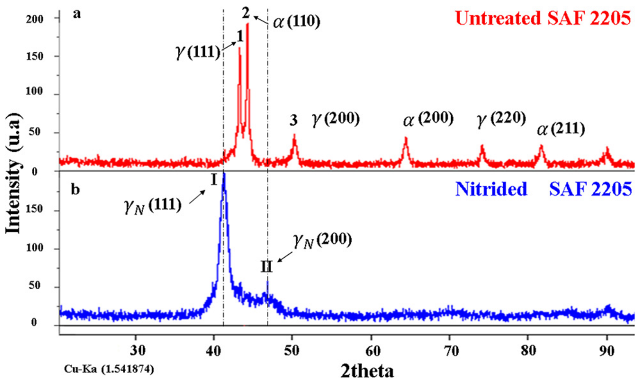

**Table I** Wear rates (mm/year) of SAF 2205 steel for pure wear ($W_0$) and tribo-corrosion ($T$) testing conditions, before and after plasma nitriding

| Condition | Wear rate (mm/year) |
|---|---|
| ***Untreated SAF 2205 steel*** | |
| ***T*** | 11.5 ± 0.3 |
| $W_0$ | 8.3 ± 0.3 |
| ***Nitrided SAF 2205 steel*** | |
| ***T*** | 9.5 ± 0.4 |
| $W_0$ | 4.2 ± 0.6 |

wear and 17.4 per cent in the tribo-corrosion wear rate. Although the benefit of plasma nitriding is observed for both tribo-systems, the expanded austenite reduced much more the wear without corrosion.

Figure 5 presents the worn surfaces revealed in SEM before and after plasma nitriding. The images correspond to the center of craters. Some grooves and indentations marks are indicated by dotted yellow and green lines, respectively. In Figure 5(a) the combined presence of grooves and indentations can be observed, which correspond to the mixed mode of wear, being the grooving more intense for the untreated steel under pure wear. Surprisingly, another situation was found when the SAF 2205 steel was subject to tribo-corrosive system [Figure 5{b)]. The rolling mode of wear became predominant, indicating that the presence of a passive layer could be decisive for the mode of wear.

Figure 5(c) shows the worn surface of the nitrided layer under pure wear condition. In comparison with the untreated steel, the presence of a hard layer acted for reducing the occurrence of grooves. This observation meets the wear rates presented in Table II, where a significant reduction was noted due to the nitrided layer; however, a mixed mode of wear was also presented. In the same sense of abovementioned for the untreated SAF 2205 steel, the change of system from pure abrasion to tribo-corrosion changed the mode of wear, i.e. in Figure 5(d) one can observe the predominance of rolling mode of wear.

Changes in the wear mode during the micro-scale abrasion test can be associated with different width of the wear caused by the abrasive particles (Da Silva and De Mello, 2009). This relation was described in detail by Rovani *et al.* (2019). These authors identified a significant reduction in the $\lambda q$ parameter (~the width of wear track) when the mixed mode changed to grooving mode. This roughness parameter was more sensitive to indicate this kind of change than the $Sq$ (root mean square height).

In Figure 6 one can see the curves obtained in cyclic polarization, and in Table II the average values of corrosion potential ($E_{corr}$), corrosion current ($i_{corr}$), corrosion rate ($C_0$), pitting potential ($E_p$), and the repassivation potential ($E_r$) can be found.

Analyzing these results, it is possible to check that the corrosion potential of the nitrided condition is worse than the untreated one. However, the values of corrosion current and corrosion rate are equivalent, considering the standard deviations. For the localized corrosion, the pitting nucleation and the repassivation

**Table II** Corrosion parameters determined after cyclic polarization for untreated and nitrided SAF 2205 steel

| Corrosion parameters | Untreated SAF 2205 steel | Nitrided SAF 2205 steel |
|---|---|---|
| $i_{corr}$ (µA/cm$^2$) | 0.75 ± 0.52 | 3.3 ± 2.6 |
| $E_{corr}$ (mV vs SCE) | −150 ± 90 | −347 ± 10 |
| $E_p$ (mV) | 1010 ± 70 | 1240 ± 20 |
| $E_r$ (mV) | 897 ± 130 | 1170 ± 30 |
| $C_0$ (mm/year) | (0.8 ± 0.4) $\times 10^{-2}$ | (3.6 ± 3.0) $\times 10^{-2}$ |

**Figure 5** Worn surfaces revealed in SEM

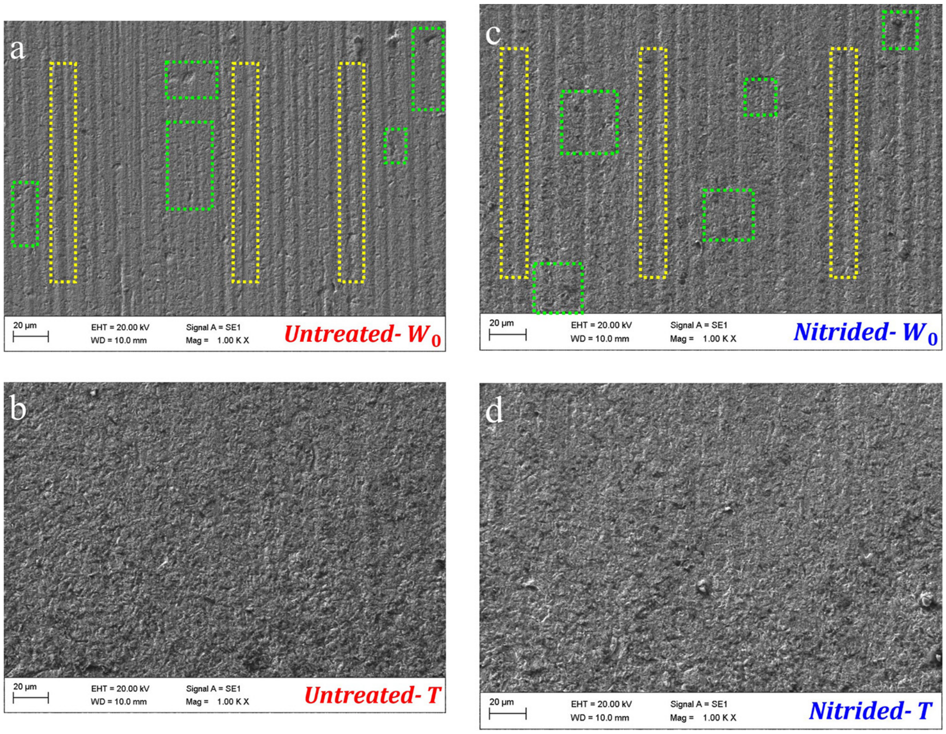

**Notes:** (a), (b) Untreated SAF 2205 steel, pure wear and tribo-corrosion, respectively; (c), (d) nitrided 2205 steel, pure wear and tribo-corrosion, respectively

**Figure 6** Cyclic polarization curves of SAF 2205 steel

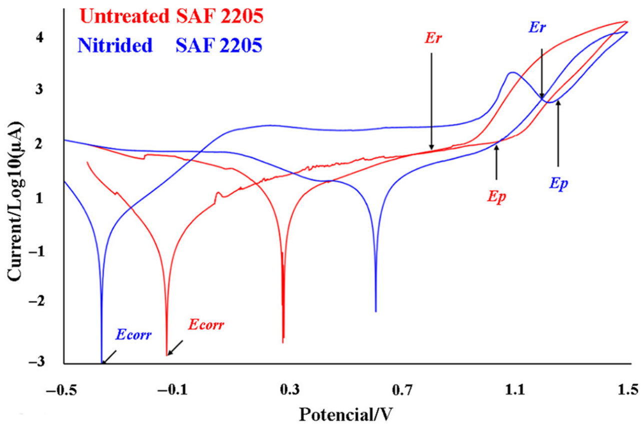

**Notes:** Untreated (red); nitrided (blue)

potentials are larger with the plasma nitriding, which represents a better-localized corrosion resistance and a small resistance to repassivation, compared with the untreated condition.

Besides the bigger size of the area of hysteresis loop means more passive film breakdown and consequently, more difficulty for restoring the damaged passive film. As shown on the curves in Figure 6, this area is higher for the untreated condition which indicates the higher resistance to repassivation. This result agrees with the literature (Jargelius-Pettersson, 1999), which relates that the presence of nitrogen favors the formation of $NH^{+4}$, with consequent reduction of pH within the pitting, as well as an easier repassivation verified by the increase of repassivation potential in nitrogen-enriched samples.

Table III shows the values calculated from equation (1) representing the synergistic effect produced by micro-scale abrasion test with, pure micro-scale abrasion test with corrosion and pure corrosion for SAF2205 steel samples before and after plasma nitriding.

Figure 7 presents a summary for better visualization of pure wear ($W_0$), tribo-corrosion ($T$), corrosion ($C_0$) and synergism (S) for the studied surfaces. These data allow verifying that the sum of pure wear and corrosion components is lesser than the tribo-corrosion component. Therefore, the synergism is positive, indicating that the simultaneous action of abrasion and corrosion intensified the wear. The main beneficial effect of plasma nitriding was on pure wear, related to the surface hardness increase.

As the synergism between wear and corrosion is a real problem in duplex stainless steels applied on offshore oil and gas facilities (Aribo *et al.*, 2013), the low-temperature plasma nitriding process can be a good approach for improving the wear and corrosion resistances. According to the results obtained in the present work, the nitrided steel presented a lower wear rate compared to the untreated material in pure wear and tribo-corrosion conditions.

**Table III** Synergism (S) (mm/year) values of SAF 2205 steel before and after plasma nitriding

| Condition | Synergism S (mm/year) |
|---|---|
| Untreated SAF 2205 steel | 3.2 ± 0.6 |
| Nitrided SAF 2205 steel | 5.3 ± 1.0 |

**Figure 7** Diagram presenting the components of tribo-corrosion (T), pure wear ($W_0$), pure corrosion ($C_0$) and synergism (S) for the untreated and nitrided SAF 2205 steel

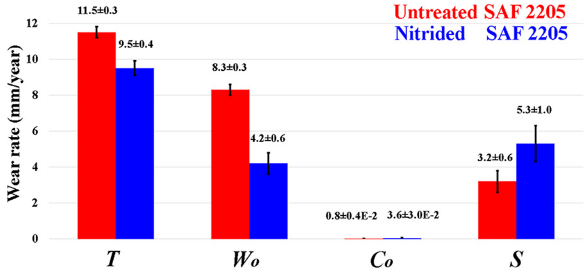

## 4. Conclusions

Micro-scale abrasion tests were performed with and without control of the corrosion component, allowing to describe the synergism between wear and corrosion for the SAF 2205 steel. From the experimental results, the following conclusions can be put forward:

- The plasma nitriding at low-temperature promotes the formation of a continuous layer of expanded austenite with 3-$\mu$m thick; the plasma nitriding promoted an increase in the hardness of SAF 2205 steel from 368 $HV_{0.05}$ to 1102 $HV_{0.05}$.
- The mode of wear changes from the pure abrasion to tribo-corrosion condition, while in the former a mixed mode is observed, the rolling mode was predominant during the tribo-corrosive tests.
- The presence of an expanded austenite layer caused a reduction of 50.6 per cent in the pure wear and 17.4 per cent in the tribo-corrosion wear rate.
- Plasma nitriding improves the resistance to the localized corrosion; the synergism value indicates a positive action for both nitride and untreated samples, indicating that the corrosion is determinant for the tribo-corrosive wear. The synergism was more positive for the nitrided sample than the untreated one.

## References

Alphonsa, J., Raja, V.S. and Mukherjee, S. (2015), "Study of plasma nitriding and nitrocarburizing for higher corrosion resistance and hardness of 2205 duplex stainless steel", *Corrosion Science*, Vol. 100, pp. 121-132.

Aribo, S., Barker, R., Hu, X. and Neville, A. (2013), "Erosion–corrosion behaviour of lean duplex stainless steels in 3.5% NaCl solution", *Wear*, Vol. 302 Nos 1/2, pp. 1602-1608.

Asgari, M., Johnsen, R. and Barnoush, A. (2013), "Nanomechanical characterization of the hydrogen effect on pulsed plasma nitrided super duplex stainless steel", *International Journal of Hydrogen Energy*, Vol. 38 No. 35, pp. 15520-15531.

Bello, J.O., Wood, R.J.K. and Wharton, J.A. (2007), "Synergistic effects of micro-abrasion–corrosion of UNS S30403, S31603 and S32760 stainless steels", *Wear*, Vol. 263 Nos 1/6, pp. 149-159.

Cardoso, R.P., Mafra, M. and Brunatto, S.F. (2016), "Low-temperature thermochemical treatments of stainless steels – an introduction, chapter 4", *An Introduction, Plasma Science and Technology – Progress in Physical States and Chemical Reactions*, IntechOpen, pp. 107-130.

Craidy, P., Briottet, L. and Santos, D. (2015), "Hydrogen–microstructure–mechanical properties interactions in super duplex stainless steel components", *International Journal of Hydrogen Energy*, Vol. 40 No. 47, pp. 17084-17090.

Da Silva, W.M. and De Mello, J.D.B. (2009), "Using parallel scratches to simulate abrasive wear", *Wear*, Vol. 267 No. 11, pp. 1987-1997.

Jargelius-Pettersson, R.F.A. (1999), "Electrochemical investigation of the influence of nitrogen alloying on pitting corrosion of austenitic stainless steels", *Corrosion Science*, Vol. 41 No. 8, pp. 1639-1664.

Lai, C.L., Tsay, L.W. and Chen, C. (2013), "Effect of microstructure on hydrogen embrittlement of various stainless steels", *Materials Science and Engineering: A*, Vol. 584, pp. 14-20.

Marques, F., Da Silva, W.M., Pardal, J.M., Tavares, S.S.M. and Scandian, C. (2011), "Influence of heat treatments on the micro-abrasion wear resistance of a superduplex stainless steel", *Wear*, Vol. 271 Nos 9/10, pp. 1288-1294.

Pereira Neto, J.O., Silva, R.O.D., Silva, E.H.D., Moreto, J.A., Bandeira, R.M., Manfrinato, M.D. and Rossino, L.S. (2016), "Wear and corrosion study of plasma nitriding F53 super duplex stainless steel", *Materials Research*, Vol. 19 No. 6, pp. 1241-1252.

Pinedo, C.E., Varela, L.B. and Tschiptschin, A.P. (2013), "Low-temperature plasma nitriding of AISI F51 duplex stainless steel", *Surface and Coatings Technology*, Vol. 232, pp. 839-843.

Pintaude, G., Rovani, A.C., das Neves, J.C.K., Lagoeiro, L.E., Li, X. and Dong, H.S. (2019), "Wear and corrosion resistances of active screen plasma-nitrided duplex stainless steels", *Journal of Materials Engineering and Performance*, Vol. 28 No. 6, pp. 3673-3682.

Rovani, A., Rosso, T. and Pintaude, G. (2019), "On the use of microscale abrasion test for determining the particle abrasivity", *Journal of Testing and Evaluation*, Vol. 49, In press, available at: https://doi.org/10.1520/JTE20180576

Santos, M., Labiapari, W., Narvaez Ardila, M., Da Silva Junior, W. and de Mello, J.D.B. (2015), "Abrasion-corrosion: new insights from force measurements", *Wear*, Vols 332/333, pp. 1206-1214.

Stack, M.M., Rodling, J., Mathew, M.T., Jawan, H., Huang, W., Park, G. and Hodge, C. (2010), "Micro-abrasion–corrosion of a Co–Cr/UHMWPE couple in ringer's solution: an approach to construction of mechanism and synergism maps for application to bio-implants", *Wear*, Vol. 269 Nos 5/6, pp. 376-382.

Sun, D., Wharton, J.A. and Wood, R.J.K. (2009), "Micro-abrasion mechanisms of cast CoCrMo in simulated body fluids", *Wear*, Vol. 267 No. 11, pp. 1845-1855.

## Further reading

ASTM G119-89 (2015), Standard Practice for Calculation of Corrosion Rates and Related Information from Electrochemical Measurements, ASTM International.

## Corresponding author

**Giuseppe Pintaude** can be contacted at: giuseppepintaude@gmail.com

*Materials Research*. 2022; 25:e20220179
DOI: https://doi.org/10.1590/1980-5373-MR-2022-0179

# Pitting and Crevice Corrosion Behavior of the Duplex Stainless Steel UNS S32205 Welded by Using the GTAW Process

***Yamid E. Nuñez de la Rosa***[a]*, ***Oriana Palma Calabokis***[a], ***Gloria M. Pena Uris***[b],

***Paulo César Borges***[a]

[a]*Universidade Tecnológica Federal do Paraná (UTFPR), 81280-340, Curitiba, PR, Brasil.*
[b]*Universidade de Vigo, Centro de Investigación en Tecnoloxías, Enerxía e Procesos Industriais (CINTECX), Enxeñaría da Corrosión e Materiais (ENCOMAT), 36310, Vigo, Spain.*

Received: April 01, 2022; Revised: August 28, 2022; Accepted: October 19, 2022

This study investigated the pitting and crevice corrosion behavior of the gas tungsten arc welding (GTAW) process in the UNS S32205 according to industrial parameters. Results revealed that the welding process presented a weld metal chemical composition similar to the base metal and an adequate balance of the austenite and ferrite phases. No relevant variation in the hardness was observed and XRD spectra did not identify the presence of deleterious phases in the weld bead. Cyclic polarization tests revealed similarities between welded and base metal samples (20±2°C, NaCl 3.5% wt.). When comparing the behavior obtained in the crevice, and pitting tests, a decrease in the corrosion resistance was observed in the presence of a crevice former. The SEM-EDS proved that the attack occurred mainly in secondary austenites. Profilometry measurements revealed that the crevice corrosion in the weld region was deeper than in the base metal. However, considering the welded samples as a unit, making no difference between regions: weld metal, HAZ, and base metal, the average crevice corrosion depth was comparable to that of the base metal samples. Finally, it was concluded that the welding process used for the UNS S32205 steel did not harm its corrosion resistance.

**Keywords:** *DSS, UNS S32205, weld, GTAW, pitting corrosion, crevice corrosion.*

## 1. Introduction

Duplex stainless steels (DSS) belong to a family of steels that present a two-phase microstructure with roughly equal proportions of austenite (γ) and ferrite (α) at room temperature[1-4] (Figure 1). This balance between the phases results in an interesting combination of properties, namely, mechanical resistance, toughness, corrosion resistance, and weldability[5-8].

The DSS UNS S32205 (3%Mo, 22%Cr, and 5%Ni) is mainly used in the chemical industry, oil transportation, food, paper and cellulose[9-13]. In these areas, pipes, tanks, and other components require a welding process that does not alter their mechanical and corrosion resistance properties. The welding processes that are mostly used in these steels according to the literature are: GMAW (Gas Metal Arc Welding)[9,14,15], FCAW (Flux-Cored Arc Welding)[16,17], SAW (Submerged Arc Welding)[18], SMAW (Shield Metal Arc Welding)[13,19], and GTAW (Gas Tungsten Arc Welding)[17,20-22].

All the processes listed above, depending on the welding conditions can generate undesirable changes in the ferrite-austenite ratio and/or in the distribution of the alloying elements in the DSS weld metal (WM) and in the HAZ. These could be a consequence of the thermal gradients resulting from the alteration of the welding speed, current, and tension[1,23-25]. Unsuitable heat input can promote the formation of deleterious phases that alters the hardness and harms the corrosion resistance[26]. To prevent such undesirable changes, some studies suggest that the heat input recommended for the DSS UNS S32205 must be around 0.5 kJ/mm up to 2.5 kJ/mm[13,14,23,27-30].

The GTAW process is one of the most popular DSS welding methods[31]. This process outstands for providing a better ferrite-austenite ratio (around 50% of each) when compared to other welding processes, according to the standards TAPPI TIP 0402-29 and Norsok M-601, 2016[25,29,32]. However, every welding process generates microstructural differences that might hamper the material corrosion resistance in the conditions in which DSS is used[33]. Microstructural characteristics depend on the choice of the welding procedure and the process parameters (current, potential, speed, heat input, and cooling rate), the filler material, the materials to be welded, and the shielding gas. As a result, welded DSS evaluation focuses on the investigation of pitting corrosion resistance in chloride environments, mainly employing cyclic potentiodynamic polarization[14,34-36] and critical pitting temperature (CPT ASTM G150)[35,37]. Also, other techniques have been evaluated such as the modified double loop electrochemical potentiokinetic reactivation[38], electrochemical impedance[33], and immersion tests[13]. A study put forward by Zhou et al.[5] that investigated 2101 lean duplex stainless steel welded using the TIG (Tungsten Inert Gas) process evaluated the material susceptibility to generalized, pitting, and transpassive corrosion with a single electrochemical

---

*e-mail: yamid@alunos.utfpr.edu.br

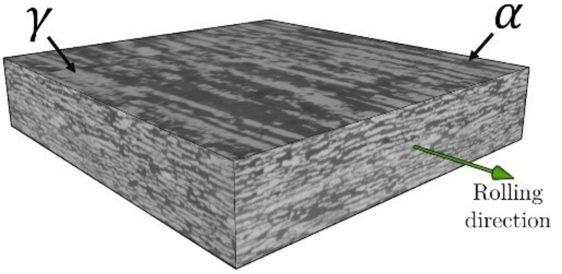

**Figure 1.** DSS UNS S32205 microstructure, ferrite phase (α: darker) and austenite phase (γ: lighter).

technique known as bipolar electrochemistry technique. Zhou et al.[5] revealed that the austenite morphologies were preferentially attacked by pitting and transpassive corrosion. Besides, the un-balanced microstructure, the formation of deleterious phases, and the high chemical composition heterogeneity weaken the corrosion resistance in different DSS welding joints, as reported in previous works[5,6,34,36-38].

Studies on localized corrosion in welded DSS focus mainly on pitting corrosion. However, there are several practical cases of geometries that lead to crevice corrosion such as gaskets, washers, screw heads, flanged pipes, pipe support brackets, lap joints, and surface deposits that make this type of corrosion less evident and often neglected[5,39]. In fact, weld beads are surface heterogeneities around which liquids can be retained, which favor crevice corrosion[5,39]. Among the studies on welded DSS, only Zhou et al.[5] reported crevice corrosion in the interface between the sample and the lacquer covering it without studying it systematically. Taking into consideration that the DSS UNS S32205 welding processes are so common in the industrial the main purpose of this study aimed to investigate the pitting and crevice corrosion resistance in a NaCl 3.5% wt. of the welded DSS UNS S32205 using the GTAW process.

## 2. Experimental Procedure

### 2.1. Material and welding process

Plates of DSS UNS S32205 with 4 mm in thickness, 300 mm in length and 50 mm in width, were used as base materials. The GTAW technique was utilized in preparing DSS joints. Argon (12-20 L/min) was used as shielding gas in the 1G position and a stainless steel ER-2209 (Lincoln®) wire (Ø=2.5 mm) was used as consumable electrode. Welding was carried out using a current of 110-200 A and arc voltage of 23-28 V. The welds were made by a specialized welding company that works for the Brazilian pulp and paper industries.

Chemical composition of the base material and weldments was determined by Positive Material Identification (PMI) technique: (Olympus-DELTA Premium) and Scanning Electron Microscopy (SEM) and Energy Dispersive X-ray Spectroscopy (EDS): (Zeiss-EVO MA15) was also used to perform analysis of sample surface.

Two types of samples were analyzed: untreated UNS S32205 sheet samples, identified as BM (base metal) and samples with weld joint called BM-WM (these samples containing base metal, heat affected zone, and weld metal region). The surfaces were ground with emery papers up to #1200 mesh and the samples were cold mounted in epoxy resin with a copper wire assembled for electric contact for the electrochemical tests (pitting and crevice corrosion tests).

### 2.2. Microstructural and microhardness analyses

BM and BM-WM samples were polished with 1 μm alumina and etched with modified Behara (100 ml $H_2O$ + 20 ml HCl + 0.4 g potassium metabisulfite) at room temperature for 600 s[40]. The BM, HAZ, and WM regions were analyzed by optical microscopy (OM) using a Olympus-BX51 and the free software *Image J.* Ten micrographs were randomly obtained for each region along the welded sheets in order to compute the average phases percentage in each zone.

The existence of possible harmful phases was determined by X-ray diffraction patterns using a Shimadzu XRD-7000 diffractometer under CuK-α (λ = 1,54060 Å) radiation, operating at 40 kV/30 mA. The scanning range was: 20°–120°, with a step width of 0.02° and 1 s per step as collecting time. The Bragg angles, 2θ, and the interplanar spacing (d-spacing) corresponding to the detected peaks were compared with the standard values from the International Centre for Diffraction Data's Powder Diffraction File (JCPDS- ICDD).

The microhardness determination of the welded samples was measured, carried out at the top and perpendicular to the weld bead. The equipment used was a Shimadzu Dynamic Ultra Micro Hardness Testers DUH-21S, using a load of 50 g for 10 s and a space between indentations of 0.5 mm according to the ISO 14577-1 standard.

### 2.3. Cyclic Polarization tests (CP)

Aiming to determine the pitting corrosion behavior, CP tests were carried out in a three-electrode electrochemical cell. The working electrode (WE) was the mounted sample (4 $cm^2$), the reference electrode (RE) was a KCl saturated silver-silver chloride (Ag-AgCl/sat) electrode, and the auxiliary electrode (AE) was a graphite rod. All electrodes are connected to the potentiostat (PalmSens, model EmStat3; software PSTrace 5). Each test started after the open circuit potential (OCP) stabilization, carried out for an hour. Next, a potential scanning was performed in the anodic direction –0.2 V respecting the OCP potential up to the 1.7 V potential (vs Standard Hydrogen Electrode, SHE) where the polarization was reversed to the cathodic direction. The tests were carried out at 20 °C in a NaCl 3.5% wt. and a 1 mV/s scanning rate. All potentials presented in this study has been converted into the SHE.

### 2.4. Crevice corrosion tests

The susceptibility to crevice corrosion was evaluated using a PD-PS-PD test consisting of three consecutive stages, as suggested by Palma et al.[41]. After OCP stabilization for an hour, a potentiodynamic (PD) polarization stage, scanning potential from –0.2 V respecting the OCP to 1.5 V (vs. SHE) at 1 mV/s. Immediately afterward, the potentiostatic (PS) stage is performed, holding 1.5 V for an hour. Finally, a reverse scanning in the cathodic direction is performed (PD stage).

The mounted sample and the crevice former were placed in a corrosion cell devised by Palma Calabokis et al.[41], as shown below (Figure 2).

The position of the samples avoids the deposition of the corrosion products on the sample surface. Constant contact pressure of 508 kPa was imposed between the crevice former and the sample surface, using standardized masses of 3 kg, and, as a result, the crevice mouth standardization was guaranteed in all tests.

### 2.5. Surface analysis after the crevice corrosion tests

After the corrosion tests, the samples were cleaned in an ultrasound bath with ethyl alcohol (70%). The surfaces were analyzed using optical microscopy, stereoscopic microscopy, scanning electron microscopy + EDS, and 2D contact profilometry.

## 3. Results

### 3.1. Chemical composition

Table 1 shows the average weight percentages (wt.%) of the main alloying elements. Using the PMI technique, the percentages were determined in five different points of the base metal and weld metal regions of welded samples. Also, Table 1 shows the nominal composition of UNS S32205 (ASTM A240) and the composition of the consumable wire indicated in the supplier datasheet for comparison reasons. The distribution of the alloying elements between the austenite and ferrite phases was assessed by SEM-EDS, performing 28-point measurements in the weld metal zone. Average results are shown in Table 1.

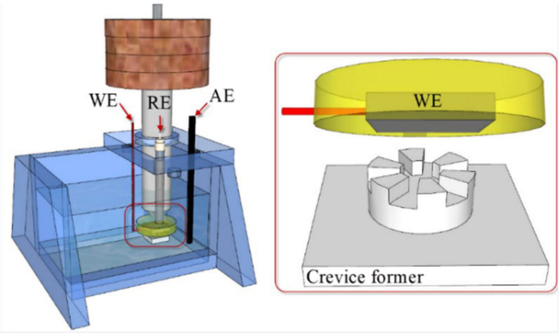

**Figure 2.** Scheme of the corrosion cell and crevice former used in the crevice corrosion tests (Adapted from Palma Calabokis et al., 2021[41]).

As verified from Table 1, while the alloying weight percentage of the main alloying elements in the base metal is close to the nominal values (according to the ASTM A240 standard), this percentage rises slightly in the welded area due to the contribution from the consumable electrode (ER-2209).

The distribution of the elements was rather uniform between austenite and ferrite in the weld metal. Although a slight concentration of Cr and Mo is observed in the ferrite and of Ni in the austenite, the difference is very small: it falls within the range of dispersion of the measurements. These results agree with those reported by Geng et al.[20], Zhang et al.[42], and Zhang et al.[38], who studied the double and single-pass GTAW and the FCAW welding process in the DSS UNS S31803, respectively.

### 3.2. X-ray diffraction

Figure 3 presents the X-ray patterns obtained from the base metal (blue) and weld metal (red) regions of the BM-WM samples. Note that both spectra show the same diffraction peaks characteristic of ferrite (α) and austenite (γ) crystalline structures, with very little difference in relative intensity. No peaks corresponding to deleterious phases were found (such as sigma phase, chi phase, chromium nitrides).

### 3.3. Phase quantification

The microstructure of the DSS UNS S32205 in the three analyzed regions is shown in Figure 4: a) base metal

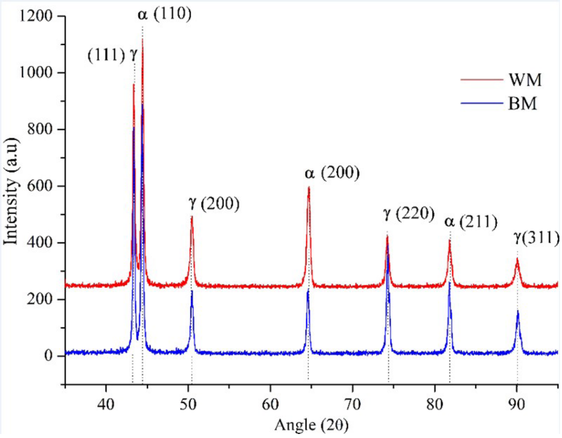

**Figure 3.** X-ray diffraction patterns for DSS UNS S32205 samples in the base metal (BM; blue) and in the weld metal (WM; red) regions and corresponding Miller indexes.

**Table 1.** Nominal composition of DSS UNS S32205 (ASTM A240) and the consumable electrode (datasheet) compared to the average values determined by PMI technique and elemental distribution between phases in the weld zone (SEM-EDS).

| | Cr wt.% | Ni wt.% | Mo wt.% | Mn wt.% |
|---|---|---|---|---|
| **UNS S32205 (ASTM A240)** | 22.0 – 23.00 | 4.5 – 6.5 | 3.0 – 3.5 | 2.0 |
| **Base metal (PMI)** | 22.17 ± 0.24 | 5.72 ± 0.03 | 3.19 ± 0.01 | 1.23 ± 0.05 |
| **Electrode ER-2209 (Datasheet)** | 23.3 | 8.5 | 3.38 | 1.43 |
| **Weld metal (PMI)** | 22.95 ± 0.25 | 7.88 ± 0.22 | 3.40 ± 0.04 | 1.64 ± 0.23 |
| **Austenite in the weld metal (SEM-EDS)** | 22.46 ± 0.93 | 7.48 ± 0.71 | 3.21 ± 0.36 | 1.49 ± 0.11 |
| **Ferrite in the weld metal (SEM-EDS)** | 23.27 ± 0.23 | 6.86 ± 0.48 | 3.59 ± 0.22 | 1.47 ± 0.11 |

(BM), b) heat-affected zone (HAZ), and c) weld metal zone (WM). In all micrographs, the darker areas correspond to the ferritic matrix and the lighter areas correspond to the austenitic phase.

Figure 4a shows the typical DSS microstructure where islands of austenite (γ), elongated in the rolling direction, are surrounded by the continuous ferrite phase (α). The micrograph in Figure 4b presents the optical microstructure of the transition region of the welded DSS UNS S32205 from the base metal, on the left, to the weld region on the right, where the microstructure is similar to that of Figure 4c. In the middle, an intermediate microstructure, corresponding to the HAZ, can be observed.

Figure 4c corresponds to the weld metal region, where different austenite morphologies are seen: grain boundary austenite (GBA), Widmanstätten austenite (WA), and intragranular austenite (IGA). These are morphologies characteristic of the solidification process during cooling[14,40,43]. From the molten metal, only α phase is directly formed, and austenite is subsequently originated from ferrite transformation in the solid-state. GBA nucleates at the grain boundaries as can be seen in Figure 4b, c, and can be continuous or discontinuous depending on the cooling speed. WA nucleates at the ferrite or GBA grain boundaries, and grows aligned along specific planes that are parallel one to another. Finally, IGA is identified as small islands scattered along with the ferritic matrix[14,44] as can be seen in Figure 4b, c.

Figures 4d-f presents the binary images of Figure 4a-c., which have been processed using the free software *Image J* to quantify the phases. Table 2 shows the results obtained from this analysis with corresponding standard deviations. The quantitative analysis of the volumetric fractions of the ferrite and austenite phases in the base metal (BM) showed proportions close to the expected (~50%). The TAPPI TIP 0402-29 standard[45] establishes that the phase balance in the weld metal zone must have at least 30% ferrite. At the

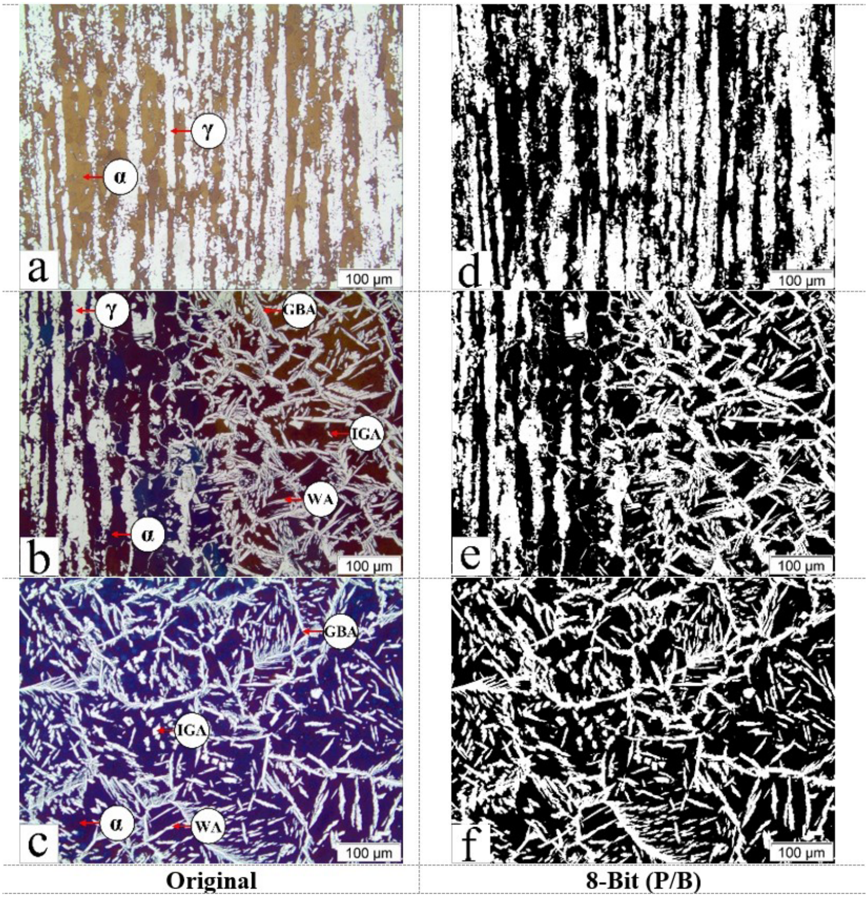

**Figure 4.** Optical micrograph of the surface top etched with modified Behara for 600 s in the: a. BM, b. HAZ, and c. WM. d-f. Binary images corresponding to the images a-c.

**Table 2.** Percentage of austenite and ferrite phases in BM, BM-HAZ-WM, and WM determined at the top of the DSS UNS S32205 welded samples.

| BM region | | BM-HAZ-WM region | | WM region | |
|---|---|---|---|---|---|
| γ | α | γ | α | γ | α |
| 52% ± 4% | 48% ± 4% | 35% ± 4% | 65% ± 4% | 45%± 2% | 55%± 2% |

same time, the Norsok M-601 standard[46], establishes that the austenite fraction cannot be below 25%. Considering the results presented in Table 2, the phase balance is within the limits set forth in both standards. The phase quantification in the welded samples (Table 2) revealed that the welding process used favored a balanced microstructure between ferrite and austenite as well as a similar distribution of alloy elements in the weld metal and the base metal (Table 1) as provided for in the TAPPI TIP 0402-29[45] and Norsok M-601[46] standards. On the other hand, in the BM-HAZ-WM transition (Table 2), a slight increase in the ferrite content was observed, which is usually associated with the material heating and cooling cycles during welding, in agreement with those obtained in other DSS studies[15,38,47]. However, this phase balance at the BM-HAZ-WM transition meets the requirements of the standards listed above.

### 3.4. Microhardness

Microhardness indentations carried out along a direction perpendicular to the weld bead are shown in Figure 5. The microhardness profile was carried out at the top of the BM-WM samples starting from the base metal, going through the weld bead, and reaching the base metal again.

Figure 6 shows the curve of the Vickers microhardness ($HV_{0.05}$) values measured along the profile as a function of distance. From this figure, it is observed that the hardness profile shows that the welding process used in the DSS UNS S32205 was adequate favorable since the hardness values in the weld bead and HAZ transition are close to the BM. The maximum and minimum values in these measurements were 343 $HV_{0.05}$ and 293 $HV_{0.05,}$ respectively with an average value of 328 ± 11 $HV_{0.05}$, in agreement with Tahaei et al.[22]. Those authors confirmed that uniform hardness values along the regions (BM-HAZ-WM) showed a direct relation with a suitable balance between microstructural phases and their chemical composition, without deleterious phases using the TIG welding process in duplex steel UNS S32304[22].

### 3.5. Cyclic polarization tests (CP)

Figure 7 shows the most representative CP curves obtained in the base metal (blue), in the welded samples (red), and the variation of OCP with immersion time. Table 3 lists the average values of the parameters of interest corresponding to the triplicates of these tests. Student T-tests were carried out (3 samples of each condition; confidence interval 95%) to confirm whether there were statistical differences between the average parameters (listed in Table 3) of the BM and BM-WM specimens. Therefore, the $E_R$ and $E_{bd}$ potentials were confirmed as statistically equal in both conditions. However, the BM condition presented more noble values for the $E_{Corr}$ potential when compared to the BM-WM, which suggests the BM greater resistance to generalized corrosion[43]. In addition, the passivation current density lower value ($i_{\mathrm{pass}}$) in the BM suggests that the passive layer formed on them is more protective than that formed on the welded specimens. Also, the corrosion current ($i_{\mathrm{corr}}$) and, consequently, the corrosion rate was lower in BM-WM. In general terms, the electrochemical behavior was not harmed by the welding process when compared to the results reported by Zhou et al.[5], Shin et al.[36], Geng et al.[20], and Tavares et al.[48] on DSS welding. In particular, Zhou et al.[5], Geng et al.[20], and Tavares et al.[48] associated the differences of corrosion susceptibility with changes in phase fraction and local weld chemistry of the DSS GTAW joints. In the present work, the selected parameters for the GTAW welding process performed on DSS UNS S32205 have led to a microstructure almost balanced in austenite-ferrite in the welded joint, with no deleterious phases present such as intermetallic phases, carbides, or nitrides. The presented results of chemical composition, XRD, and the balance microstructure in the welded material meet the requirements of the standards, therefore, a good corrosion resistance of the welded union can be expected.

### 3.6. Crevice corrosion tests (PD-PS-PD)

The susceptibility to crevice corrosion was evaluated in a specially designed corrosion cell, using a PTE crevice former with 6 crevice slots, by a PD-PS-PD method as it was previously indicated. Figure 8 shows the most representative curves of the crevice corrosion behavior tests and their respective OCP in the BM and the welded piece BM-WM. Table 4 presents the mean values and standard deviations

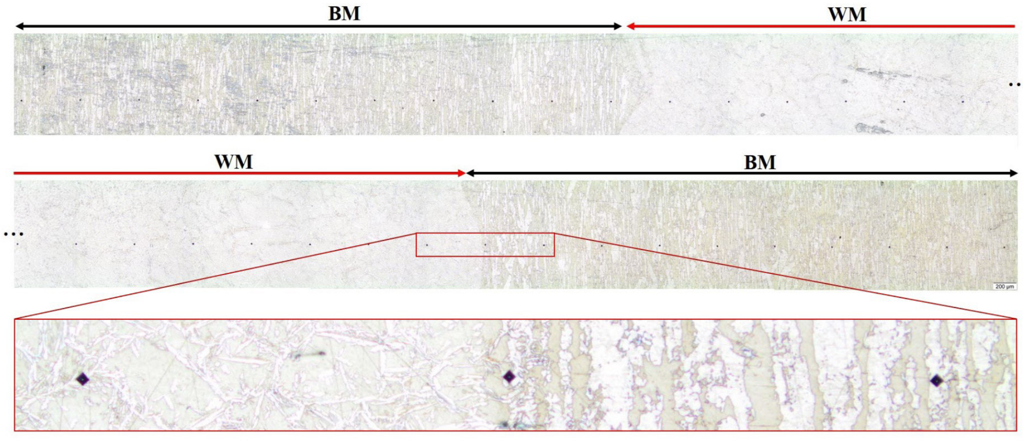

**Figure 5.** Microhardness profile ($HV_{0.05}$) carried out along the surface of the welded samples, perpendicular to the weld bead. Indentations were performed every 0.5 mm.

of the parameters of interest corresponding to triplicate samples. As in section 3.5, statistical analyses were carried out of both conditions, which revealed that only the mean values of potential $E_{bd}$ differed between BM and BM-WM. The remaining parameters of interest (Table 4) were statistically similar, which shows that the crevice corrosion behavior was not influenced by the welding process, except the breakdown potential.

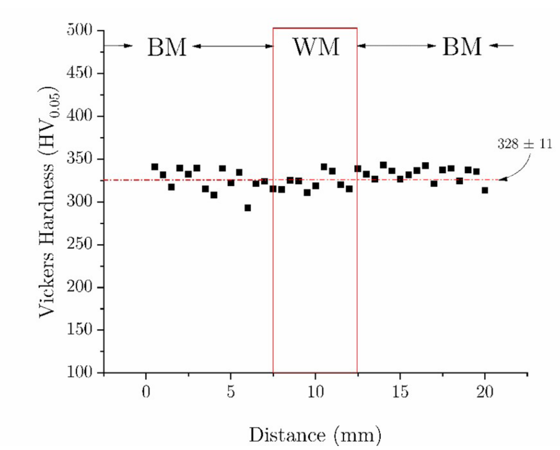

**Figure 6.** Microhardness values ($HV_{0.05}$) as a function of the distance (mm), indentations were carried out every 0.5 mm.

In addition, when comparing the crevice test values (Table 4) with those obtained in the CP tests (Table 3) a general reduction in the potentials $E_R$, $E_{bd}$, and $E_{Corr}$ was observed in both BM and BM-WM as well as an increase in the corrosion and passivation current densities, because of the reactions that occur due to the crevice former contact.

Figure 9 shows two representative curves of the current density as a function of time in the second step of the crevice corrosion tests (potentiostatic polarization, PS). It could be noticed that the current density keeps increasing throughout the test time and showed similar values for both conditions investigated. Therefore, in the PS step, the welded material showed a localized crevice corrosion behavior comparable to the base material, which had been correlated with the same repassivation potential values $E_R$ (Table 4).

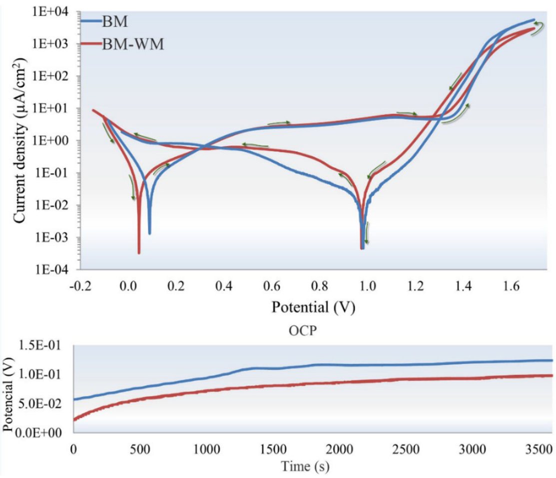

**Figure 7.** Cyclic polarization curves in BM and BM-WM samples in NaCl 3.5% solution (20 ± 2 °C, 1 mV/s), and their corresponding OCP.

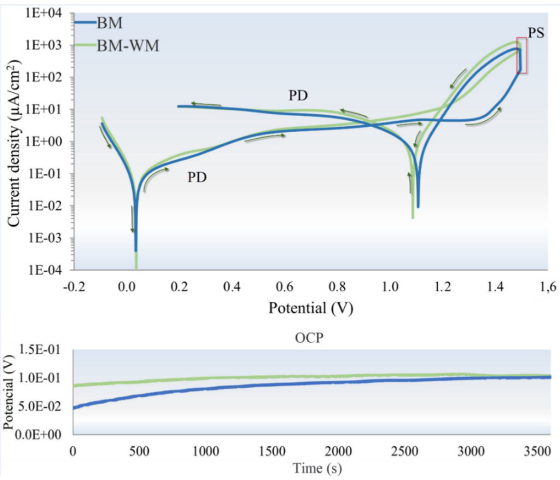

**Figure 8.** Crevice corrosion tests curves in BM and BM-WM in NaCl 3.5% solution (20 ± 2 °C), and their corresponding OCP.

**Table 3.** Mean values and standard deviations of the repassivation potential ($E_R$), breakdown potential ($E_{bd}$), passivation current density ($i_{pass}$), corrosion current density ($i_{Corr}$), corrosion potential ($E_{Corr}$) and corrosion rate ($C_0$) of triplicate CP tests in BM and BM-WM in NaCl 3.5% wt. (20 ± 2 °C).

| | | $E_R$ (V) | $E_{bd}$ (V) | $i_{pass}$ (µA/cm²) | $i_{Corr}$ (µA/cm²) | $E_{Corr}$ (V) | $C_0$ (mm/ano) |
|---|---|---|---|---|---|---|---|
| **BM** | $\bar{x}$ | 1.310 | 1.384 | 2.715 | $7.43 \times 10^{-3}$ | 0.081 | $8.85 \times 10^{-5}$ |
| | $\sigma$ | 0.20 | 0.020 | 0.178 | $0.93 \times 10^{-3}$ | 0.011 | $1.11 \times 10^{-5}$ |
| **BM-WM** | $\bar{x}$ | 1.254 | 1.354 | 3.646 | $4.60 \times 10^{-3}$ | 0.044 | $5.48 \times 10^{-5}$ |
| | $\sigma$ | 0.041 | 0.023 | 0.179 | $0.34 \times 10^{-3}$ | 0.004 | $0.40 \times 10^{-5}$ |

**Table 4.** Mean values and standard deviations of the parameters of interest in the triplicate crevice tests in BM and BM-WM in NaCl 3.5% solution (20 ± 2 °C).

| | | $E_R$ (V) | $E_{bd}$ (V) | $i_{pass}$ (µA/cm²) | $i_{Corr}$ (µA/cm²) | $E_{Corr}$ (V) | $C_0$ (mm/ano) |
|---|---|---|---|---|---|---|---|
| **BM** | $\bar{x}$ | 1.186 | 1.339 | 3.469 | 0.012 | 0.036 | $1.4 \times 10^{-4}$ |
| | $\sigma$ | 0.004 | 0.019 | 0.341 | 0.004 | 0.014 | $0.5 \times 10^{-4}$ |
| **BM-WM** | $\bar{x}$ | 1.154 | 1.252 | 3.394 | 0.021 | 0.071 | $2.52 \times 10^{-4}$ |
| | $\sigma$ | 0.043 | 0.004 | 0.525 | 0.009 | 0.010 | $1.07 \times 10^{-4}$ |

### 3.7. Sample surface analyses after crevice corrosion tests

After the corrosion tests, the surface of the samples was carefully examined. Figure 10a and Figure 10b show macroscopic images obtained by stereomicroscope (Olympus SZX10 series) of the six attacked sites formed under the crevice former in the BM and BM-WM samples subjected to PD-PS-PD tests, respectively. The dotted lines in Figure 10b separate the base metal region (upper and lower part) from the weld metal region (middle).

According to stereoscope images shown in Figure 10, it was observed that during the crevice corrosion tests on both the base metal sample (BM) and the weld metal sample (BM-WM), the crevice former defined a profile irregular localized attack. Note that in the welded sample (Figure 10b), the regions corresponding to BM and WM are marked with horizontal lines. Of these regions, a morphological difference in corrosion can be clearly distinguished, where the WM regions presented a more scattered attack outside the areas limited by the crevice former.

Figure 11a corresponds to the crevice attacked site micrograph (*) of Figure 10a (base metal), while Figure 11b-d show its enlargement. Figure 11c shows that no pits were detected inside these boundaries on the BM sample's surface. Also, it is possible to observe in Figure 11b-d that there was an electrochemical attack that revealed the microstructure of the whole piece surface (with and without contact with the crevice former), as seen by Hang et al.[49] and Yang et al.[50], in many DSS. However, elemental chemical characterizations were carried out using SEM-EDS to differentiate the austenitic phase regions (Cr: 20.75 ± 0.19%wt., Ni: 6.18 ± 0.14%wt., Mo: 2.4 ± 0.08%wt.) from the ferritic ones (Cr: 23.38 ± 0.28%wt., Ni: 3.99 ± 0.23%wt., Mo: 3.7 ± 0.23%wt.). In this regard, it was not possible to identify which phase presented greater susceptibility to corrosion. Both phases were equally consumed at the crevice former boundaries (crevice mouth). Besides, the α/γ, α/α, and γ/γ boundaries were selectively attacked, as shown in Figure 11b and Figure 11d.

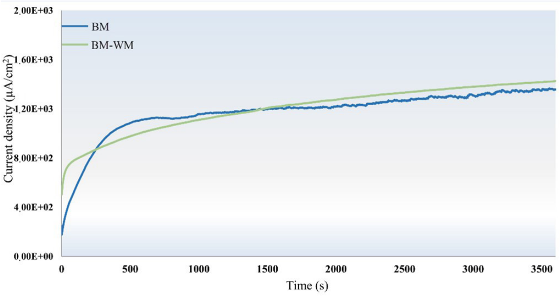

**Figure 9.** Current density comparative curves as a function of time during the potentiostatic step (PS) in the crevice corrosion test in BM and BM-WM in NaCl 3.5% solution (20 ± 2 °C).

In the crevice corrosion tests, the crevice former generated an opening large enough to allow electrolyte stagnation. Once the solution is in the occluded region, it changes because of the anodic and cathodic reactions until it reaches the critical composition that disrupts the passive film[51]. Finally, the cathodic reactions, mainly oxygen reduction, are inhibited inside the crevice sites because of the oxygen depletion within the crevice and, therefore, are largely confined to the exterior surfaces of the sample (out of the crevice former). Hence, the anodic reactions are limited inside the crevice sites accelerating the dissolution and metal hydrolysis reactions that nucleate at the most susceptible regions, phases, or microstructural defects[51]. Han et al.[49], Zeng et al.[52] and Yang et al.[50], observed that crevice corrosion resistance of ferrite was lower than austenite in neutral NaCl medium for the UNS S31803, UNS S32205, and UNS S32101, respectively. Besides, Torres et al.[53] and Palma Calabokis et al.[41] observed that the initiation of crevice corrosion in 25Cr super DSS started at the grain boundary between phases, followed by selective corrosion of one of the phases depending on the thermochemical treatment. Finally, all studies in DSS agree that the austenite and ferrite phases are equally consumed in the region of greater crevice corrosion depth[41,53,54]. In this work, the base metal samples (BM) presented a similar behavior: corrosion appears to start at grain boundaries, followed by dissolution of both phases, as seen in the magnifications of Figure 11 b,d.

Figure 12 shows the crevice attacked site (**) of Figure 10b formed in the BM-HAZ-WM transition region, indicated by

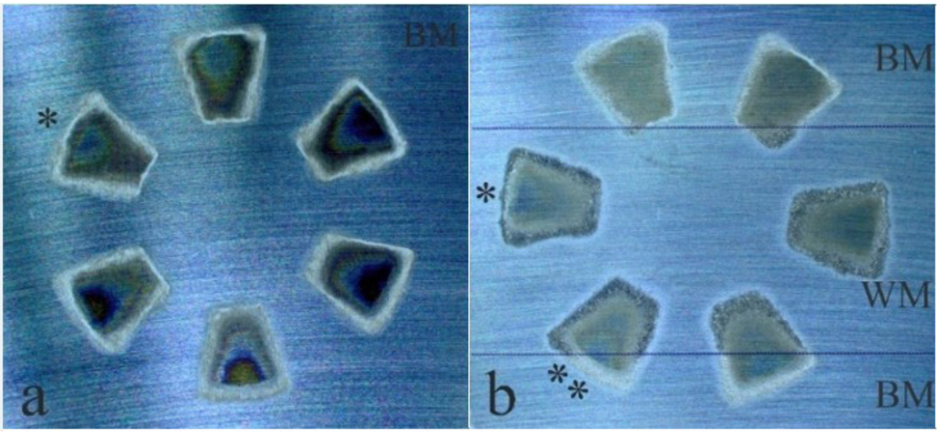

**Figure 10.** Macrograph of the surface samples in crevice corrosion tests in NaCl 3.5% wt. solution a. Base metal (BM), b. Base metal-weld metal (BM-WM).

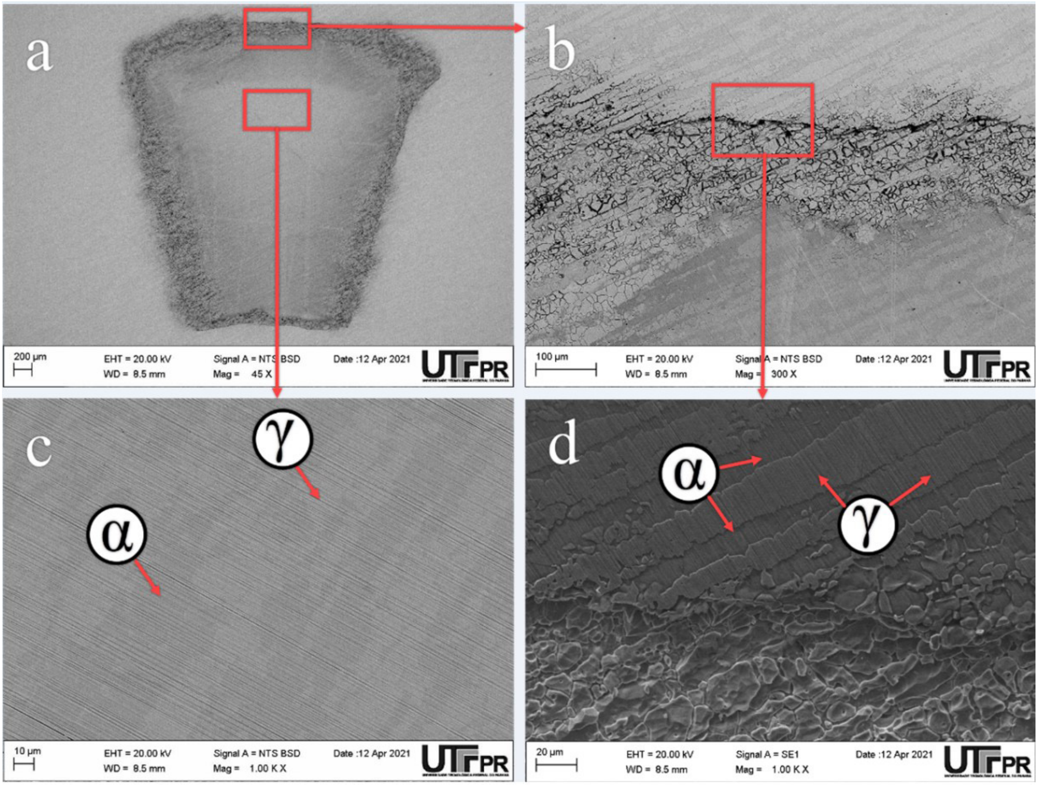

**Figure 11.** a. SEM micrographs of the crevice attacked site (* in Figure 10a) generated in a BM sample in PD-PS-PD tests in NaCl 3.5% wt. solution. b-d. Magnifications.

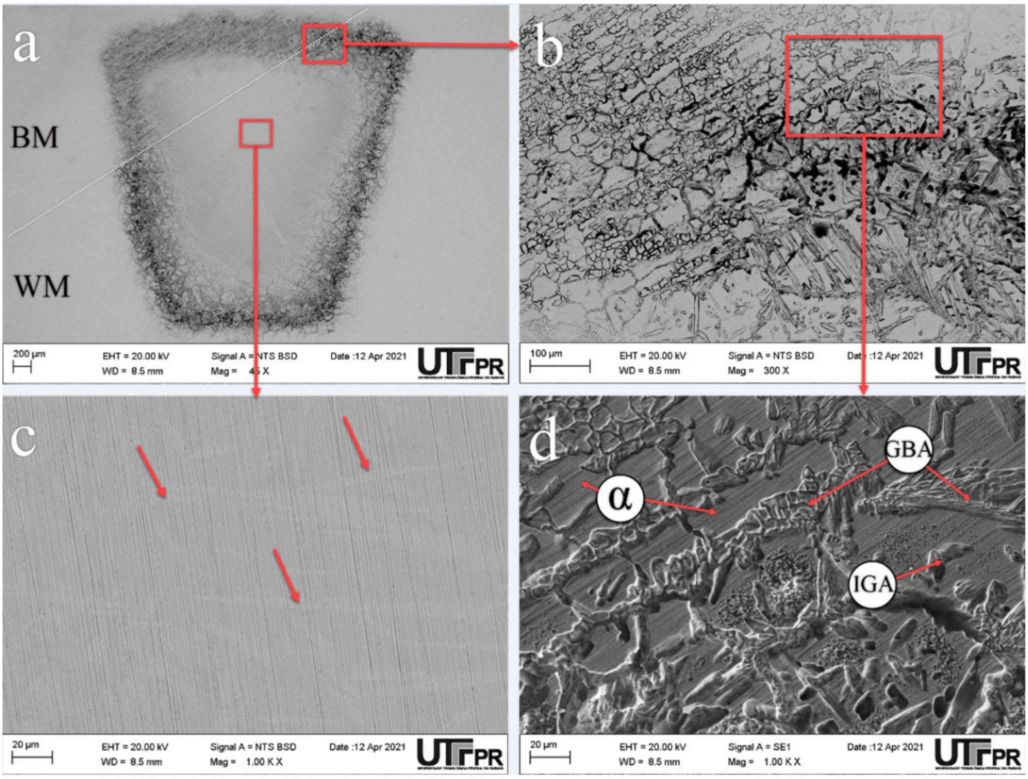

**Figure 12.** a. SEM micrograph (45X) of the crevice attacked site (** in Figure 10b) generated in a BM-WM sample in PD-PS-PD tests in NaCl 3.5% wt. solution, b-d. Magnifications.

the dotted line in Figure 12a. As seen in BM samples, the electrochemical attack revealed the microstructure of the BM-WM samples (Figure 12c). The arrows in Figure 12c indicated the slightly etched austenite morphologies. In addition, pitting did not occur within the crevice former in the WM zone, as shown in Figure 12c. This fact confirms that the GTAW welding conditions carried out on the DSS UNS S32205 did not affect the pitting corrosion resistance of the alloy, as indicated by the cyclic polarization tests Figure 7.

Figure 12 a,b shows that the crevice corrosion occurred in both the base metal and the weld metal. It could be distinguished in Figure 12b that the corrosion was more intense at the crevice mouth and started at grain boundaries ($\alpha/\gamma$), as obtained by Zeng et al.[52] and Yang et al.[50]. Subsequently, as seen in BM samples, the corrosion attack was enlarged to both the outside and the inside of the crevice former boundaries (Figure 12a). Figure 12d and Figure 13 show the preferential dissolution of all morphologies of austenitic phases: grain boundary (GBA), Widmanstätten (WA), and intragranular (IGA). Additionally, notice in Figure 12d and Figure 13 that the regions corresponding to the ferritic phase (matrix) still retain the sanding marks. Zhou et al.[5] confirmed by bipolar electrochemistry tests that a higher susceptibility to transpassive and crevice corrosion occurred in the WM zone of a 2101 lean duplex stainless steel welded using the TIG process. Tests carried out by Zhou et al.[5] did not employ a crevice former, therefore, crevice corrosion did not occur intentionally, it occurred in the interface between the sample and resin. However, according to Zhou et al.[5], higher susceptibility to both types of corrosion was a consequence of the preferential dissolution of secondary austenite in the WM zone, as obtained in this work.

Several studies evaluated the effect of different welding processes on DSS and their consequences to the corrosion resistance by applying electrochemical techniques and solutions containing chlorides[5,14,34-36,42,54]. In general, they reported that the WM and HAZ regions are more susceptible to pitting localized corrosion than the BM, mainly regarding: i) secondary austenite morphologies (IGA, GBA, WA) and deleterious phases, which act as micropits nucleation sites[42,54]; ii) HAZ shows coarser ferrite grains and larger ferrite volume fraction[34]; iii) secondary austenite (IGA, GBA, WA) is more susceptible to corrosion when compared to the primary ferrite and austenite due to its lower Cr, Mo, and N content[14,34,36,42,54]; and iv) change in phase balance (50/50) in WM, and high microstructural heterogeneity[5,34,36]. These four causes were identified for pitting corrosion; however, crevice corrosion is also a type of localized corrosion influenced by the material's microstructural, chemical, and morphological characteristics. In fact, crevice corrosion has not been widely studied in welded duplex stainless steel[5], but in this study, the austenite morphologies (IGA, GBA, WA) in the WM and HAZ regions were heavily and selective corroded compared to the base metal during crevice corrosion (Figure 12, Figure 13).

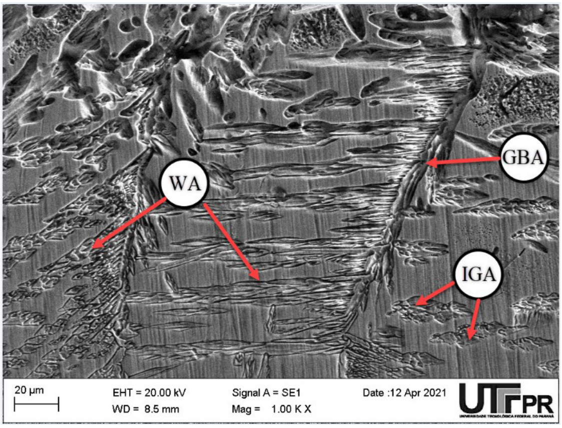

**Figure 13.** SEM micrograph of the preferential attack of secondary austenite in crevice corrosion tests (PD-PS-PD) generated in the weld metal in NaCl 3.5% wt. solution.

The causes previously listed which promote pit nucleation could be related to the characteristics of the welded DSS UNS S32205 in this study, therefore it can be stated: i) a similar elemental chemical distribution was observed between the austenite morphologies and the ferritic matrix in the WM (Table 1); ii) some changes occurred in the phase balance of the HAZ region (Table 2); iii) high microstructural heterogeneity was also observed in both HAZ and WM regions (Figure 4b, c). Consequently, in this study, the microstructural characteristics of the joints favored preferential corrosion of all the austenite morphologies (Figure 12, Figure 13). Therefore, the WM and HAZ regions were more susceptible to crevice corrosion when compared to the base metal region, as confirmed by Zhou et al.[5].

### *3.8. Roughness profile*

Figure 10 shows that the attack was focused on the crevice former boundaries. By investigating the roughness profile, the severity of the crevice corrosion was analyzed based on the depth of the attack in those regions, as presented in Figure 14. Roughness profiles were measured along the dotted line (as seen in Figure 14b) and across it, always aligned with the axes of symmetry of the crevice former slot.

From Figure. 14b, it is clear the difference in crevice corrosion depth at the crevice mouth between the BM and WM regions. Figure 15 presents the depth average values of the base metal samples (BM samples) and welded samples (BM-WM samples). 'BM region' and 'WM region' (Figure 15) represent the corrosion mean depth in the base metal and weld metal regions of BM-WM samples, both measured separately as indicated by the red and blue rectangles, respectively in Figure 14b. The depth mean values and their confidence intervals were analyzed statistically using a student T-test (confidence = 95%).

The corrosion depth of the 'WM region' (Figure 15) was the most severe, with a mean value statistically higher than that outside the weld bead ('BM region' in Figure 15).

The corrosion depth results (Figure 15) suggested that first, the crevice former formed a macroregion where the electrolyte stagnates. Then, such stagnation speeds the electrolyte acidification until the critical solution composition is reached to initiate and propagate the corrosion. Subsequently, the dissolution and metal hydrolysis reactions occur in the most susceptible phases: the austenite morphologies (Figure 13). Finally, the preferential dissolution of the austenite phases in the weld bead generates localized occluded microregions that

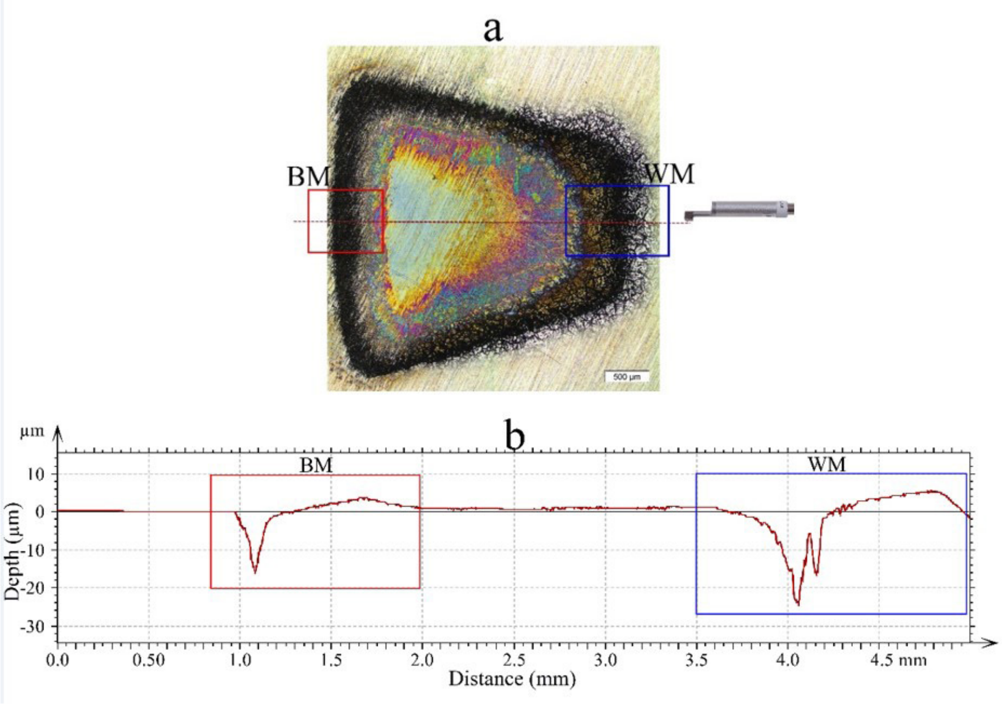

**Figure 14.** a. Optical micrograph of a crevice corrosion attacked site in the transition between the base metal and the weld metal in welded samples. b. 2D roughness profile measured along the dotted line.

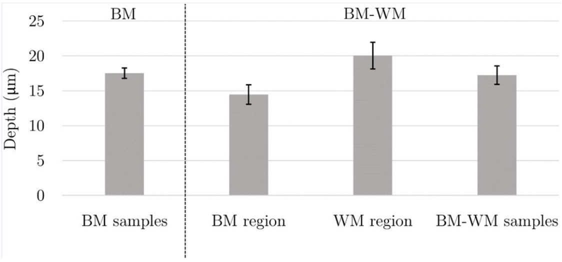

**Figure 15.** Crevice depth measured with 2D roughness equipment in the BM and BM-WM after the crevice tests. 'BM-WM samples' represent the mean depth along the surface, made up of both the base material, HAZ, and WM regions. 'BM region' and 'WM region' represent the corrosion mean depth in the base material and in the weld metal of welded samples measured separately. Error bars indicated de confidence intervals (Student T-test).

intensify the stagnated condition and accelerates the crevice corrosion attack. Consequently, the crevice corrosion in the WM regions satisfies the critical crevice solution mechanism. However, as observed by Palma Calabokis et al.[41] and Zeng, et al.[52], crevice corrosion attacked in duplex stainless steel occurs in the region known as crevice mouth, also indicating the contribution of the local potential drop mechanism (IR drop) inside the crevice.

It seems relevant to mention that crevice corrosion tests carried out in the BM samples showed mean corrosion depths close to those of the welded samples (BM-WM samples) as seen in Figure 15. Although the microstructure inside the weld metal increases the material susceptibility to crevice corrosion, when the welded BM-WM sample (without separating regions) is evaluated, the different behavior between the base metal and welded samples ended up, presenting little statistical relevance regarding both the attack depth and the electrochemical response. In fact, TAPPI TIP 0402-29[45] and Norsok M-601[46] standards set forth that the susceptibility to corrosion must be evaluated in the welded piece without separating the regions. Thus, the DSS UNS S32205 welded using the GTAW process in this study, showed crevice corrosion resistance comparable to the base material.

## 4. Conclusions

The GTAW process of DSS UNS S32205 performed in this study kept the material electrochemical behavior of the base metal. This is a consequence of several aspects such as the proper balance of austenite-ferrite phases along the weld metal, the non-formation of precipitates of deleterious phases, and the proper alloy elemental distribution between the base metal and the weld metal.

The austenite morphologies (IGA, GBA, WA) were the localized crevice corrosion preferential nucleation sites in the HAZ and WM regions, catalyzing its propagation inside and outside the crevice formers. Its differentiated behavior occurs due to changes in the austenite/ferrite phase balance in HAZ and the high microstructural heterogeneity in the weld bead (HAZ and WM).

The pitting and crevice corrosion behavior studied by cyclic polarization tests (CP) and step by step tests (PD-PS-PD) in 3.5% NaCl solution demonstrated that no significant differences were found between the base metal and welded samples. The latter was confirmed when the welded piece was evaluated without distinguishing the regions (BM, HAZ, WM) in accordance with the TAPPI TIP 0402-29 and Norsok M-601 standards.

## 5. Acknowledgments

This work was partially supported by Coordenação de Aperfeiçoamento de Pessoal de Nível Superior (CAPES) for the doctoral sandwich program (PDSE) grant 88881.624474/2021-01. The authors are thankful to the Centro Multiusuário de Caracterização de Materiais (CMCM-UTFPR) for the XRD and SEM-EDS analyses, mainly MSc. Alexandre Gonçalves and PhD Júlio Klein das Neves. P. C. Borges acknowledges CNPq fundings, process 308716/2021-3. The author would also like to acknowledge the special contribution of the company PG CAMPOS for the donation of all materials and the execution of the welding process. The authors also recognize the company ARTIS MATRIZ for the sample grinding.

## 6. References

1. Rodriguez BR, Miranda A, Gonzalez D, Praga R, Hurtado E. Maintenance of the austenite/ferrite ratio balance in GTAW DSS joints through process parameters optimization. Materials (Basel). 2020;13. http://dx.doi.org/10.3390/ma13030780.
2. Selvabharathi R, Muralikannan R. Influence of shot peening and plasma ion nitriding on tensile strength of 2205 duplex stainless steel using A-PAW. Mater Sci Eng A. 2018;709:232-40. http://dx.doi.org/10.1016/j.msea.2017.10.068.
3. Rodríguez BR, Miranda AF, Hurtado E. Microestructural de la unión disímil de acero inoxidable lean dúplex 2304 y acero inoxidable súper dúplex 2507 soldados mediante el proceso GTAW. In: Congreso 2017 Ingenieria Mecanica/Ciencia E I Ngeniería de Materiales; Septiembre 2017; Querétaro, México. Proceedings. 2017 [cited 2022 Apr 1]. Available from: http://comimsa.repositorioinstitucional.mx/jspui/handle/1022/160
4. Núñez de la Rosa YE, Palma Calabokis O, Borges PC, Ballesteros Ballesteros V. Effect of low-temperature plasma nitriding on corrosion and surface properties of duplex stainless steel UNS S32205. J Mater Eng Perform. 2020;29:2612-22. http://dx.doi.org/10.1007/s11665-020-04753-6.
5. Zhou Y, Kablan A, Engelberg DL. Metallographic screening of duplex stainless steel weld microstructure with a bipolar electrochemistry technique. Mater Charact. 2020;169:110605. http://dx.doi.org/10.1016/j.matchar.2020.110605.
6. Mohammed GR, Ishak M, Aqida SN, Abdulhadi HA. Effects of heat input on microstructure, corrosion and mechanical characteristics of welded austenitic and duplex stainless steels: a review. Metals (Basel). 2017;7. http://dx.doi.org/10.3390/met7020039.
7. Paulraj P, Garg R. Effect of intermetallic phases on corrosion behavior and mechanical properties of duplex stainless steel and super-duplex stainless steel. Adv Sci Technol Res J. 2015;9:87-105. http://dx.doi.org/10.12913/22998624/59090.
8. Badji R, Bacroix B, Bouabdallah M. Texture, microstructure and anisotropic properties in annealed 2205 duplex stainless steel welds. Mater Charact. 2011;62:833-43. http://dx.doi.org/10.1016/j.matchar.2011.06.001.
9. Azzi M, Klemberg-Sapieha J. Tribocorrosion test protocols for sliding contacts. In: Landolt D, Mischler S, editors. Tribocorrosion of passive metals and coatings. Cambridge: Woodhead Pub; 2011. p. 222-38. https://doi.org/10.1533/9780857093738.2.222.
10. Sim BM, Hong TS, Hanim MAA, Tchan EJN, Talari MK. The influence of post weld heat treatment precipitation on duplex stainless steels weld overlay towards pitting corrosion. Materials (Basel). 2019;12. http://dx.doi.org/10.3390/ma12203285.
11. Singh AK, Singh G. Corrosion of stainless steels in chlorine dioxide solution. Anti-Corros Methods Mater. 2002;49:417-25. http://dx.doi.org/10.1108/00035590210452761.
12. Núñez Y, Mafra M, Morales RE, Borges PC, Pintaude G. The effect of plasma nitriding on the synergism between wear and corrosion of SAF 2205 duplex stainless steel. Ind Lubr Tribol. 2020;9:1117-22. http://dx.doi.org/10.1108/ILT-08-2019-0302.
13. Elsaady MA, Khalifa W, Nabil MA, El-Mahallawi IS. Effect of prolonged temperature exposure on pitting corrosion of duplex stainless steel weld joints. Ain Shams Eng J. 2018;9:1407-15. http://dx.doi.org/10.1016/j.asej.2016.09.001.
14. Luchtenberg P, Tancredo P, Campos D, Soares P, Augusto C, Laurindo H et al. Effect of welding energy on the corrosion and tribological properties of duplex stainless steel weld overlay deposited by GMAW/CMT process. Surf Coat Tech. 2019;375:688-93. http://dx.doi.org/10.1016/j.surfcoat.2019.07.072.
15. Badji R, Bouabdallah M, Bacroix B, Kahloun C, Belkessa B, Maza H. Phase transformation and mechanical behavior in annealed 2205 duplex stainless steel welds. Mater Charact. 2008;59:447-53. http://dx.doi.org/10.1016/j.matchar.2007.03.004.
16. Gnanasundaram BR, Natarajan M. Influences of the heat input on a 2205 duplex stainless steel weld. Mater Tehnol. 2014;48:761-3.
17. Zappa S, Zalazar M, Surian E. Efecto de la composición química del metal de aporte y del calor aportado sobre la microestructura y las propiedades mecánicas de juntas soldadas de aceros inoxidables dúplex. Soldag Insp. 2017;22:116-28. http://dx.doi.org/10.1590/0104-9224/SI2202.02.
18. Luo J, Yuan Y, Wang X, Yao Z. Double-sided single-pass submerged arc welding for 2205 duplex stainless steel. J Mater Eng Perform. 2013;22:2477-86. http://dx.doi.org/10.1007/s11665-013-0529-8.
19. Aguiar IV, Escobar DP, Santos DB, Modenesi PJ. Microstructure characterization of a duplex stainless steel weld by electron backscattering diffraction and orientation imaging microscopy techniques. Rev Mat. 2015;20:212-26. http://dx.doi.org/10.1590/S1517-707620150001.0022.
20. Geng S, Sun J, Guo L, Wang H. Evolution of microstructure and corrosion behavior in 2205 duplex stainless steel GTA-welding joint. J Manuf Process. 2015;19:32-7. http://dx.doi.org/10.1016/j.jmapro.2015.03.009.
21. Heider B, Oechsner M, Reisgen U, Ellermeier J, Engler T, Andersohn G et al. Corrosion resistance and microstructure of welded duplex stainless steel surface layers on gray cast iron. J Therm Spray Technol. 2020;29:825-42. http://dx.doi.org/10.1007/s11666-020-01003-y.
22. Tahaei A, Perez AFM, Merlin M, Valdes FAR, Garagnani GL. Effect of the addition of nickel powder and post weld heat treatment on the metallurgical and mechanical properties of the welded UNS S32304 duplex stainless steel. Soldag Insp. 2016;21:197-208. http://dx.doi.org/10.1590/0104-9224/si2102.09.
23. Fonseca CS, Pinheiro IP, Silva SN. Influência do aporte térmico sobre a morfologia da austenita e na quantidade das fases em chapas soldadas de aço inoxidável duplex SAF2205. Materia (Rio J). 2016;21(1):227-34. http://dx.doi.org/10.1590/S1517-707620160001.0020.
24. Roldão AMB. Estudo do efeito do aporte térmico nas propriedades macânicas e microestruturais do aço inoxidável duplex UNS S 31803 em chapa grossa, soldado pelo processo GMAW [thesis]. Belo Horizonte: Universidade Federal de Minas Gerais; 2010.
25. Videira AME. Influência do aporte térmico da soldagem GTAW no balanço de fases ferrita/austenita do aço inoxidável duplex UNS S32205 [dissertation]. Ilha Solteira: Universidade Estadual Paulista; 2016.

26. Nascimento AM, Ierardi MCF, Kina AY, Tavares SSM. Pitting corrosion resistance of cast duplex stainless steels in 3.5%NaCl solution. Mater Charact. 2008;59:1736-40. http://dx.doi.org/10.1016/j.matchar.2008.03.015.
27. Eghlimi A, Shamanian M, Raeissi K. Effect of current type on microstructure and corrosion resistance of super duplex stainless steel claddings produced by the gas tungsten arc welding process. Surf Coat Tech. 2014;244:45-51. http://dx.doi.org/10.1016/j.surfcoat.2014.01.047.
28. Kotecki DJ. Some pitfalls in welding of duplex stainless steels. Soldag Insp. 2010;15:336-43. http://dx.doi.org/10.1590/s0104-92242010000400011.
29. Yousefieh M, Shamanian M, Saatchi A. Influence of heat input in pulsed current GTAW process on microstructure and corrosion resistance of duplex stainless steel welds. J Iron Steel Res Int. 2011;18(9):65-9. http://dx.doi.org/10.1016/S1006-706X(12)60036-3.
30. Moura VS, Lima LD, Pardal JM, Kina AY, Corte RRA, Tavares SSM. Influence of microstructure on the corrosion resistance of the duplex stainless steel UNS S31803. Mater Charact. 2008;59:1127-32. http://dx.doi.org/10.1016/j.matchar.2007.09.002.
31. Vahman M, Shamanian M, Golozar MA, Jalali A, Sarmadi MA, Kangazian J. The effect of welding heat input on the structure–property relationship of a new grade super duplex stainless steel. Steel Res Int. 2020;91:1-12. http://dx.doi.org/10.1002/srin.201900347.
32. Pereira PAS. Efeito da energia de soldagem na microestrutura de um aço inoxidável duplex e super duplex [dissertation]. Campo dos Goytacazes: Universidade Estadual do Norte Fluminense Darcy Ribeiro; 2009.
33. Heider B, Oechsner M, Reisgen U, Ellermeier J, Engler T, Andersohn G et al. Corrosion resistance and microstructure of welded duplex stainless steel surface layers on gray cast iron. J. Therm. Spray Technol. 2020;29:825-42. http://dx.doi.org/10.1007/s11666-020-01003-y.
34. Geng S, Sun J, Guo L, Wang H. Evolution of microstructure and corrosion behavior in 2205 duplex stainless steel GTA-welding joint. J Manuf Process. 2015;19:32-7. http://dx.doi.org/10.1016/j.jmapro.2015.03.009.
35. Eghlimi A, Raeissi K, Shamanian M. Tribocorrosion behavior of overlay welded super duplex stainless steel in chloride medium. J Bio- Tribo-Corros. 2015;1(3):1-15. http://dx.doi.org/10.1007/s40735-015-0018-8.
36. Shin BH, Park S, Park J, Kim D, Hwang M, Chung W. Effect of post-weld heat treatment on the corrosion behavior of resistance spot welded super duplex stainless UNS S 32750. Int J Electrochem Sci. 2019;14:2430-41. http://dx.doi.org/10.20964/2019.03.14.
37. Pettersson R, Westin EM, Johansson M. Corrosion performance of welds in duplex, superduplex and lean duplex stainless steels. In: NACE CORROSION 2013. Proceedings. Texas: OnePetro; 2013.
38. Zhang Z, Jing H, Xu L, Han Y, Zhao L. The influence of microstructural evolution on selective corrosion in duplex stainless steel flux-cored arc welded joints. Corros Sci. 2017;120:194-210. http://dx.doi.org/10.1016/j.corsci.2016.12.007.
39. Palma Calabokis O. Corrosão localizada do aço duplex UNS S32750 nitretado por plasma em baixas temperaturas [dissertation]. Curitiba: Universidade Tecnologica Federal do Paraná; 2020.
40. Videira AM. Influência do aporte térmico da soldagem GTAW no balanço de fases ferrita/austenita do aço inoxidável duplex UNS S32205 [dissertation]. Ilha Solteira: Universidade Estadual Paulista; 2016.
41. Palma Calabokis O, Núñez de la Rosa Y, Lepienski CM, Perito Cardoso R, Borges PC. Crevice and pitting corrosion of low temperature plasma nitrided UNS S32750 super duplex stainless steel. Surf Coat Tech. 2021;413:17-20. http://dx.doi.org/10.1016/j.surfcoat.2021.127095.
42. Zhang Z, Wang Z, Jiang Y, Tan H, Han D, Guo Y et al. Effect of post-weld heat treatment on microstructure evolution and pitting corrosion behavior of UNS S31803 duplex stainless steel welds. Corros Sci. 2012;62:42-50. http://dx.doi.org/10.1016/j.corsci.2012.04.047.
43. Zhang Y, Cheng F, Wu S. Improvement of pitting corrosion resistance of wire arc additive manufactured duplex stainless steel through post-manufacturing heat-treatment. Mater Charact. 2021;171:110743. http://dx.doi.org/10.1016/j.matchar.2020.110743.
44. Singh J, Shahi AS. Electrochemical corrosion behavior and microstructural characteristics of electron beam welded UNS S32205 duplex stainless steel. Mater Corros – Werkst Korros. 2021;72(8):1350-69. http://dx.doi.org/10.1002/maco.202012201.
45. TAPPI. TIP 0402-29: Qualification of welding procedures for duplex stainless steels. Georgia: TAPPI; 2001).
46. Norsok Standard. M-601, Welding and inspection of piping©. Norway: Standards Norway; 2016.
47. Moteshakker A, Danaee I. Microstructure and corrosion resistance of dissimilar weld-joints between duplex stainless steel 2205 and austenitic stainless steel 316L. J Mater Sci Technol. 2016;32:282-90. http://dx.doi.org/10.1016/j.jmst.2015.11.021.
48. Tavares SSM, Pardal JM, Noris LF, Diniz MG. Microstructural characterization and non-destructive testing and of welded joints of duplex stainless steel in flexible pipes. J Mater Res Technol. 2021;15:3399-408. http://dx.doi.org/10.1016/j.jmrt.2021.09.087.
49. Han D, Jiang Y, Deng B, Zhang L, Gao J, Tan H et al. Detecting critical crevice temperature for duplex stainless steels in chloride solutions. Corrosion. 2011;67(2):0250041-7. http://dx.doi.org/10.5006/1.3552290.
50. Yang YZ, Jiang YM, Li J. In situ investigation of crevice corrosion on UNS S32101 duplex stainless steel in sodium chloride solution. Corros Sci. 2013;76:163-9. http://dx.doi.org/10.1016/j.corsci.2013.06.039.
51. Betts AJ, Boulton LH. Crevice corrosion: review of mechanisms, modelling, and mitigation. Br Corros J. 1993;28:279-96. http://dx.doi.org/10.1179/000705993799156299.
52. Zeng H, Yang Y, Liu L, Li M. Pitting and crevice corrosion evolution characteristics of 2205 duplex stainless steel in hot concentrated seawater. J Solid State Electrochem. 2021;25(5):1555-65. http://dx.doi.org/10.1007/s10008-021-04935-9.
53. Torres C, Johnsen R, Iannuzzi M. Crevice corrosion of solution annealed 25Cr duplex stainless steels: effect of W on critical temperatures. Corros Sci. 2021;171:1-14. http://dx.doi.org/10.1016/j.corsci.2020.109053.
54. Zhiqiang Z, Jing H, Xu L, Han Y, Zhao L. The influence of microstructural evolution on selective corrosion in duplex stainless steel flux-cored arc welded joints. Corros Sci. 2017;120:194-210. http://dx.doi.org/10.1016/j.corsci.2016.12.007.

# 8 CONCLUSÕES

A nitretação a plasma em 380 °C promoveu a formação de uma fina camada uniforme e bem destacada de austenita expandida sem presença de nitretos, com espessura em torno de 3,5 µm e dureza de até três vezes a dureza do substrato. Estes resultados são consequência da difusividade do nitrogênio e à formação da fase austenita expandidas.

A NPBT usada nesta pesquisa, melhorou significativamente a resistência a corrosão, evidenciadas pela taxa de corrosão generalizada, aumento do potencial de corrosão, diminuição da densidade de corrente e aumento do potencial de pites.

As condições de nitretação empregadas neste trabalho promoveram melhoras no desempenho frente ao desgaste abrasivo puro e tribocorrosivo (abrasão-corrosão) comparado com o aço não tratado devido a capacidade de repassivação e dureza da capa protetora.

Os parâmetros empregados no processo de solda GTAW no AID UNS S32205 mantiveram o comportamento eletroquímico do metal base. Isto baseados nos resultados dos ensaios de polarização cíclica e potenciostáticos em solução de NaCl 3,5 % que mostraram que não houve diferenças significativas nos potenciais de corrosão, pites e fresta entre o metal base e as amostras soldadas.

O bom comportamento frente a corrosão localizada do AID soldado foram consequência de vários aspectos, tais como um equilíbrio adequado das fases austenita-ferrita ao longo do metal de solda, a não formação de precipitados de fases deletérias e a distribuição adequada dos elementos de liga entre o metal base e o metal de solda.

Ambos os processos empregados (nitretação e solda) no AID UNS S32205 geraram mudanças tanto microestruturais como de composição sem comprometer a resistência a corrosão em meios contendo cloretos.

# SUGESTÕES

Efetuar o tratamento de nitretação por plasma desenvolvido nos dois primeiros artigos, em juntas de solda pelo processo TIG do aço inoxidável duplex UNS S32205 e avaliar a viabilidade de realizar este tratamento de nitretação como processo posterior à soldagem e o processo inveso (soldar o aço nitretado).

Realizar as devidas caracterizações de dureza, mudanças microestruturais, morfologias das fases, e avaliar o comportamento frente a corrosão localizada por pites e fresta.

Avaliar a temperatura crítica de pites e fresta em soluções contendo cloretos (NaCl e $FeCl_3$) do aço inoxidável duplex UNS S32205 e sua solda (pelo processo TIG), ambos nitretados por plasma.

Estudar o efeito sinérgico de erosão-corrosão e cavitação-corrosão do aço do inoxidável duplex UNS S32205, sua solda e condições nitretadas, em soluções contendo cloretos (NaCl e $FeCl_3$).

# REFERÊNCIAS

AGUILAR-SIERRA, S. M.; SERNA GIRALDO, C. P.; ARISTIZÁBAL-SIERRA, R. E. Transformaciones microestructurales en soldaduras disímiles de acero inoxidable austenítico con acero inoxidable ferrítico. **Soldagem e Inspeção**, v. 20, n. 1, p. 59–67, 2015.

AHAMAD, N. W.; JAUHARI, I. Carburizing of duplex stainless steel (DSS) under compression superplastic deformation. **Metallurgical and Materials Transactions A: Physical Metallurgy and Materials Science**, v. 43, n. 13, p. 5115–5121, dez. 2012.

ALPHONSA, J.; RAJA, V. S.; MUKHERJEE, S. Study of plasma nitriding and nitrocarburizing for higher corrosion resistance and hardness of 2205 duplex stainless steel. **Corrosion Science**, v. 100, p. 121–132, 1 nov. 2015.

ALVES JUNIOR, C. **Nitretação a plasma: Fundamentos e Aplicações**. Natal: Universidade Federal do Rio Grande do Norte, 2001.

BORGES, F. M. R. et al. Plasma nitriding of welded joint of the SAF 2507 super duplex stainless steel. **Revista Materia**, v. 24, n. 1, 2019.

BRINKE, T. AUF DEM., C. JURGEN., H. R. O. W. Plasma-assisted surface treatment: nitriding, nitrocarburizing and oxidation of steel, cast iron and sinterd materials = **Plasmagestützte Oberflächenbehandlung <engl.>**. Verl. Moderne Industrie, 2006.

CALABOKIS, O. P. **Corrosão localizada do aço duplex UNS S32750 nitretado por plasma em baixas temperaturas**. Curitiba: Universidade Tecnológica Federal do Paraná, 2020.

CARDOSO, P.; MAFRA, M.; BRUNATTO, S. Low-temperature thermochemical treatments of stainless Steels – An Introduction. Em: **Plasma Science and Technology - Progress in Physical States and Chemical Reactions**. InTech, 2016. p. 1–24.

DAN, N. E. et al. Improved surface morphology and corrosion resistance performance of 2205 duplex stainless steel by low temperature gas nitriding. **Journal of Bio- and Tribo-Corrosion**, v. 8, n. 4, 1 dez. 2022.

DAVIDSON, K. P.; SINGAMNENI, S. The mechanics of machining selective laser melted super duplex stainless steels. **Journal of Materials Research and Technology**, v. 17, p. 601–611, 1 mar. 2022.

DE SOUZA PEREIRA, P. A. **Efeito da energia de soldagem na microestrutura deum aço inoxidável duplex e super duplex**. Dissertação—Campos dos Goytacazes: Universidade Estadual do Norte Fluminense Darcy Ribeiro, jun. 2009.

EGHLIMI, A.; RAEISSI, K.; SHAMANIAN, M. Tribocorrosion behavior of overlay welded super duplex stainless steel in chloride medium. **Journal of Bio- and Tribo-Corrosion**, v. 1, n. 3, 1 set. 2015.

EGHLIMI, A.; SHAMANIAN, M.; RAEISSI, K. Effect of current type on microstructure and corrosion resistance of super duplex stainless steel claddings produced by the gas tungsten arc welding process. **Surface and Coatings Technology**, v. 244, p. 45–51, 15 abr. 2014.

ELSAADY, M. A. et al. Effect of prolonged temperature exposure on pitting corrosion of duplex stainless steel weld joints. **Ain Shams Engineering Journal**, v. 9, n. 4, p. 1407–1415, 1 dez. 2018.

FONSECA, C. S.; PINHEIRO, I. P.; DA SILVA, S. N. Influência do aporte térmico sobre a morfologia da austenita e na quantidade das fases em chapas soldadas de aço inoxidável duplex SAF2205. **Revista Materia**, v. 21, n. 1, p. 227–234, 1 jan. 2016.

FREITAS, G. C. L. D. et al. Phase transformations of the duplex stainless steel UNS S31803 under non-isothermal conditions. **Journal of Materials Research and Technology**, v. 11, p. 1847–1851, 1 mar. 2021.

GENG, S. et al. Evolution of microstructure and corrosion behavior in 2205 duplex stainless steel GTA-welding joint. **Journal of Manufacturing Processes**, v. 19, p. 32–37, 2015.

GHOLAMI, M.; HOSEINPOOR, M.; MOAYED, M. H. A statistical study on the effect of annealing temperature on pitting corrosion resistance of 2205 duplex stainless steel. **Corrosion Science**, v. 94, p. 156–164, 1 maio 2015.

GNANASUNDARAM, B. R.; NATARAJAN, M. Influences of the heat input on a 2205 duplex stainless steel weld. **Materiali in tehnologije**, v. 48, n. 5, p. 761–763, 2014.

HARUMAN, E.; SUN, Y.; ADENAN, M. S. A comparative study of the tribocorrosion behaviour of low temperature nitrided austenitic and duplex stainless steels in NaCl solution. **Tribology International**, v. 151, 1 nov. 2020.

HEIDER, B. et al. Corrosion Resistance and Microstructure of Welded Duplex Stainless Steel Surface Layers on Gray Cast Iron. **Journal of Thermal Spray Technology**, v. 29, n. 4, p. 825–842, 1 abr. 2020.

KOTECKI, D. J. Some pitfalls in welding of duplex stainless steels (Algumas armadilhas na soldagem de aços inoxidáveis duplex). **Soldagem e Inspeção**, v. 15, n. 4, p. 336–343, 2010.

LEITE, A. M. D. S. et al. On the pitting resistance of friction stir welded UNS S82441 lean duplex stainless steel. **Journal of Materials Research and Technology**, v. 8, n. 3, p. 3223–3233, 1 maio 2019.

LIANG, X. Z. et al. Hydrogen embrittlement in super duplex stainless steels. **Materialia**, v. 9, 1 mar. 2020.

LUCHTENBERG PAOLA et al. Effect of welding energy on the corrosion and tribological properties of duplex stainless steel weld overlay deposited by GMAW/CMT process. **Surface and Coatings Technology**, v. 375, p. 688–693, 15 out. 2019.

LUO, J. et al. Double-sided single-pass submerged arc welding for 2205 duplex stainless steel. **Journal of Materials Engineering and Performance**, v. 22, n. 9, p. 2477–2486, 1 set. 2013.

MARCOS BORBA ROLDÃO ORIENTADOR, A.; ALEXANDRE QUEIROZ BRACARENSE, P.; HORIZONTE, B. **Estudo do efeito do aporte térmico nas propriedades mecânicas e microestruturais do aço inoxidável duplex UNS S31803 em chapa grossa, soldado pelo processo GMAW**. Dissertação—Belo Horizonte: Universidade Federal de Minas Gerais, maio 2010.

MOHAMMED, G. R. et al. Effects of heat input on microstructure, corrosion and mechanical characteristics of welded austenitic and duplex stainless steels: A review. **Metals**, v. 7, n. 2, p. 1–18, 1 fev. 2017.

MORAES E VIDEIRA, A. **Influência do aporte térmico da soldagem GTAW no balanço de fases ferrita/austenita do aço inoxidável duplex UNS S32205**. Ilha Solteira: Universidade Estadual Paulista, 2016.

MÚÑEZ, C., et al. Influencia del material de aporte en la resistencia a corrosión por picadura en uniones soldadas de un acero inoxidable dúplex 2205. p. 1–8, 2007.

MÚÑEZ, C. J., et al. Influencia del material de aporte en la resistencia a corrosión por picaduras en uniones soldadas de un acero dúplex 2205. p. 1–8, 2007.

NORSOK STANDARD M-601:2016. **Welding and inspection of piping**. Disponível em: <www.standard.no/petroleum>, 2016.

PALMA CALABOKIS, O. et al. Crevice and pitting corrosion of low temperature plasma nitrided UNS S32750 super duplex stainless steel. **Surface and Coatings Technology**, v. 413, 15 maio 2021.

PARDAL, J. M. et al. Caracterização e Avaliação da Resistência à Corrosão na Soldagem de Tubulação de Aço Inoxidável Duplex UNS S31803 pelo Processo a Arco Submerso. **Soldagem e Inspeção**, v. 16, n. 4, p. 310–321, 2011.

PATRICK DE LEÃO, A. et al. **Análise dos sistemas de risers utilizados na produção de óleo em sistemas submarinos**. Ciências exatas e tecnológicas. **Anais**, 2014.

PAULRAJ, P.; GARG, R. Effect of intermetallic phases on corrosion behavior and mechanical properties of duplex stainless steel and super-duplex stainless steel. **Advances in Science and Technology Research Journal**, v. 9, p. 87–105, 2015.

PEDRALI, P. C. **Nitretação à baixa temperatura assistida por plasma do aço inoxidável duplex UNS S32101: influência da deformação plástica**. Curitiba: Universidade Federal do Paraná, 2012.

PEZZATO, L.; CALLIARI, I. Advances in Duplex Stainless Steels. **Materials**, v. 15, n. 20, p. 1–3, 1 out. 2022.

PINEDO, C. E.; VARELA, L. B.; TSCHIPTSCHIN, A. P. Low-temperature plasma nitriding of AISI F51 duplex stainless steel. **Surface and Coatings Technology**, v. 232, p. 839–843, 15 out. 2013.

PINTAUDE, G. et al. Wear and Corrosion Resistances of Active Screen Plasma-Nitrided Duplex Stainless Steels. **Journal of Materials Engineering and Performance**, v. 28, n. 6, p. 3673–3682, 15 jun. 2019.

RENÓ GRILO, T. et al. Análise microestrutural de um aço inoxidável duplex UNS S32304 submetido ao processo de soldagem GMAW. p. 1–9, 2016.

RODRIGUEZ, B. R. et al. Maintenance of the austenite/ferrite ratio balance in GTAW DSS joints through process parameters optimization. **Materials**, v. 13, n. 3, p. 1–14, 1 fev. 2020.

SATYAPAL, M., A. S. K. A. J. Effect of Temperature on the Plasma Nitriding of Duplex Stainless Steels. **International Journal of Engineering and Innovative Technology (IJEIT)**, v. 2, n. 11, p. 1–6, 2013.

SATYAPAL.M; A.S. KHANNA AND ALPHONSA JOSEPH. Effect of Temperature on the Plasma Nitriding of Duplex Stainless Steels. p. 1–7, 2013.

SELVABHARATHI, R.; MURALIKANNAN, R. Influence of shot peening and plasma ion nitriding on tensile strength of 2205 duplex stainless steel using A-PAW. **Materials Science and Engineering: A**, v. 709, p. 232–240, 2 jan. 2018.

SHEN, H.; WANG, L.; SUN, J. Effect of plasma nitriding at low temperature on the corrosion resistance and conductivity of 2205 duplex stainless steel. **Surface Engineering**, p. 1–6, 2020.

SHIN, B. H. et al. Effect of post-weld heat treatment on the corrosion behavior of resistance spot welded super duplex stainless UNS S 32750. **International Journal of Electrochemical Science**, v. 14, n. 3, p. 2430–2441, 2019.

SIM, B. M. et al. The influence of post weld heat treatment precipitation on duplex stainless steels weld overlay towards pitting corrosion. **Materials**, v. 12, n. 20, p. 1–11, 1 out. 2019.

SINGH, A. K.; SINGH, G. Corrosion of stainless steels in chlorine dioxide solution. **Anti-Corrosion Methods and Materials**, v. 49, n. 6, p. 417–425, 2002.

SUBBIAH, R.; VINOD KUMAR, V.; LAKSHMI PRASANNA, G. wear analysis of treated duplex stainless steel material by carburizing process - A review**. Materials Today**: Proceedings. **Anais**. Elsevier Ltd, 2019.

TAHAEI, A. et al. Efeito da adição de pó de níquel e do tratamento pós soldagem nas propriedades metalúrgicas do aço inoxidável duplex UNS S32304 soldado. **Soldagem e Inspeção**, v. 21, n. 2, p. 197–208, 1 abr. 2016.

TAPPI. **Qualification of welding procedures for duplex stainless steels - TIP 0402-29, TAPPI.**, 2001.

VERMA, J.; TAIWADE, R. V. Effect of welding processes and conditions on the microstructure, mechanical properties and corrosion resistance of duplex stainless steel weldments—A review. **Journal of Manufacturing Processes** Elsevier Ltd, 1 jan. 2017.

YAN, J. et al. Microstructure and properties of SAE 2205 stainless steel after salt bath nitrocarburizing at 450 °c. **Journal of Materials Engineering and Performance**, v. 23, n. 4, p. 1157–1164, 1 abr. 2014.

YOUSEFIEH, M.; SHAMANIAN, M.; SAATCHI, A. Influence of heat input in pulsed current GTAW process on microstructure and corrosion resistance of duplex stainless steel welds. **Journal of iron and steel research, international**, v. 18, p. 65–69, 2011.

ZAPPA, S. et al. Corrosion characterization in superduplex stainless steel cladding. **Revista Materia**, v. 23, n. 2, 2018.

ZAPPA, S.; ZALAZAR, M.; SURIAN, E. Efecto de la composición química del metal de aporte y del calor aportado sobre la microestructura y las propiedades mecánicas de juntas soldadas de aceros inoxidables dúplex. **Soldagem e Inspeção**, v. 22, n. 2, p. 116–128, 2017.

ZHANG, Z. et al. Influence of microstructure and elemental partitioning on pitting corrosion resistance of duplex stainless steel welding joints. **Applied Surface Science**, v. 394, p. 297–314, 1 fev. 2017.

## APENDICE A

### Artigos publicados no doutorado

**Lubricants** Qualis Capes: **A1** Scimago: **Q2**

Effect of a metal conditioner on the physicochemical properties and tribological performance of the engine oil SAE 5W-30 API SN

*O. P. Calabokis, **Y. Nuñez de la Rosa**, V. Ballesteros-Ballesteros, P. C. Borges e T. Cousseau*

DOI: doi.org/10.3390/lubricants11070305

**Materials** Qualis Capes: **A1** Scimago: **Q2**

Strength, Stiffness, and Microstructure of Stabilized Marine Clay-Crushed Limestone Waste Blends: Insight on Characterization Through Porosity-to-Cement Index

*Carlos Román Martínez, **Yamid E. Núñez de la Rosa**, Daniela Estrada Luna, Jair Arrieta Baldovino and Giovani Jordi Bruschi*

DOI: doi.org/10.3390/ma16144983

**Metals** Qualis Capes: **A1** Scimago: **Q1**

Assessment of pitting and crevice corrosion and mechanical properties of low- temperature plasma nitrided Inconel alloy 718

***Y. Nuñez de la Rosa**, O. P. Calabokis, V. Ballesteros-Ballesteros, C. Lozano Tafur e P. C. Borges*

DOI: doi.org/10.3390/met13071172

**Metals** Qualis Capes: **A1** Scimago: **Q1**

Mechanical characterization of austenite, ferrite and sigma phases of duplex stainless steel using hardness and fretting techniques at nanoscale

*Jomar José Knaip Ribeiro, Alba Regina Turin, **Yamid E. Nuñez de la Rosa**, Pedro Victorio Caetano Abrantes Quadros, Oriana Palma Calabokis,Carlos Maurício Lepienski, Silvio Francisco Brunatto e Paulo César Borges*

DOI: doi.org/ 10.3390/met13050864

**Polymers** Qualis Capes: **A1** Scimago: **Q1**

Electrochemistry study of bio based composite Biopolymer electrolyte starch/cardol

*Alvaro A. Arrieta, **Yamid Nuñez de la Rosa**, e Manuel Palencia*

DOI: doi:10.3390/polym15091994

**Surface Topography: Metrology and Properties** Qualis Capes: **A3** Scimago: **Q2**

Experimental and numerical study of contact fatigue for 18CrNiMo7-6 and 20MnCr5 carburized gear tooth

*Oriana Palma Calabokis, **Yamid Enrique Núñez de la Rosa**, Samara Paulin de Moraes, Estela Vicentim Antunes, Tiago Cousseau e Carlos Henrique da Silva*

DOI: doi.org/10.1088/2051-672X/ac939f

**Lubricants** Qualis Capes: **A4** Scimago: **Q2**

Effect of an aftermarket additive in powertrain wear and fuel consumption of small-capacity motorcycles: a lab and field study

*Oriana Palma Calabokis, **Yamid Nuñez de la Rosa**, Paulo César Borges e Tiago Cousseau*

DOI: doi.org/10.3390/lubricants10070143

**Surface Topography: Metrology and Properties** Qualis Capes: **A3** Scimago: **Q2**

Tribological Behavior of Cellulose Nanostructured Films

*Carmen Fuenmayor, Dimas A da Silva1, Umberto Klock, Elaine C Lengowski, Alan S de Andrade, Eraldo A Bonfatti, Jhonattan Trejo, **Yamid Nuñez**, Oriana Palma, Pedro Henrique G de Cademartori e Graciela Ines B de Muniz*

DOI: doi.org/10.1088/2051-672X/ac7fab

**Revista de Chimie** Qualis Capes: **B1** Scimago: N/A

Nanocomposite Poly(lactic acid)/sepiolite with Improved Mechanical and Biofilms Formation Properties

*Oriana Palma Calabokis, Rosestela Perera, Carmen Rosales,* ***Yamid Nuñez,*** *Jairo Segura, Alvaro Arrieta*
DOI: doi.org/10.37358/RC.22.1.8501

**Surface and coatings technology** Qualis Capes: **A1** Scimago: **Q1**
Crevice and pitting corrosion of low temperature plasma nitrided UNS S32750 super duplex stainless steel
*Oriana Palma Calabokis,* ***Yamid Núñez de la Rosa****, Carlos M. Lepienski, Rodrigo Perito Cardoso, Paulo César Borges*
DOI: doi.org/10.1016/j.surfcoat.2021.127095

**Mechanics of Materials** Qualis Capes: **A1** Scimago: **Q1**
Comparative study of the main properties associated with thin layers of coatings with the cobalt-chromium-tungsten alloy (stellite) and hard chromium plating used as reinforcements for wood sawing
*Jhonattan Trejo, Ramón Tolosa, Néstor Ruiz, Pablo Ninin, Carmen Fuenmayor, Marcos Zambrano, Oriana Palma,* ***Yamid Nuñez***
DOI: doi:10.1016/j.mechmat.2020.103637

**International Journal of Technology** Qualis Capes: N/A Scimago: **Q2**
Mini-electronic tongue used to discriminate between coffee samples of different geographical origin
*A.A. Arrieta,* ***Y.E. Nuñez*** *e J.M. Mendoza*
DOI: doi:10.14716/ijtech.v11i2.3225

## Artigos submetidos atualmente

**Sustainability** Qualis Capes: **A1** Scimago: **Q1**
Insight on Characterization Through Porosity-to-Lime Index of a Stabilized Soil for the Long-Term
***Yamid E. Núñez de la Rosa,*** *Jair Arrieta Baldovino and Oriana Palma Calabokis*
DOI: *Revised version review*

## Artigo publicado em congresso

Congresso: **SIMEA 2022**
Effect of using a metal conditioner in performance, fuel consumption, and powertrain wear of new small-capacity motorcycles
*Oriana Palma Calabokis,* ***Yamid E. Nuñez de la Rosa,*** *Paulo César Borges e Tiago Cousseau*
DOI: doi.10.5151/simea2022-PAP26

Congresso: **COBEF 2019**
Avaliação da nitretação a plasma em baixas temperaturas na resistência à corrosão do aço inoxidável duplex UNS S32205
*Oriana Palma Calabokis,* ***Yamid E. Nuñez de la Rosa****, Jomar José Knaip Ribeiro e Paulo César Borges*
DOI: doi://10.26678/ABCM.COBEF2019.COF2019-0548

Congresso: **COBEF 2019**
Comportamento tribológico do aço inoxidável duplex UNS S32205 submetido a nitretação a plasma em baixas temperaturas
*Oriana Palma Calabokis,* ***Yamid E. Nuñez de la Rosa****, Jomar José Knaip Ribeiro e Paulo César Borges*
DOI: doi://10.26678/ABCM.COBEF2019.COF2019-0548

## Capítulo em livro

Estudo da evolução da rugosidade de dentes de engrenagens durante ensaios de desgaste tipo FZG" soluções em engenharia mecânica edição 2021

ISBN: 978-655-8902-55-3

## Participação em congresso

Congresso Brasileiro de Engenharia e Ciência dos Materiais – CBECiMat 2022

## Outras atividades no doutorado

**Estágio de doutorado**

Bolsa de doutorado sanduiche (PDSE: 88881.624474/2021-01) Estágio de doutorado na Universidade de Vigo - Espanha (6 meses).